Magnetic Properties of Frustrated

Pyrochlore Antiferromagnets

By

Jan Naess Reimers, B.Sc.

A Thesis

Submitted to the School of Graduate Studies

in Partial Fulfillment of the Requirements

for the Degree

Doctor of Philosophy

McMaster University

December 1990

FRUSTRATED PYROCHLORE ANTIFERROMAGNETS

Doctor of Philosophy (1990) McMaster University

(Chemistry) Hamilton Ontario

Title: *Magnetic Properties of Frustrated Pyrochlore Antiferromagnets*

Author: Jan Naess Reimers, B.Sc. (McMaster University)

Supervisor: Professor J. E. Greedan

Number of Pages: 155

Abstract

The magnetic properties of polycrystalline samples of pyrochlore antiferromagnets were investigated. The metal atoms in pyrochlores form a 3 dimensional network of corner sharing tetrahedra. Antiferromagnetic ordering is frustrated on such a lattice in the sense that all nearest neighbor microscopic interactions cannot be simultaneously satisfied. A number of experimental (Neutron diffraction, magnetic susceptibility and heat capacity) and theoretical techniques (mean field theory and Monte Carlo simulations) have been used to investigate the magnetic properties of this interesting lattice.

Considerable experimental evidence was consistent with spin glass behavior which is unusual for chemically ordered materials. All of the compounds investigated showed dramatic irreversibilities in the magnetic susceptibility data. A few of the materials (FeF_3, $Nd_2Mo_2O_7$ and $Mn_2Sb_2O_7$) were seen to exhibit long range order, which was complex in nature. $Tb_2Mo_2O_7$ and $Y_2Mn_2O_7$ showed no signs of magnetic ordering down to 7K but neutron scattering data indicated that strong short range correlations were present over a wide temperature range. Inelastic scattering for $Tb_2Mo_2O_7$ was consistent with some degree of spin freezing at 25K.

Mean field theory calculations predicted that no long range order would exist in pyrochlore antiferromagnets with only nearest neighbor interactions. Further neighbor interactions would in most cases stabilize complex long range magnetic order. Monte Carlo simulations showed that thermal fluctuations were insufficient to stabilize long range order in the absence of further neighbor interactions. Extensive simulations for a model with further neighbor interactions and long range order gave strong evidence for the existence of a new universality class in pyrochlore antiferromagnets. This result was supported by neutron scattering results for FeF_3.

Acknowledgments

Foremost I would to sincerely thank my supervisor, Dr. J. E. Greedan, for his guidance, patience, sense of humor and sharing his scientific skills and insights with me. I would also like to thank the many other faculty members for their guidance. In particular discussions with Dr. M. F. Collins on the subjects of neutron scattering and critical phenomena were indispensable. Dr A. J. Berlinsky was instrumental in initiating and supervising most of the theoretical work in this thesis. Useful discussions about neutron scattering with Dr. B. D. Gaulin who carried out the inelastic measurements on $Tb_2Mo_2O_7$ were also very much appreciated. Dr. C. V. Stager was always helpful in planning and interpreting the many magnetic susceptibility measurements carried out over the years. Dr. C. Kallin was also very kind in providing access to her computing facilities.

Assistance from and discussions with many postdoctoral fellows, Drs. A.-C. Shi, A. M. Brass, M. Bjorgvinnson, R. E. Kremer and M. F. Eitel were also indispensable. A very special thanks is due to the technical staff: G. Hewitson, J. Avelar, J. Cooper, J. Garret(thanks for welding my glasses back together) and M. Crowe, who can all make the most stubborn equipment work.

I must acknowledge my student friends: C. Trendall, A Dawson, J. Abudayy, Abdalla^2 and P. Williams, for all of the heated arguments over the years about everything from SU(3) gauge theory to the thermodynamics of frogs. One of the best ways to learn science is to have an argument.

Finally I wish to thank my Father (Mr. J. H. Reimers B. Eng.), my Brother (Mr R. G. Reimers B. A.) and Dr. Isaac Asimov for stimulating my interests in science when I was much younger.

Table of Contents

List of Figures

List of Tables

Chapter 1.

Introduction

1.1 Magnetism

1.1.1 Atomic Moments

For this work I will be concerned primarily with magnetism originating from localized atomic moments in 3d, 4d and 5f series elements. Both orbital and spin angular momentum contribute to the total magnetic moment in such a way that

$$\vec{\mu} = -\mu_B(\vec{L} + g_S\vec{S}) = -g_J\mu_B\vec{J} \qquad (1.1)$$

where $\vec{\mu}$ is the magnetic moment

$\mu_B = \frac{e\hbar}{2mc}$ is the Bohr magneton

$\vec{L}$ and $\vec{S}$ are respectively orbital and spin angular momentum

$g_S = 2$ (neglecting radiative corrections)

$g_J = \frac{3}{2} + \frac{S(S+1) - L(L+1)}{2J(J+1)}$ is the Landé g factor

and $\vec{J}$ is the total angular momentum .

This proportionality between angular momentum and magnetic moment is only valid when the mixing of the lowest lying zero field excited states is negligible. From now on g_J will simply be written as g.

Most often these atomic moments are loosely referred to as spins, even though the moment may have a considerable orbital contribution. There are other sources of magnetism in atoms such as nuclear moments and diamagnetism (which results from

field induced charge density currents). Both of these are 2 or 3 orders of magnitude weaker than the angular momentum moments.

1.1.2 Exchange:

In general the local moments in a crystal will interact with nearby neighbors and any external field that is present. The interaction with neighbors is by an exchange mechanism similar to that responsible for the well known singlet-triplet splitting in the hydrogen molecule. More relevant to pyrochlore oxides is the propagation of the exchange forces through one or more intermediate diamagnetic (no angular momentum) atoms, referred to as "super-exchange"[Kr34]. I will consider the following magnetic Hamiltonian

$$\mathscr{H} = -\frac{1}{2}\sum_{ij} \vec{S}_i \overleftrightarrow{J}_{ij} \vec{S}_j - \sum_i \vec{H}\cdot\vec{S}_i \tag{1.2}$$

where $\vec{S}_i$ is a spin vector (in units of $g\mu_B$, thus $\vec{S}_i\cdot\vec{S}_i = g^2\mu_B{}^2 S(S+1)$ where S is the spin quantum number) at lattice i, $\vec{H}$ is an external magnetic field, and $\overleftrightarrow{J}_{ij}$ is a second rank tensor describing the spin-spin interaction between sites i and j,

$$\overleftrightarrow{J}_{ij} = \begin{bmatrix} J_{ij}^{xx} & J_{ij}^{xy} & J_{ij}^{xz} \\ J_{ij}^{yx} & J_{ij}^{yy} & J_{ij}^{yz} \\ J_{ij}^{zx} & J_{ij}^{zy} & J_{ij}^{zz} \end{bmatrix}. \tag{1.3}$$

The connection between $\overleftrightarrow{J}_{ij}$ and crystal field theory is a very complicated subject, however a good deal of progress can be made using symmetry considerations. For example two atomic systems that are particularly relevant to this work are Mn^{2+} and

Fe^{3+}, which are isoelectronic. Both are d^5 ions with totally symmetric ^6A ground states and in pyrochlores they have an almost octahedral environment. Due to the spherical symmetry of the ions one might expect that $J^{xx} = J^{yy} = J^{zz}$ and all off diagonal elements are also equivalent to each other. Neglecting off diagonal elements one can construct the three most commonly treated models in magnetism: 1) the Ising model ($J^{xx} = J^{yy} = 0$), 2) the XY model ($J^{xx} = J^{yy}$, $J^{zz} = 0$), 3) the Heisenberg model ($J^{xx} = J^{yy} = J^{zz}$). Thus Fe^{3+} and Mn^{2+} are to a good approximation, Heisenberg systems.

When the $J_{ij} > 0$ the energy of (1.2) is minimized when all spins are parallel, *i.e.* a ferromagnetic ground state. If the nearest neighbor $J_{ij} < 0$ the system will be antiferromagnetic. When there is a mixture of positive and negative J's much more complicated situations can arise such as non-collinear (canted) order, incommensurate or helical order (where the repeat length of the magnetic structure is not an integral multiple of the chemical unit cell), or spin glass order which will be described below.

1.1.3 Thermodynamics:

The stability a magnetic system is governed by the free energy which can be thought of as a generating function of the thermodynamic functions.

$$\begin{aligned} F(\beta,\vec{H}) &= -T\ln[\mathcal{Z}] \\ &= -\frac{1}{\beta}\ln\left[Tr\{e^{-\beta\mathcal{H}}\}\right], \end{aligned} \tag{1.4}$$

where $\mathcal{Z}$ is the partition function and *Tr* indicates a summation over all spin states of the system, $\beta = \frac{1}{T}$ (I prefer units in which k_B=1). Differentiating $F(\beta,\vec{H})$ once with respect to $\vec{H}$ generates thermal expectation values for the corresponding conjugate field which is the magnetization,

$$\frac{\partial F}{\partial \vec{H}} = \frac{1}{\beta}\ln\left[Tr\{ \beta\sum_i \vec{S}_i e^{-\beta\mathcal{H}} \} \right]$$
$$= \vec{M}(\beta,\vec{H}) . \qquad (1.5)$$

Differentiating again gives the susceptibility tensor

$$\chi^{\alpha\gamma}(\beta,\vec{H}) = \frac{\partial^2 F}{\partial H^\alpha \partial H^\gamma} = \beta\left\langle (M^\alpha - \langle M^\alpha \rangle)(M^\gamma - \langle M^\gamma \rangle) \right\rangle \qquad (1.6)$$

where α,γ = x,y,z and $\langle\rangle$ denotes thermal expectation value. The susceptibility can be thought of as the system's response to an external field or alternatively, or as the amplitude of the thermal fluctuations in the magnetization. Again neglecting the off diagonal elements one can define an isotropic susceptibility in a straightforward manner

$$\chi^{iso} = \frac{1}{3}(\chi^{xx} + \chi^{yy} + \chi^{zz}) \qquad (1.7)$$

which is the quantity measured for powder samples.

1.1.4 Mean field theory:

Because of the exchange term in (1.2) that couples each spin with it's neighbors, the evaluation of the free energy (1.4) or any other thermodynamic functions will necessarily be a hopelessly complicated many body problem. The simplest and therefore most widely used approximation scheme is the mean field or Hartree approximation, in which one assumes that each spin is independent and only sees the average exchange field generated by all the other spins in the system. Since the spins are independent the exchange term in (1.2) decouples and one has N, one body

problems to solve. If one defines the so-called molecular field $\vec{H}_{mol}$ then the Hamilton is greatly simplified

$$\vec{H}_{mol} = \vec{M}\sum_i J_{0i} + \vec{H}$$
$$= \vec{M} J_o + \vec{H} \tag{1.8}$$

$$\mathcal{H} = -N\vec{S}\cdot\vec{H}_{mol} \tag{1.9}$$

$$F(\beta,\vec{H}) = -\frac{N}{\beta}\ln\left[Tr_{\vec{S}}\{ e^{\beta\vec{S}\cdot\vec{H}_{mol}} \} \right] \tag{1.10}$$

The trace over spin states is a geometric series which can be summed for general S with the z axis along the molecular field,

$$F = -\frac{N}{\beta}\ln\left[\frac{\sinh[(S+\frac{1}{2})\beta H_{mol}]}{\sinh[\frac{1}{2}\beta H_{mol}]}\right]. \tag{1.11}$$

Since H_{mol} depends on the magnetization one must solve the non-linear mean field equation

$$M = \frac{\partial F}{\partial H} \tag{1.12}$$

self-consistently. At high temperature one can expand (1.11) in a Taylor series

$$F = -N\left[\ln(2S+1) + \frac{1}{6}g^2\mu_B^2 S(S+1)\beta H_{mol}^2 - \frac{1}{360}g^4\mu_B^4 S(S+1)(2S^2+2S+1)\beta^3 H_{mol}^4 + \ldots\right]. \tag{1.13}$$

The magnetization to first order in β is

$$M = \frac{\partial F}{\partial H} = \frac{1}{3} g^2 \mu_B{}^2 S(S+1) \beta (MJ_o + H) . \tag{1.14}$$

Solving for M and differentiating with respect to H gives the Curie Weiss law for the magnetic susceptibility

$$\chi = \frac{C}{T-\theta} \tag{1.15a}$$

where

$$C = \frac{1}{3} g^2 \mu_B{}^2 S(S+1) \tag{1.15b}$$

$$\theta = C \sum_i J_{0i} . \tag{1.15c}$$

Thus a measurement of the high temperature susceptibility should give information on the net moment of the magnetic species and an estimate of the sum of all exchange constants in the system. Caution is advised in the interpretation of θ since crystal field effects that split the ground state term or nearby exited terms, can also contribute to θ. When $T < \theta$ and $H = 0$ then one finds that self a consistent solution of (1.14) only exists for non-zero M. Thus one may associate θ with the mean field critical temperature T_c below which spontaneous magnetization occurs. Both the magnetization and the susceptibility follow a power law behavior near T_c,

$$M = M_o(T_c-T)^{1/2} \tag{1.16}$$

$$\chi = C (T-T_c)^{-1} . \tag{1.17}$$

1.1.5 Frustration

Frustration is the inability of a system to simultaneously minimize all microscopic interactions in the Hamiltonian. The term frustration is mostly used in connection with magnetism but this concept is of course important in almost all branches of science. An obvious example would be the kinetic and potential energy terms in the electronic Hamiltonian of an atomic or molecular system. The potential energy is minimized when all electrons crash into the nucleus, however the uncertainty principle tells us that localizing the electron at the nucleus necessarily increases the kinetic energy without bound. The system must find a happy medium with completely different (and more interesting) physics than that predicted by each Hamiltonian term separately. Classic examples of frustrated magnets are the triangular lattice antiferromagnet, the face centered cubic (FCC) lattice antiferromagnet and any antiferromagnet and an external field. Ferromagnets on any lattice are not frustrated. Fig. 1.1 shows schematic diagrams of finite plaquettes taken from the square, triangular and FCC lattice.

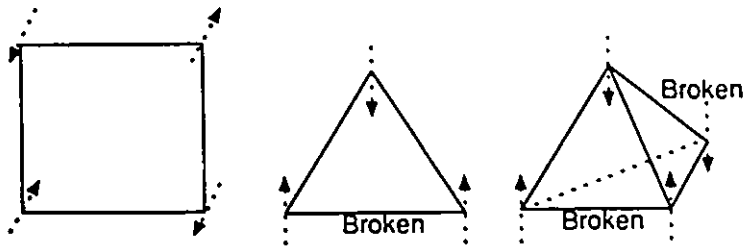

Fig. 1.1 Square, triangular, and tetrahedral spin clusters

The square lattice is un-frustrated. Antiferromagnetic interactions prefer neighboring spins to be aligned anti-parallel (180°) and it is a simple matter to decorate the lattice with up and down spins satisfying this requirement. For the triangle things become non-trivial. Any attempt at decorating the triangle with up and down spins results in

one broken antiferromagnetic bond. For the tetrahedron the situation is even worse with two bonds always broken. The grounds states of these systems are seen to be highly degenerate which is a general feature of frustrated magnets. A lower energy state than the one shown in Fig. 1.2 for the triangle might be one in which the spins are mutually oriented at 120°, thus non-collinear.

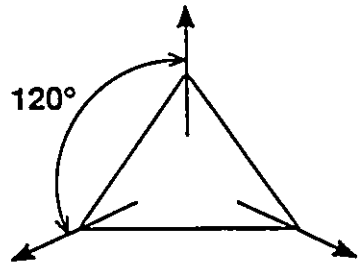

Fig. 1.2 The 120° spin arrangement found in some triangular lattice systems.

Something resembling a 120° arrangement is only possible if the spin quantum number, S, is large. One can ask at this point whether there is a criterion for determining which system (the triangle or the tetrahedron) is more frustrated than the other. Before one trys to answer this question one must first consider the ground states of the clusters in Fig. 1.1.

For a cluster with $p \geq 2$ spins all interconnected with interaction $J < 0$ the reduced energy per spin is

$$\frac{E}{p|J|} = e = \frac{1}{p}\sum_{ij}^{p} \vec{S}_i \cdot \vec{S}_j$$

$$= \frac{1}{p}\left[\sum_{i=1}^{p} \vec{S}_i\right]^2 - \frac{1}{p}\sum_{i=1}^{p} S_i^2$$

$$= \frac{1}{p}\left[\sum_{i=1}^{p} \vec{S}_i\right]^2 - S(S+1) \qquad (1.18)$$

where the sums are unrestricted. The ground state of this system has reduced energy

of $e_o = -S(S+1)$ and is determined by the condition

$$\sum_{i=1}^{p} \hat{S}_i = 0 . \tag{1.19}$$

Lacorre has proposed a method of gauging frustration by calculating the so called "constraint function"[La87]. He defines the basis energy of the system as the sum of all pair interaction energies as if they were not frustrated:

$$E_b = \sum_{ij}^{p} |J_{ij}| \, |\hat{S}_i| \, |\hat{S}_j| \tag{1.20}$$

$$= |J| \; S(S+1) \; p(p-1) \tag{1.21}$$

thus

$$\frac{E_b}{p|J|} = e_b = S(S+1)\,(p-1), \; p \geq 2 . \tag{1.22}$$

The constraint function is now defined as the ratio of the system energy per unit cell, to its basis energy

$$F_c = \frac{E}{E_b} = \frac{e}{e_b} = \frac{-1}{p-1}, \; p \geq 2 . \tag{1.20}$$

In general F_c ranges from -1 (non-frustrated) to +1 (fully frustrated). For the model of p antiferromagnetically coupled clusters, the degree of frustration increases with p. According to this definition the tetrahedron ($p = 4$, $F_c = -\frac{1}{3}$) is more frustrated than the triangle ($p = 3$, $F_c = -\frac{1}{2}$). The constraint function has been discussed in more general terms by Lacorre[La87]

1.1.6 Spin Glasses

Spin glasses are magnetic systems in which frustration arises from some sort of frozen-in structural disorder. A simple example would be a square lattice with randomly distributed positive and negative exchange interactions. Square plaquettes with an odd number of antiferromagnetic interactions will be frustrated.

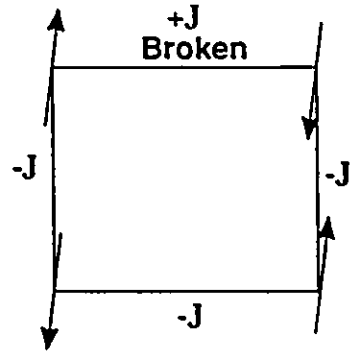

Fig. 1.3 A frustrated square plaquette.

Frustration and randomness are considered necessary but not sufficient conditions for spin glass behavior. No conventional long range order can be established in these systems. However below a certain temperature, T_f, the spins will freeze into some state where they are aligned in random directions. As with periodic frustrated systems (no structural disorder) the ground state is highly degenerate.

Spin glasses have a number of experimental signatures[Bi86]:

1) A sharp cusp in the frequency dependent susceptibility at T_f
2) Frequency dependence of T_f
3) A remnant magnetization in field cooled samples.
4) Onset of short range spin-spin correlations below T_f
5) A broad peak in the magnetic heat capacity, C_m, above T_f
6) Linear behavior of C_m below T_f (in some instances $C_m \propto T^{1.5}$).

There are a number of unresolved questions regarding spin glasses

1) What is the nature of the frozen state?
2) Is the spin freezing transition a new type of phase transition?
3) Is the lack of long range order simply due to a failure to reach equilibrium with in the observation time? In other words are spin glasses non-ergodic?

Below the freezing temperature the free energy of a spin glass develops a large number of degenerate local minima in phase space with essentially the same macroscopic properties. These minima are separated by large barriers which prevent the system from fluctuating between the minima.

The study of spin-glasses has had a strong impact on other diverse areas in science such as neural networks[Li74,Ho82], models of evolution[An83], and optimization problems[Ki83].

1.1.7 Critical Phenomena

Phase transitions come in a number of varieties, from common liquid-vapor and liquid-solid transitions to more exotic effects like the onset of superconductivity and the condensation of the Quark-Gluon plasma into hadronic matter. So called first-order

phase transitions involve the discontinuous change of some thermodynamic properties (first derivatives of the free energy) at the critical point. In particular there is a discontinuity in the enthalpy as a function of temperature and thus a latent heat for the transition. A classic example is the melting of ice at 1 atm pressure. Many phase transitions in magnetic systems are continuous and known as critical phase transitions, where the thermodynamic properties are continuous but non-analytic at T_c.

Mean field theory is successful in predicting spontaneous magnetic long range order at some critical temperature T_c, and near T_c the magnetization and susceptibility obey power law behavior in the reduced temperature $t = (T-T_c)/T_c$

$$M \alpha (-t)^{\beta}$$
$$\chi \alpha (t)^{-\gamma}$$

with $\beta = \frac{1}{2}$ and $\gamma = 1$. Further analysis of the mean field approach shows that the heat capacity will have a jump discontinuity at T_c. Also the mean field results are fairly insensitive to the dimensionality of the lattice *d*. There are a number of characteristics of phase transitions where mean field theory is at odds with experiment.

1) In general $\beta \neq \frac{1}{2}$, $\gamma \neq 1$.

2) Heat capacity shows a so called lambda anomaly at T_c with exponent α, $C \sim |t|^{\alpha}$.

3) All one dimensional and many two dimensional systems do not spontaneously order at finite temperature, *i.e.* $T_c = 0$.

The mean field approach completely neglects any local deviations of the magnetization from its mean value. These deviations are generally referred to as fluctuations. Near the critical temperature of a ferromagnet the free energy of the

ordered phase and the paramagnetic phase are not very different, thus one may expect small regions of the unstable phase to coexist with the stable phase. For example just above T_c the paramagnetic phase is most stable, however small ferromagnetic domains will exist for limited time scales. The closer one gets to T_c the larger the domains become. If one imagines looking at the magnet with a microscope equipped with a magnification adjustment, then changes in reduced temperature t will be indistinguishable from changes in magnification, since both alterations have the effect of changing the domain sizes. This remarkable fact was first pointed out by Kadanoff[Ka66]. If one defines the correlation length ξ as the average domain size, then

$$\xi = t^{-\nu}$$

and mean field theory predicts that $\nu = 1/2$. At $T = T_c$, $\xi = \infty$ and the system is scale invariant. For first order transitions the phase change occurs abruptly and ξ never reaches ∞. So far I have defined four critical exponents α, β, γ, and ν, which have been determined, through many years of effort, for a number of different magnetic systems, from both experimental measurements and careful calculations. Approximate values of these exponents are listed in table 1.1.

Table 1.1

Critical exponents for some models[Co89]

Models	d^a	n^b	α	β	γ	ν
Mean field[c]	all	all	—	$\frac{1}{2}$	1	$\frac{1}{2}$
2d-Ising[c]	2	1	0	$\frac{1}{8}$	$\frac{7}{4}$	1
3d-Ising	3	1	0.106	0.326	1.2378	0.6312
3d-XY	3	2	-0.01	0.345	1.316	0.669
3d-Heisenberg	3	3	-0.121	0.367	1.388	0.707

[a] Lattice dimensionality, a number of 3-d lattices are effectively 2-d magnets because exchange coupling along the third direction is cancelled by symmetry.

[b] Effective spin-space dimensionality. Strong anisotropy can make fluctuations along certain directions in spin-space negligible.

[c] These exponents are exact. The 2-d Ising model was solved exactly by Onsager[On44,Ya52].

A number of comments are in order. 1) 2-d XY and Heisenberg systems are not included because long range order is not stable in these systems as proved by Mermin and Wagner[Me66]. 2) The exponents have a weak dependence on the dimensionality of spin-space, *n*. 3) The exponents are independent of lattice geometry (*i.e.* cubic, hexagonal or face centered), exchange constants and quantum effects. 4) These exponents are valid for ferromagnets and non-frustrated or collinear antiferromagnets.

The independence of the exponents mentioned in (3) has led to the now famous universality hypothesis which goes roughly as follows[Co89].

For a continuous phase transition the static critical exponents depend on the following three properties and nothing else.

1) The dimensionality of the system, *d*.
2) The symmetry of the order parameter.
3) Whether the forces are of short or long range.

Conditions 1 and 3 are fairly straight forward and it is worth pointing out that systems with long range forces (magnetic exchange is usually short range) will have mean field behavior. Identifying the order parameter and its symmetry for ferromagnets is rather simple. The order parameter is the magnetization vector, and its symmetry depends on the dimensionality of spin-space *n*. For n=1 the magnetization is a scalar, and the free energy is invariant under a change in sign which corresponds to reversing all the spins in the system. For XY and Heisenberg systems the free energy is invariant under order parameter rotations in 2 and 3 dimensional space respectively. The symmetry of the order parameter for frustrated non-collinear systems, such as the triangular lattice antiferromagnet with the 120° ordered phase, is non-trivial.. Therefore one might expect that frustrated systems will have different critical exponents than those listed in table 1.1. Whether or not universality holds up in these non-trivial frustrated systems is not yet established.

1.2 Pyrochlores

1.2.1 Crystal Chemistry

Pyrochlores are isostructural to the mineral $(NaCa)(NbTa)O_6F/OH$ and have the general formula $A_2B_2O_6O'$ where A and B are metals. The space group for the ideal pyrochlore structure is $Fd\bar{3}m$ with eight formula units per unit cell and unit cell edges

in the neighborhood of 10Å. The atom positions and site symmetries are shown in table 1.2.

Table 1.2

The Pyrochlore Structure

Space group: $Fd\bar{3}m$ $A_2B_2O_6O'$ $Z = 8$

Atom	Pos.	Site Symmetry	Frac. Coord.
A	16d	$\bar{3}m$ (D_{3d})	$(\frac{1}{2},\frac{1}{2},\frac{1}{2})$ $(0,\frac{1}{2},\frac{1}{2})$ $(\frac{1}{2},0,\frac{1}{2})$ $(\frac{1}{2},\frac{1}{2},0)$ + FC[a]
B	16c	$\bar{3}m$ (D_{3d})	$(0,0,0)$ $(0,\frac{1}{2},\frac{1}{2})$ $(\frac{1}{2},0,\frac{1}{2})$ $(\frac{1}{2},\frac{1}{2},0)$ + FC
O	48f	mm (C_{2v})	$(x,\frac{1}{8},\frac{1}{8})$ $(\bar{x},\frac{7}{8},\frac{7}{8})$ $(\frac{1}{4}-x,\frac{1}{8},\frac{1}{8})$ $(\frac{3}{4}+x,\frac{7}{8},\frac{7}{8})$ + FC $(\frac{1}{8},x,\frac{1}{8})$ $(\frac{7}{8},\bar{x},\frac{7}{8})$ $(\frac{1}{8},\frac{1}{4}-x,\frac{1}{8})$ $(\frac{7}{8},\frac{3}{4}+x,\frac{7}{8})$ + FC $(\frac{1}{8},\frac{1}{8},x)$ $(\frac{7}{8},\frac{7}{8},\bar{x})$ $(\frac{1}{8},\frac{1}{8},\frac{1}{4}-x)$ $(\frac{7}{8},\frac{7}{8},\frac{3}{4}+x)$ + FC
O′	8b	$\bar{4}3m$ (T_d)	$(\frac{3}{8},\frac{3}{8},\frac{3}{8})$ $(\frac{5}{8},\frac{5}{8},\frac{5}{8})$ + FC

[a] FC stands for the face centering operation $(0,0,0)$ $(0,\frac{1}{2},\frac{1}{2})$ $(\frac{1}{2},0,\frac{1}{2})$ and $(\frac{1}{2},\frac{1}{2},0)$.

The A and B atoms are respectively 8 and 6 fold coordinated. The oxygen at the 48f site has one adjustable parameter, when $x = \frac{1}{8}$ the coordination shell of the A atoms forms a regular cube and when $x = \frac{5}{16}$ the B atom coordination is a regular octahedron. Of primary interest for this work are the metal atom sublattices, each of which forms an infinite network of corner-sharing tetrahedra shown in Fig. 1.4. A more complete discussion of pyrochlore oxides can be found in a review article by Subramanian[Su83].

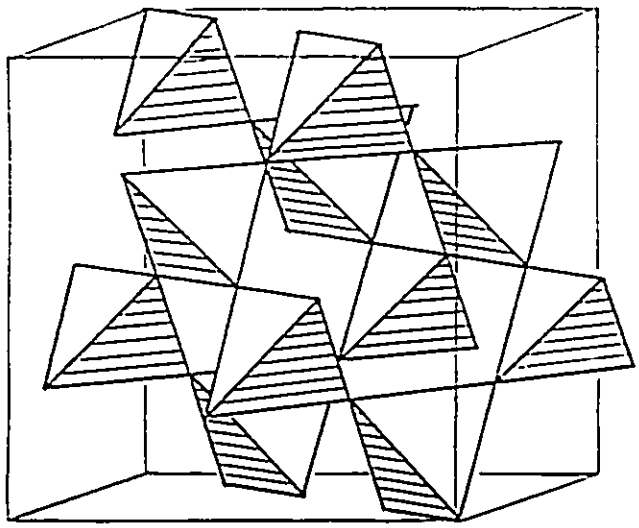

Fig. 1.4 Three dimensional network of corner-sharing tetrahedra formed by one of the metal sublattices in pyrochlores.

1.2.2 Magnetic Properties

Most of what is known about the magnetic properties of pyrochlore oxides comes from magnetic susceptibility and heat capacity data. Very little is known about magnetic long range order, particularly for antiferromagnets. From Sec. 1.4 one knows that the tetrahedron with antiferromagnetic interactions is highly frustrated. Thus one might expect that a lattice of corner-sharing tetrahedral will also be very frustrated and therefore interesting.

The problem of antiferromagnetic ordering on this lattice was first considered by P. W. Anderson[An56], who predicted on qualitative grounds a very high ground state degeneracy and that no long range order would exist at any temperature for Ising spins. Villain reached basically the same conclusion for Heisenberg spins[Vi78], calling the system a "Cooperative Paramagnet" . Liebmann has performed computer simulations of an Ising pyrochlore antiferromagnet and found no evidence for long

range order[Li86].

Heat capacity measurements[Bl 68] for the series of compounds $R_2M_2O_7$ (R = rare earth, M = Ti, Sn, Zr, $\frac{1}{2}\{Ga^{3+}Sb^{5+}\}$) show transitions to long range order in only a few cases, and then only at temperatures below 2K. The remaining systems show broad features in the heat capacity which may be due to the onset of short range order over a wide temperature range.

A large amount of work has also been done on the related series of compounds $R_2M_2O_7$ (R = rare earth, M = Mo[Sa 86], Mn[Sub 88]). Magnetic measurements for the Mo series show a wide range of magnetic behavior, in particular $Nd_2Mo_2O_7$ and $Sm_2Mo_2O_7$ have complex magnetization curves with two apparent critical temperatures. For R = Tb, Dy, Ho, Er, Tm, Yb and Y the susceptibility data indicate strong deviations from Curie-Weiss behavior and no evidence for long range order down to 4K.

All of the $R_2Mn_2O_7$ compounds appear to be ferromagnetic from high field susceptibility data[Sub88], however it is still of interest to discuss the possibility of antiferromagnetic nearest neighbor interactions for the Mn sublattice.

A more complete discussion of the magnetic properties of oxide pyrochlores will be found in a recent review article by Greedan[Gr90].

This interesting lattice is also realized in spinel compounds, AB_2O_4 at the B site, and in the cubic Laves phase RMn_2 where the Mn atoms lie on the 16d site. Many of these systems undergo lattice distortions at the magnetic phase transition which will lift the degeneracy of the magnetic ground state. Neutron diffraction experiments on a large number of the spinel compounds[Ha56,Lo71,Pl75,Ak77,Po82,Vo87] and YMn_2[Ba87,Ba88] have shown significant diffuse scattering over a wide temperature range above T_c and complex magnetic order below T_c, which are both indications of magnetic frustration.

Chapter 2

Long Range Order

2.1 Neutron Scattering:

2.1.1 Introduction:

Although the neutron is a neutral particle it has a magnetic moment of $1.9132\mu_N$, where μ_N is the nuclear magneton. Neutrons will interact with matter via a strong force interaction with the nuclei as well as a magnetic dipole interaction with the electron spin density. Fission reactions in nuclear reactors generate large quantities of neutrons, which will come to thermal equilibrium with the reactor moderator. Thermal neutron velocities will have a Maxwellian distribution peaked at a wave length of about 1.4Å for a moderator temperature of 300K.

In a typical experiment neutrons from the reactor core are scattered from a monochromator crystal which acts like a prism, thus generating neutrons sharply peaked at a single wavelength. The sample is imersed in a beam of monochromated neutrons which are then scattered with a probability, σ_s, called the scattering cross section. Scattered neutrons are detected over some small region of solid angle $d\Omega$. The whole process is shown schematically in Fig. 2.1.

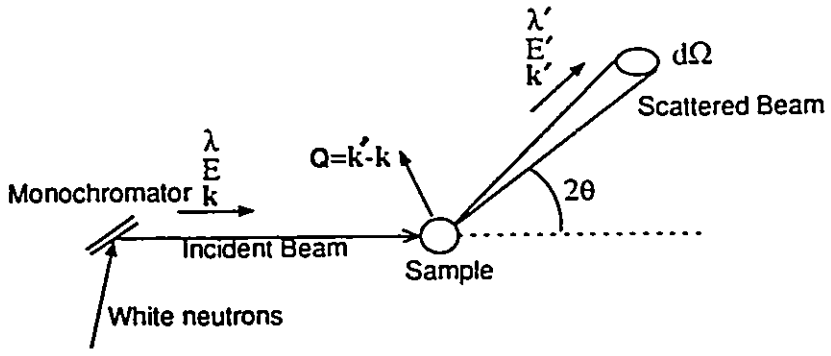

Fig. 2.1. Schematic view of a 2-axis neutron scattering experiment.

The incident and scattered neutrons are characterized by wave vectors $\vec{k}$ and $\vec{k}'$ respectively. A neutron with wavevector $\vec{k}$ travels in the direction of $\vec{k}$ with wave length $\lambda = \frac{2\pi}{k}$, momentum $\hbar\vec{k}$, and energy $\frac{\hbar^2 k^2}{2m}$. A scattering event can be characterized by a scattering vector $\vec{Q} = \vec{k}' - \vec{k}$ which is proportional to the momentum transfer of the neutron. By measuring the intensity of the scattered beam as a function of scattering angle or equivalently as a function of $\vec{Q}$, one can obtain information about the microscopic details of the sample on length scales of the order λ. At this point I will not consider the distinction of inelastic processes for which $E \neq E'$. Such experiments would involve an analyzer crystal, like the monochromator in function, placed between the sample and detector. These are called triple-axis experiments. Of central interest is the differential scattering cross section which is the probability of scattering a neutron into a small region of solid angle $d\Omega$,

$$\frac{d\sigma}{d\Omega} d\Omega \,. \qquad (2.1)$$

2.1.2 Differential Cross section:

Derivation of the differential cross section for magnetic scattering of neutrons is rather involved due to the complicated nature if the interaction potential between the neutron and atomic magnetic moments. The details are sketched out in any good book on neutron diffraction[Ba75,Sq78,Lo84,Co89]. For elastic scattering the final result for a non-Bravais lattice is

$$\frac{d\sigma}{d\Omega} = (\tfrac{1}{2}\gamma r_o)^2 \sum_{ij} e^{i\vec{Q}\cdot(\vec{R}_i-\vec{R}_j)} \times \sum_{ab} f_a(\vec{Q})\, f_b(\vec{Q})\, e^{i\vec{Q}\cdot(\vec{r}_a-\vec{r}_b)} \langle \vec{S}^{\perp}_{ia}\cdot\vec{S}^{\perp}_{jb}\rangle \qquad (2.2)$$

where

$\frac{1}{2}\gamma r_o = .27\times10^{-12}$ cm, is the neutron scattering length per Bohr magneton

$\gamma = 1.9132$ is the neutron magnetic moment in nuclear magnetons

$r_o = e^2/mc^2$ is the classical radius of the electron

i and *j* label unit cells

a and *b* label atoms within a unit cell

$\vec{Q}$ is the neutron scattering vector

$f_a(\vec{Q})$ is the magnetic form factor for atom *a*

$\vec{S}_{ia}$ is an atomic spin vector (in units of μ_B) at position $\vec{R}_i + \vec{r}_a$

$\vec{S}^{\perp} = \vec{S} - \hat{Q}(\vec{S}\cdot\hat{Q})$ is the component of $\vec{S}$ perpendicular to the scattering vector.

<> indicates thermal expectation value

$\langle \vec{S}_{ia}\cdot\vec{S}_{jb}\rangle$ is the spin-spin correlation function.

The magnetic form factor is similar to the charge density form factor encountered in the analysis of X-ray scattering. Because the spin density of an atom

has a spatial extent that is comparable with neutron wavelength, interference effects between scattering from different parts of the atom will occur. The interference effects become stronger as the scattering angle increases. Formally $f_a(\vec{Q})$ is the normalized Fourier transform of the atomic magnetization density

$$f_a(\vec{Q}) = \frac{\int \vec{S}_a(\vec{r})\, e^{i\vec{Q}\cdot\vec{r}}\, d^3\vec{r}}{\int \vec{S}_a(\vec{r})\, d^3\vec{r}} \tag{2.3}$$

2.1.3 Bragg Scattering:

Below T_c where the system is long range ordered the spin-spin correlation function will be independent of i and j

$$\langle \vec{S}^{\perp}_{ia} \cdot \vec{S}^{\perp}_{jb} \rangle = \langle \vec{S}^{\perp}_{a} \rangle \cdot \langle \vec{S}^{\perp}_{b} \rangle . \tag{2.4}$$

The double summation over lattice sites in (2.2) can now be evaluated

$$\sum_{ij} e^{i\vec{Q}\cdot(\vec{R}_i - \vec{R}_j)} = N \sum_{i} e^{i\vec{Q}\cdot\vec{R}_i}$$
$$= N^2 \delta(\vec{K}-\vec{Q}) \tag{2.5}$$

where

$$e^{i\vec{K}\cdot\vec{R}_i} = 1 , \text{ all } i . \tag{2.6}$$

The relation (2.5) tells us that the cross section is sharply peaked near scattering vectors that satisfy (2.6). These special vectors are commonly known as reciprocal lattice

vectors, since all solutions of (2.6) form a lattice in momentum (reciprocal or Q) space. If $\vec{a}$, $\vec{b}$, and $\vec{c}$ are the lattice vectors that define the unit cell edges in the crystal, then one wishes to relate these basis vectors to the basis vectors ($\vec{a}^*$, $\vec{b}^*$, $\vec{c}^*$)that define the reciprocal space lattice. With the following definitions (2.6) is always satisfied

$$\vec{R} = n_1\vec{a} + n_2\vec{b} + n_2\vec{c}, \quad n_1,n_2,n_3 \text{ are integers} \tag{2.7}$$

$$\vec{K} = h\vec{a}^* + k\vec{b}^* + l\vec{c}^*, \quad h,k,l \text{ are integers} \tag{2.8}$$

$$\begin{aligned} \vec{a}^* &= \frac{2\pi}{V}\vec{b}\times\vec{c} \\ \vec{b}^* &= \frac{2\pi}{V}\vec{c}\times\vec{a} \\ \vec{c}^* &= \frac{2\pi}{V}\vec{a}\times\vec{b} \end{aligned} \tag{2.9}$$

$$V = \vec{a}\cdot(\vec{b}\times\vec{c}) \text{ is the unit cell volume.} \tag{2.10}$$

The hkl's that label the reciprocal lattice points can be interpreted as Miller indices labeling planes of atoms (or spins) in direct space. With these definitions the cross section becomes

$$\frac{d\sigma}{d\Omega}(hkl) = (\tfrac{1}{2}\gamma r_o N)^2 \, |\vec{F}_{hkl}|^2 . \tag{2.11}$$

$\vec{F}_{hkl}$ is the structure factor which takes into account interference effects between magnetic atoms in the unit cell.

$$\vec{F}_{hkl} = \sum_a e^{i\vec{K}\cdot\vec{r}_a} f_a(\vec{Q}) <\vec{S}^{\perp}_{ia}>$$
$$= \sum_a \exp\left[2\pi i[x_a h + y_a k + z_a l]\right] f_a(\vec{Q}) <\vec{S}^{\perp}_{ia}> \qquad (2.12)$$

where x_a, y_a and z_a are the fractional coordinates of atom a.

Of course there is no reason to expect the magnetic structure to have the same periodicity as the atomic structure, particularly in frustrated systems. A simple example would be an antiferromagnet on a cubic lattice which has a magnetic unit cell with lattice vectors $2\vec{a}$, $2\vec{b}$, $2\vec{c}$. One can still use the technology described above if one defines magnetic direct and reciprocal, lattice vectors such as

$$\vec{a}_m = 2\vec{a}, \quad \vec{b}_m = 2\vec{b}, \quad \vec{c}_m = 2\vec{c} \qquad (2.13a)$$

$$\vec{a}^*_m = \frac{1}{2}\vec{a}^*, \quad \vec{b}^*_m = \frac{1}{2}\vec{b}^*, \quad \vec{c}^*_m = \frac{1}{2}\vec{c}^*. \qquad (2.13b)$$

One can show that the condition for non-zero scattering (2.5) or $\vec{Q} = \vec{K}$, is equivalent to Braggs law. In particular for a cubic system where the expression for K^2 is rather simple

$$|\vec{Q}| = |\vec{k}'-\vec{k}| = |\vec{K}|$$
$$k^2+k'^2 - 2kk'\cos(2\theta) = K^2$$
$$(2\pi)^2\left[\frac{2}{\lambda^2} - \frac{2}{\lambda^2}\cos(2\theta)\right] = (2\pi)^2 a^{*2}(h^2+k^2+l^2)$$
$$4\sin^2\theta = \lambda^2\frac{(h^2+k^2+l^2)}{a^2}.$$

If one now replace $a^2/(h^2+k^2+l^2)$ with the square of the distance, d^2_{hkl}, between the

corresponding Miller planes one obtains the familiar form of Braggs law

$$\lambda = 2d_{hkl}\sin\theta . \tag{2.14}$$

2.1.4 Paramagnetic Scattering:

In the paramagnetic temperature range the spins are all completely uncorrelated thus

$$\begin{aligned} \langle \vec{S}^{\perp}_{ia} \cdot \vec{S}^{\perp}_{jb} \rangle &= \langle \vec{S}^{\perp 2}_{ia} \rangle \delta_{ij}\, \delta_{ab} \\ &= \tfrac{2}{3} g^2 \mu_B^2\, S(S+1)\, \delta_{ij}\, \delta_{ab} . \end{aligned} \tag{2.15}$$

All interference effects between atoms are no longer present and the cross section is rather simple

$$\frac{d\sigma}{d\Omega} = \tfrac{2}{3} N g^2 \mu_B^2\, S(S+1) \left[\tfrac{1}{2}\gamma r_o f(\vec{Q})\right]^2 \tag{2.16}$$

which is only weakly dependent on $\vec{Q}$ (or the scattering angle), through the magnetic form factor.

2.1.5 The Powder experiment:

All two-axis experiments were carried out at the McMaster Nuclear Reactor (MNR) using 1.3913 Å neutrons obtained from a copper monochromator [hkl]=[200]. The detector was a Position Sensitive Detector (PSD) which can collect data simultaneously over a one dimensional strip of solid angle. All samples were polycrystalline in which the individual grains were assumed to be randomly oriented.

Because of this the amount of information that can be obtained is considerably reduced. To be more specific the scattering cross section presented above must be averaged over all directions in momentum space, thus making $\frac{d\sigma}{d\Omega}$ a function of θ only. As θ increases the PSD covers a smaller and smaller fraction of solid angle which is compensated for in any intensity calculation by a factor of $1/\sin\theta$. Another factor of $1/\sin 2\theta$, called the Lorentz factor, arises from integrating $\frac{d\sigma}{d\Omega}$ over the solid angle near the reciprocal lattice point. Finally

$$\sigma(\vec{K}) = \sigma_{hkl} = (\tfrac{1}{2} r_o N)^2 \, |\vec{F}_{hkl}|^2 \, \frac{1}{\sin\theta \, \sin 2\theta} \tag{2.17}$$

and

$$\sigma(\theta) = \sum_{\vec{K}} \sigma(\vec{K}) \, \delta\Big[\, |K| - 4\pi \sin(\theta)/\lambda \, \Big] \tag{2.18}$$

where the angular average in momentum space is performed in (2.18). This last expression implies that the scattering intensity will have delta function peaks at Bragg angles defined in (2.14). The measured intensity is actually a convolution of (2.18) with the resolution function of the instrument which, to a very good approximation, is a Gaussian function of θ.

$$I(\theta) = \frac{1}{4\ln\sqrt{2} \, Hw} \int d\theta' \, \sigma(\theta') \exp\Big[-4\ln 2 \, \frac{(\theta' - \theta)^2}{Hw^2} \Big] \tag{2.19}$$

Hw is the full width at half maximum of a Bragg peak which is actually a slowly varying function of θ. For clarity a number of constant numerical factors in the cross section have been neglected, which would only be important in calculating the absolute intensity. For this work I am only interested in calculating the relative scattering intensities at different scattering angles.

In practice one proposes a structural model which will determine all peak positions and intensities. Using a computer the model is relaxed in such a way that the fit between calculated and observed scattering profiles (including background) is optimized. In the end one obtains a set of refined model parameters and their associated errors. This technique is commonly known as the Rietveld profile refinement method[Ri67,Ri69,Al82]. It is also possible to refine a model by comparing calculated peak intensities with integrated intensities from the data. However this method suffers when the Bragg peaks in the data set overlap with each other.

2.2 Experimental Results:

2.2.1 Results for $Nd_2Mo_2O_7$:

The sample was prepared by M. Sato[Sa86]. Previous work on $Nd_2Mo_2O_7$ [Sa86][Al89]shows metallic behavior and spontaneous net magnetization below ≡ 93K. A second transition is observed near 20K where the net magnetization vanishes. The compound also exhibits strong sample history dependence in the low field magnetization below 20K. Data sets at 150, 105, 53, 11K were collected.

Fig. 2.2 shows the low temperature data sets with the 150K data subtracted in order to remove nuclear Bragg scattering and paramagnetic scattering.

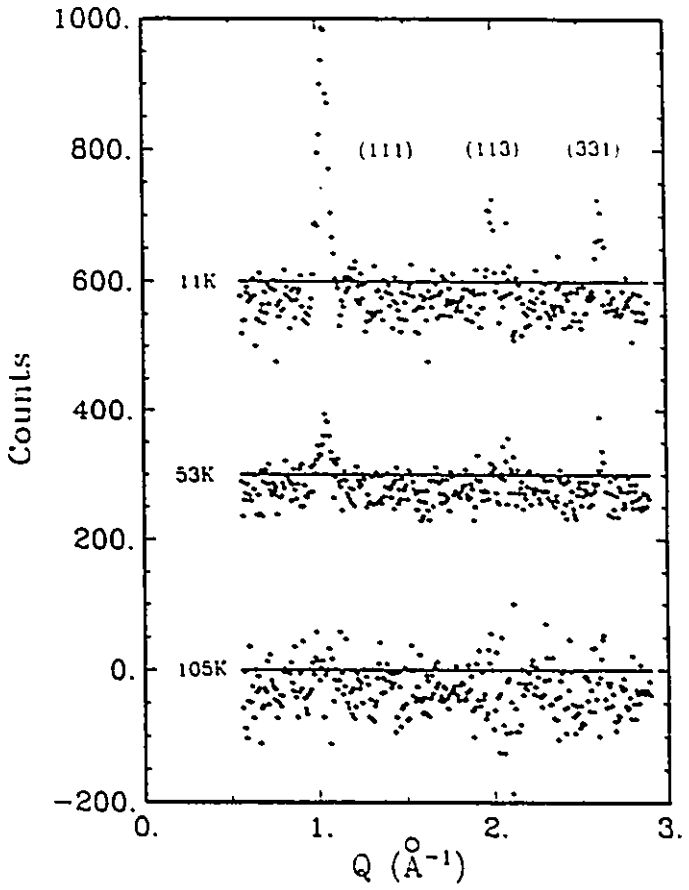

Fig. 2.2 Low temperature neutron data sets for $Nd_2Mo_2O_7$ after subtracting the 150K data. The 11 and 53K data are offset for clarity.

Small changes in the cell constants with temperature made it necessary to rescale Q-space for the 273K data set at each temperature in such a way that the nuclear reflections would superimpose. This procedure is of course only valid for cubic systems. The 53 and 11K data sets clearly show a Bragg peak near Q = 1 $\mathring{A}^{-1}$ which can be indexed as a (111) reflection. Weaker resolution limited scattering is also observed at the (113) and (331) Bragg angles. The absence of reflections with even (hkl) suggests a magnetic structure that is anti-body-centered. However this is only

possible if the Mo moments are exactly equal and opposite to the Nd moments, which would be accidental, thus the anti-body-centering is most likely only a pseudo-symmetry. A number of models consistent with the pseudo-symmetry are shown schematically in Fig. 2.3.

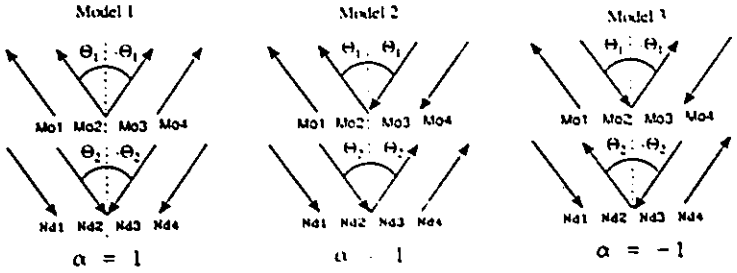

Fig. 2.3 Schematic representations of the three magnetic structural models tested for $Nd_2Mo_2O_7$. α is defined in Table 2.1.

Table 2.1

Metal atom positions and spin vectors in $Nd_2Mo_2O_7$

Spin #	Species	Fract. Coord.
$\hat{S}_1$	Mo	(0,0,0) + F.C.
$\hat{S}_2 = \alpha \hat{S}_1$	Mo	$(0,\frac{1}{4},\frac{1}{4})$ + F.C.
$\hat{S}_3$	Mo	$(\frac{1}{4},0,\frac{1}{4})$ + F.C.
$\hat{S}_4 = \alpha \hat{S}_3$	Mo	$(\frac{1}{4},\frac{1}{4},0)$ + F.C.
$\hat{S}_5$	Nd	$(\frac{1}{2},\frac{1}{2},\frac{1}{2})$ + F.C.
$\hat{S}_6 = \alpha \hat{S}_5$	Nd	$(\frac{1}{2},\frac{1}{4},\frac{1}{4})$ + F.C.
$\hat{S}_7$	Nd	$(\frac{1}{4},\frac{1}{2},\frac{1}{4})$ + F.C.
$\hat{S}_8 = \alpha \hat{S}_7$	Nd	$(\frac{1}{4},\frac{1}{4},\frac{1}{2})$ + F.C.

F.C. stands for the Face Centering operation $(0,0,0;\ 0,\frac{1}{2},\frac{1}{2};\ \frac{1}{2},0,\frac{1}{2};\ \frac{1}{2},\frac{1}{2},0)$

Using the atom positions and spin vectors defined in table 2.1 (neglecting face centering, which has no effect on the relative intensities of allowed reflections) one can write down the following expression for the magnetic structure factor

$$\vec{F}_{hkl} = 4\mu_{Mo} f_{Mo}(K)\left\{ \hat{S}_1^{\perp} \left(1 + \alpha e^{i\pi(k+l)/2} \right) + \hat{S}_3^{\perp} \left(e^{i\pi(l+h)/2} + \alpha e^{i\pi(h+k)/2} \right) \right\}$$

$$+ 4\mu_{Nd} f_{Nd}(K) \cos\left(\pi(h+k+l)\right)$$

$$\times \left\{ \hat{S}_5^{\perp} \left(1 + \alpha e^{i\pi(k+l)/2} \right) + \hat{S}_7^{\perp} \left(e^{i\pi(l+h)/2} + \alpha e^{i\pi(h+k)/2} \right) \right\} \qquad (2.20)$$

where

μ's are magnetic moments in μ_B

$\hat{S}_i$ = is a unit spin at site i

α = ± 1 is defined in Fig. 2.3

the factor 4 arises because the structure factor only includes $\frac{1}{4}$ of the unit cell.

The magnetic form factor for Nd^{3+} was taken from calculations of Stassis *et. al.*[St77] and Wilkinson's[Wi67] measured form factor for Mo^{3+} was used as an approximation for the Mo^{4+} form factor.

Models 1 to 3 were tested using the Rietveld profile refinement method with the above magnetic cross-section. Results are listed in table 2.2.

Table 2.2

Magnetic structural parameters obtained from Rietveld analysis.

Model	χ^2	μ_{Mo}	μ_{Nd}	μ^a_{NET}	θ_1	θ_2
11K						
1	2.5	2.07(11)	0.88(4)	0.80(12)	64(7)	83(10)
2	2.5	2.14(11)	0.88(2)	0	30(4)	4(6)
3	2.5	1.90(7)	0.96(8)	0	67(6)	101(11)
53K						
1	3.3	1.10(5)	0.95(4)	0.03(6)	41(15)	32(9)
2	3.3	1.70(3)	0.79(2)	0	62(4)	3(4)
3	3.5	1.41(3)	0.71(3)	0	44(3)	43(3)

$^a\mu_{NET}$ are per half formula unit.

Fig. 2.4 shows the profile fit for model 1 at 9 and 53K which is representative of the other fits.

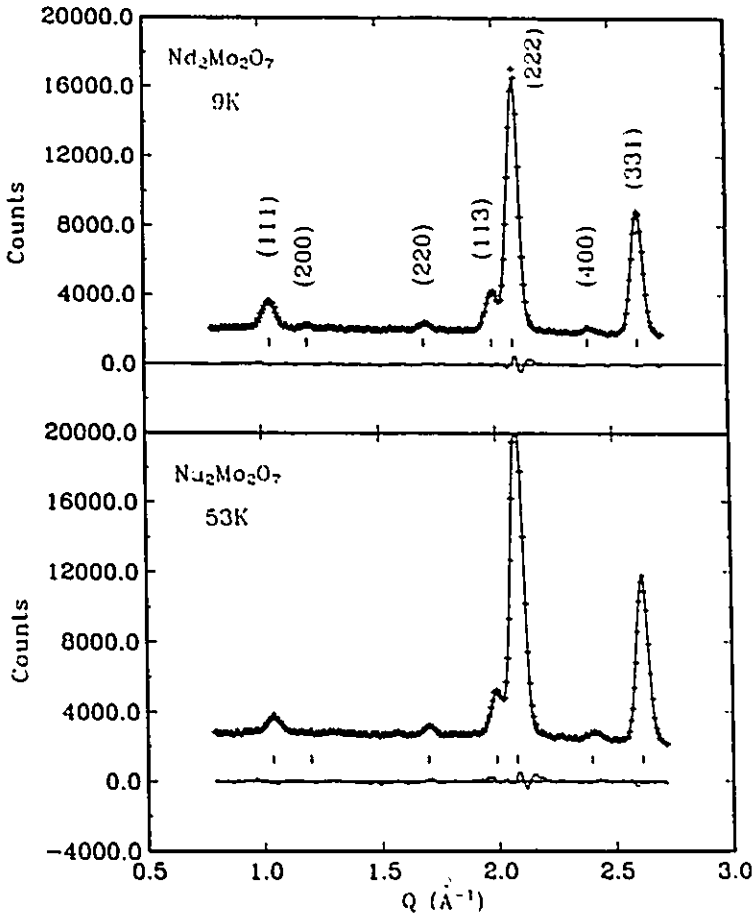

Fig 2.4. Observed (+), calculated (-) and difference profiles of the Rietveld fit to the neutron data for $Nd_2Mo_2O_7$ at 9k (top) and 53K (Bottom). Bragg angles are indicated by the vertical bars.

Because of the small amount of information contained in the data all models gave essentially the same χ^2 for the least squares fit. A very weak Bragg peak can be seen at the (200) position in the 9K data set, which is purely magnetic and was obscured in the difference plots. For Models 2 and 3 both Mo and Nd sublattices have no net moment which is not consistent with the spontaneous moment observed in the magnetization data between 20 and 90K. Thus model 1 which is a canted ferrimagnet is most likely correct at 53K in spite of the fact that the predicted net moment is very

small. On the other hand at 11K the magnetization data show a decreasing net magnetization which suggests the onset of one of the antiferromagnetic models (2 or 3). It is worth mentioning that restricted versions of model 1 with $\theta_1 = 0$ or $\theta_2 = 0$, at 53K were tested giving χ^2 values near 3.7 and net moments of .34 μ_B per half formula unit from the Nd moments.

2.2.2 $Mn_2Sb_2O_7$:

The sample was prepared by M. A. Subramanian[Su 84]. $Mn_2Sb_2O_7$ is actually a distorted form of pyrochlore with the distortion primarily along one of the cubic 3-fold axes. To a first approximation the space group is R$\bar{3}$m[Su 84] but further investigations have revealed even lower symmetry of $P3_121$[Sc 87] or P2[Gr 88] which are all successive sub-groups. Therefore the detailed structure of this compound is not known but it is a reasonable assumption that the magnetic sublattice of Mn^{2+} atoms forms a slightly distorted version of the corner-sharing tetrahedral lattice in normal pyrochlores. Scott[Sc87] has proposed a hexagonal structure, a = 7.191 Å and c = 17.398 Å, in the space group $P\,3_121$, based on X-ray diffraction data.

The 26K difference data for $Mn_2Sb_2O_7$ at 9K is shown in Fig. 2.5 showing numerous magnetic Bragg peaks. The Bragg peak intensities and positions are listed in Table 2.3.

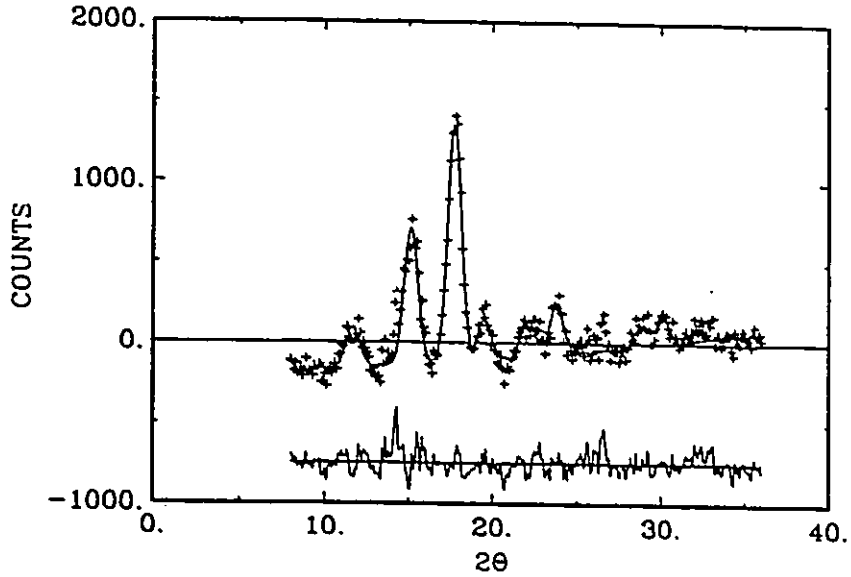

Fig 2.5 Neutron scattering data for $Mn_2Sb_2O_7$ at 9K with the 26K data subtracted. The bottom line shows the difference between the observed and calculated intensities.

Table 2.3

Magnetic Bragg peak positions and intensities for $Mn_2Sb_2O_7$ at 9K

	Pos (2θ)	d (Å)	Rel. Int.	(hkl)	Calc. Pos. (2θ)
1	11.44(2)	6.98(1)	17(1)	$(\frac{1}{2},0,2)$	11.20
2	15.13(2)	5.28(1)	58(2)	$(\frac{1}{2},0,3)$	15.21
3	17.73(1)	4.514(5)	100(2)	$(\frac{1}{2},\frac{1}{2},3)$	17.73
4	19.49(4)	4.11(1)	17(1)	$(\frac{1}{2},0,4)$	19.51
5	22.10(6)	3.63(2)	16(2)	$(\frac{1}{2},1,3)$	21.94
6	23.76(4)	3.37(1)	21(1)	$(\frac{1}{2},\frac{3}{2},1)$	23.70
				$(\frac{3}{2},0,3)$	23.78
7	28.82(7)	2.80(1)	10(1)	$(\frac{1}{2},1,5)$	28.79
8	30.13(6)	2.68(1)	11(1)	$(\frac{1}{2},2,1)$	30.03
				$(\frac{3}{2},0,5)$	30.24

All reflections could be indexed on a unit cell (2a,2a,c) or equivalently with a $(\frac{1}{2},\frac{1}{2},0)$ propagation vector, as related to Scott's hexagonal unit cell. The calculated peak positions within this indexing scheme are also listed in Table 2.3. The lack of detailed crystallographic information on this compound makes the solution of the magnetic structure rather difficult, thus no attempts have been made.

2.2.3 FeF_3 and $Y_2Mn_2O_7$:

$Y_2Mn_2O_7$ was prepared from MnO_2 and Y_2O_3 by M. A. Subramanian[Su88]. FeF_3 was prepared following De Pape [De86] with the assistance of M. A. Bjorgvinsson, by oxidation of $NH_4Fe_2F_6$ with bromine.

$$NH_4^+Fe^{2+}Fe^{3+}F_6^- + \tfrac{1}{2}Br_2$$
$$\rightarrow 2(NH_3)_z\,Fe^{3+}F_3^- + 2zHBr + (1\text{-}2z)NH_4Br,\ 0.03 \le z \le 0.35\,.$$

The excess ammonia was the removed under high vacumm at 250°C, leaving the pyrochlore form of FeF_3. Above 300°C pyr-FeF_3 reverts to a more stable, denser hexagonal form Htb-FeF_3.

The pyrochlore form of FeF_3[Fe 86] has lattice constant a = 10.232 Å with Fe atoms on the 16c site and fluorine at 48f in $Fd\bar{3}m$, the 16 d and 8a sites are unoccupied. Very little is known about magnetic ordering in pyrochlore antiferromagnets, In fact FeF_3 is the only such compound for which a low temperature antiferromagnetic structure has been observed[Fe 86]. Here the low temperature phase (below 16K) consists of four sub-lattices oriented along the four [111] directions, thus any two sub-lattices are oriented at 109° from each other as shown in Fig. 2.6.

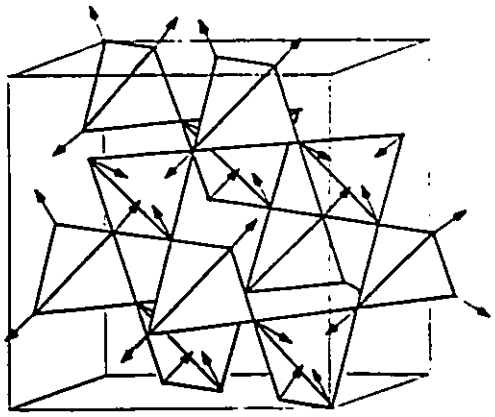

Fig. 2.6 The 109° magnetic structure of FeF_3[Fe86]

Data obtained elsewhere[Pa86] for $Y_2Mn_2O_7$ at 2.5K show very weak reflections at [111], [311] and near $[\frac{111}{222}]$.

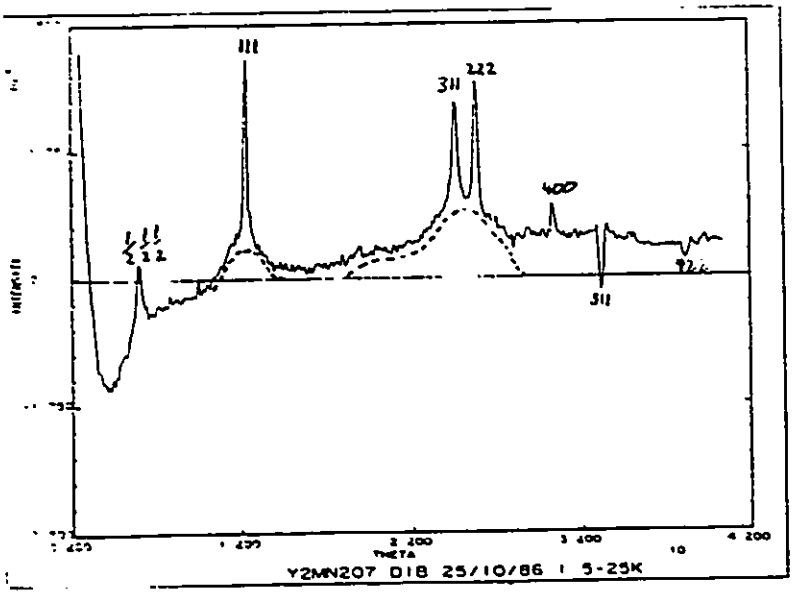

Fig 2.7 Neutron scattering data for $Y_2Mn_2O_7$ at 2.5K with the 25K data subtracted.

It is possible that the [111] and [311] reflections are nuclear in origin. The $[\frac{111}{222}]$ reflection could also be due to contamination from a small fraction of $\lambda/2$ neutrons in the incident beam. More careful analysis of these data is crucial. If these peaks are magnetic in origin then this is a very interesting result especially in light of the unusual behavior seen in $Y_2Mn_2O_7$ presented in chapter 3.

Chapter 3

Short Range Order

3.1 Introduction:

In the last chapter the two extremes of magnetic ordering were considered. At one end of the spectrum was long range ordering with $\xi = \infty$ (ξ is the correlation length) and sharp Bragg peaks in the neutron scattering cross section. The other extreme was the paramagnetic phase with $\xi = 0$ and a scattering cross section that is virtually independent of scattering vector $\vec{Q}$. Anything in between can be considered as short range ordering. However $\xi = 0$ to ∞ is a rather large interval and it would be useful to consider limiting cases where $\xi \approx 1$ (unit cell) and $\xi \approx \infty$. The first case $\xi \approx 1$ (unit cell) is similar to a liquid in that only correlations between the first and second coordination shells of neighbors are appreciable. When $\xi \approx \infty$ the system is very close to a critical phase transition and correlations can extend up to distances on the order of the crystal size.

3.1.1 Magnetic susceptibility:

The Curie-Weiss law derived in section 1.1.4 was said to be valid at high temperature. By high temperature I mean $T \gg J_0$ (the sum of exchange constants). Mean field theory predicts that when $T \approx J_0$ there occurs a phase transition from a pure paramagnetic phase to a long range ordered phase. This is wrong, especially for frustrated systems. In general real T_c's are lower than the mean field values since thermal fluctuations suppress ordering. Frustration will tend to depress T_c even more. Thus we might expect a wide temperature range $T_c < T < J_1$ (nearest neighbor

coupling) over which the Curie-Weiss law does not hold. In this region of temperature $\xi > 1$ but not close to infinity.

High temperature magnetic susceptibility data for $Mn_2Sb_2O_7$ were collected on a PAR vibrating sample magnetometer calibrated with high-purity nickel. All other susceptibility data were collected on a Quantum Design SQUID magnetometer calibrated with high-purity palladium. The samples were pressed into small pellets.

The magnetometers do not measure susceptibility directly. A field is applied and the magnetization is measured. The susceptibility is approximated by

$$\chi = \frac{\partial M}{\partial H} \approx \frac{M}{H}. \tag{3.1}$$

The approximation is good when M(H=0) = 0 and H is small (when H is large M(H) is usually non-linear in H). For a ferromagnet below T_c M(H=0) $\neq$ 0 and $\left.\frac{M}{H}\right|_{H=0}$ is undefined where $\left.\frac{\partial M}{\partial H}\right|_{H=0}$ is well defined and (3.1) breaks down completely. For antiferromagnets this will not be a problem.

One can also measure susceptibility of a sample in an oscillating applied field, which is called the ac-susceptibility. If the field frequency is ν then

$$H_\nu = H_o \sin(2\pi\nu t) \tag{3.2}$$

where t is the time. And we may expect the magnetization to behave like

$$M_\nu = M_o \sin(2\pi\nu t + \varphi) \tag{3.3}$$

$$= M'_\nu \sin\varphi + M''_\nu \cos\varphi \tag{3.4}$$

where the angle φ has been introduced to allow for the possibility that the M_ν is out of phase from H_ν. Now one can define a frequency dependent susceptibility

$$\chi_\nu = \frac{\partial M_\nu}{\partial H_o} = \chi'_\nu \sin\varphi + \chi''_\nu \cos\varphi \qquad (3.5)$$

where χ' and χ'' are the in phase and out of phase portions of the susceptibility respectively.

3.1.2 Neutron scattering $\xi = \infty$:

In the limit of large ξ we can use the results from chapter two for neutron scattering from long range ordered systems with one modification. The delta function in (2.5) and thus the Bragg condition for scattering (2.14) must be relaxed. The scattering will still be peaked at reciprocal lattice points with the width of the peak proportional to ξ^{-1}. For most systems, experiments as well as first order corrections to mean field theory, show that the scattering function has a Lorentzian line shape near reciprocal lattice points. Thus, neglecting any anisotropy we have

$$\frac{d\sigma}{d\Omega} \propto \frac{1}{\xi^{-2} + (\vec{Q}-\vec{K})^2}. \qquad (3.6)$$

Scattering close to T_c is called critical scattering.

3.1.3 Neutron scattering $\xi \approx 1$ (unit cell)

For many of the pyrochlore systems studied long range order has not been observed and the spin-spin correlations only extend out to the first few coordination shells of neighbors. Starting from the cross section in (2.2) it is useful to perform an angular average in $\vec{Q}$-space in order to obtain a scattering cross section for powders. As well it will be assumed that the spin-spin correlations are isotropic thus

$$\langle \vec{S}^{\perp}_{ia} \cdot \vec{S}^{\perp}_{jb} \rangle = \frac{2}{3} \langle \vec{S}_{ia} \cdot \vec{S}_{jb} \rangle . \tag{3.7}$$

After integrating (2.2) over all angles in $\vec{Q}$, and neglecting anisotropy in the form factors we have the radial cross section[Be67]

$$\frac{d\sigma}{d\Omega}(Q) = \frac{2}{3} (\tfrac{1}{2}\gamma r_o)^2 \sum_{ij} \sum_{ab} f_a(Q) f_b(Q) \langle \vec{S}_{ia} \cdot \vec{S}_{jb} \rangle \frac{\sin\left[Q|\vec{R}_{ai} - \vec{R}_{bj}|\right]}{Q|\vec{R}_{ai} - \vec{R}_{bj}|}$$

$$= \frac{2}{3} (\tfrac{1}{2}\gamma r_o)^2 N \sum_{b} \sum_{ia} f_a(Q) f_b(Q) \langle \vec{S}_{ia} \cdot \vec{S}_{0b} \rangle \frac{\sin\left[Q|\vec{R}_{ai} - \vec{r}_b|\right]}{Q|\vec{R}_{ai} - \vec{r}_b|} . \tag{3.8}$$

The Fourier transform of the radial cross section gives an approximation to the radial correlation function

$$g(r) = \int_{Q_l}^{Q_h} I_{diff}(Q)\, f^{-2}(Q)\, Q \sin(Qr)\, dQ . \tag{3.9}$$

where $I_{diff}(Q)$ is the magnetic scattering intensity at Q, with the paramagnetic scattering subtracted. In the limit of isotropic interactions

$$g(r) \propto \frac{1}{S(S+1)} \sum_{\vec{r}'} \langle \vec{S}_o \cdot \vec{S}_{\vec{r}'} \rangle \, \delta(|\vec{r}| - |\vec{r}'|) \tag{3.10}$$

which is a sum of spin-spin correlations at distance r. When $g(r) > 0$ the spins on average tend to be aligned parallel at distance r, and when $g(r) < 0$ the spins are

anti-parallel. The major limitation in this sort of analysis is the limited Q-range of the data. Other sources of error such as data noise and anisotropy (for the systems under study) are less significant.

3.1.4 Small Angle Neutron Scattering (SANS):

By using a longer wave length and measuring scattered neutrons at very small angles (small Q) one can obtain information about spin-spin correlations over large length scales. All of the above analysis concerning the scattering cross section applies. However for most samples the only Bragg reflection in this range of Q is the [000] reflection, which cannot be measured directly as it is in the direct beam of unscattered neutrons. Paramagnetic and diffuse scattering from short range order will certainly be observable.

SANS data were collected at MNR with 4.75$\mathring{A}$ neutrons from a pyrolytic graphite (PG) monochromator. The detector was a 128×128 element 2D-PSD providing useful data in the range $0.016\ \mathring{A}^{-1} \leq Q \leq 0.2\ \mathring{A}^{-1}$. Data sets at 300, 50, 30, 25, 20, 16, 12, 8K for $Tb_2Mo_2O_7$ and at 200, 160, 100, 95, 80, 50, 17, 15, 12, and 10K for $Nd_2Mo_2O_7$[Ba89] were collected.

3.2 $A_2B_2O_7$ Systems With One of A or B magnetic:

3.2.1 $Y_2Mn_2O_7$:

Susceptibility and heat capacity data have been measured elsewhere[Su88][Kr89][Re90a]. A summary of the results will be presented here.

For T > 125K, χ_{iso} follows the Curie-Weiss (CW) law with C = 1.84(2) emu·K/mole implying an effective magnetic moment of $\mu_{eff} = 3.84(2)\mu_B$ or a spin value of $S = \frac{3}{2}$ as expected for Mn^{4+}. The paramagnetic Curie temperature was found to be θ_c = 41(2)K and indicates predominant ferromagnetic exchange interactions between Mn moments. For T < 125K deviations from the CW law appear. Below about 20K a sudden rise in the magnetization is seen but the data are strongly dependent on the thermal history and the applied magnetic field (Fig. 3.1).

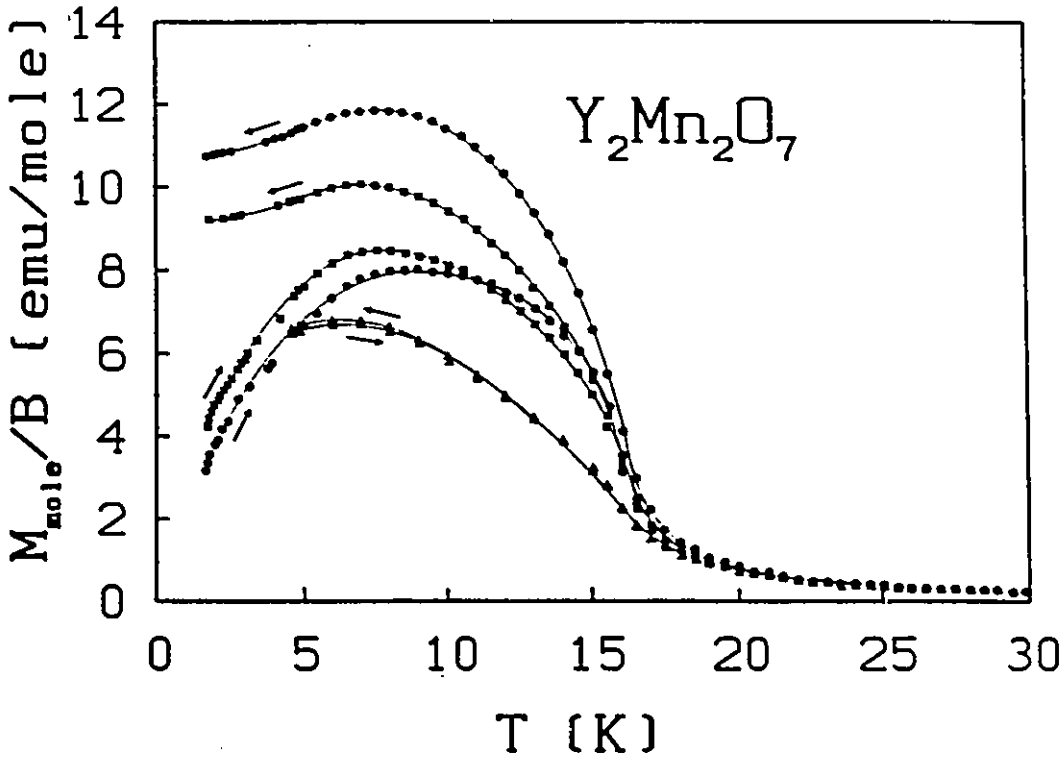

Fig 3.1 Field cooled (fc: ↤) and zero field cooled (zfc: ↦) dc-susceptibility of $Y_2Mn_2O_7$ per Mn atom. (·) .15 mT, (□) .56 mT and (△) 10 mT[Kr89][Re90a].

A remnant magnetization (splitting of the *zfc* and field cooled (*fc*) magnetization) is observed for small fields $B_{ext} < 10$ mT. While the *fc* magnetization displays a weak maximum and saturates at a slightly lower value as $T \to 0$, the *zfc* data go through a broad maximum and tend to zero. With increasing field the rise becomes flatter and the maxima decrease. The maximum shifts to lower temperatures and the splitting of *fc* and *zfc* susceptibility is reduced upon increasing field. The difference between *zfc* and *fc* susceptibility has almost completely vanished for $B_{ext} = 10$ mT.

High field measurements (not shown) give magnetization curves similar to ferromagnetic behavior with spontaneous magnetization below a Curie temperature of about 20K. However complete saturation cannot be achieved at 1.8K in a field of 4T.

The magnetic moment per Mn atom is $2.3\mu_B$ and still considerably lower than $3\mu_B$ as expected for $S = \frac{3}{2}$.

Ac susceptibility results are shown in Fig. 3.2.

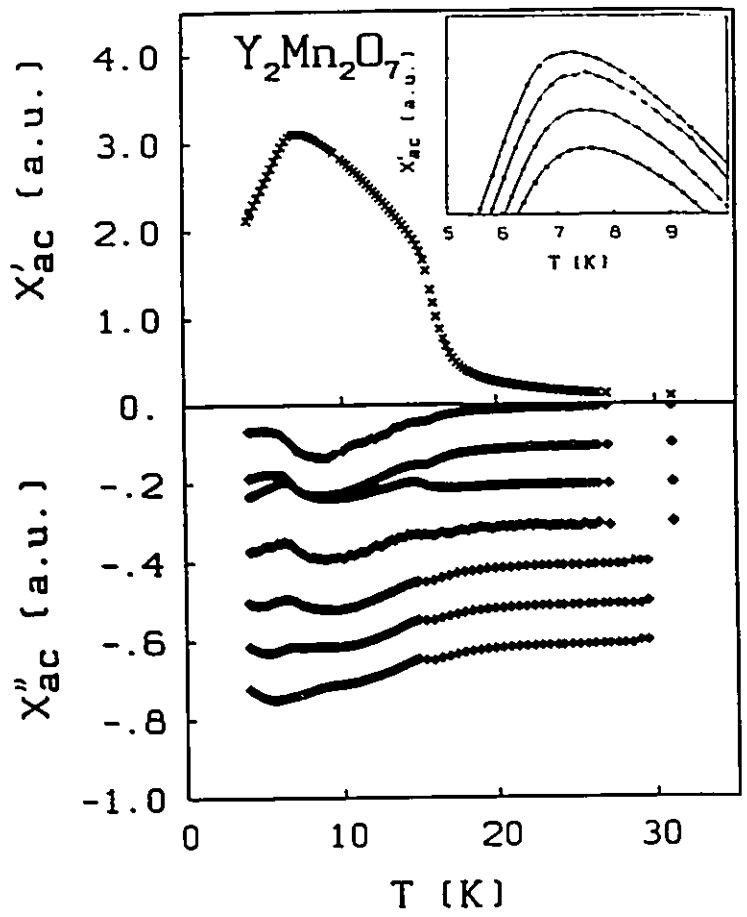

Fig. 3.2 ac-susceptibility of $Y_2Mn_2O_7$. top) χ' at 20Hz. The inset shows the χ' maxima for various frequencies, from top to bottom: 20Hz, 100Hz, 200Hz and 1000Hz. bottom) χ'' at various frequencies, from top to bottom: 20Hz, 40Hz, 80Hz, 100Hz, 200Hz, 500Hz and 1000Hz. Each curve was shifted by -0.1 compared to the to the preceding one[Kr89][Re90a].

$\chi'(T)$ has some basic features in common with the dc-susceptibility, *i.e.* the relatively sharp rise below about 20K and the maximum at about 7K. Compared to the

dc-susceptibility, however, the maximum is more pronounced and the data above the maximum fall into two ranges with different slopes. The slope change happens at about 15.5K and simultaneously a kink in χ'' is generated. The maxima temperatures are frequency dependent and shift to higher temperatures with increasing frequency.

The magnetic portion C_m of the heat capacity for $Y_2Mn_2O_7$ (the lattice part was removed by subtracting the heat capacity for $Y_2Sn_2O_7$) shows no sharp anomaly usually associated with long range magnetic ordering (Fig. 3.3).

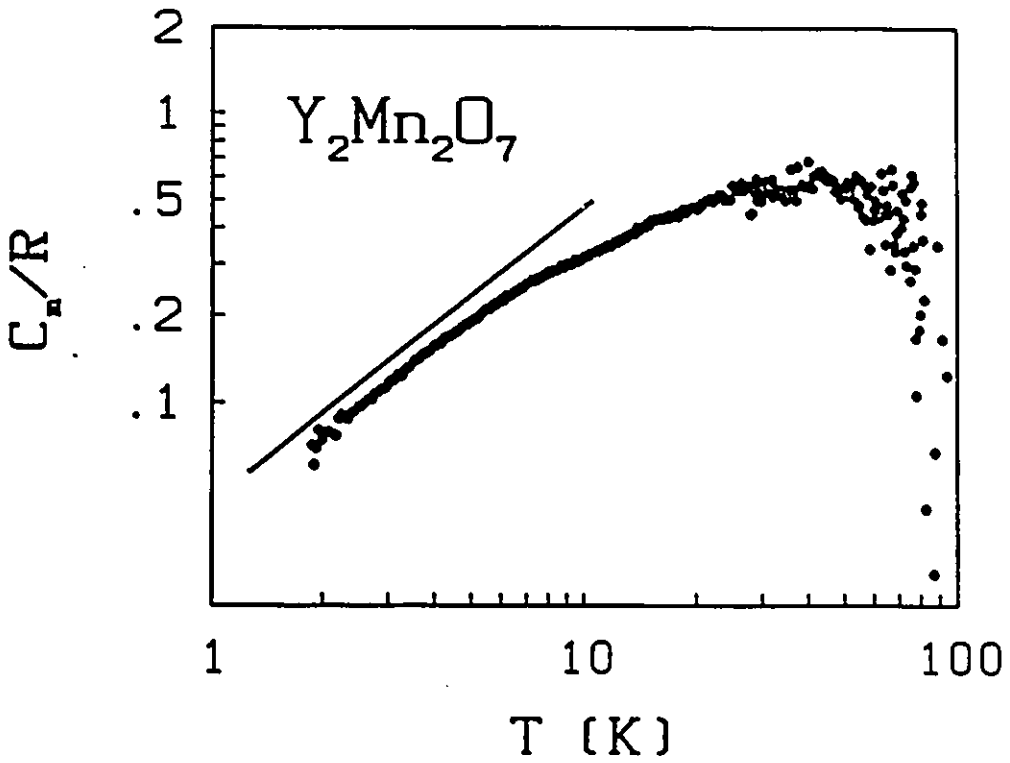

Fig. 3.3 Magnetic part C_m of the heat capacity for $Y_2Mn_2O_7$[Kr89][Re90a].

A broad maximum of C_m is centered around 40K. At low temperatures, $T < 7K$, C_m follows a T^1 power law. The change in slope at 7K corresponds to the maximum in χ_{dc} and χ'_{ac}.

The integrated entropy

$$S(T) = \int_0^T \frac{C_m}{T} dT \qquad (3.11)$$

smoothly increases and almost saturates towards high temperatures. The saturation value 1.35 R is in good agreement with Rln4 expected for an $S = \frac{3}{2}$ magnetic system. At 18.4K where the magnetization data pointed to spontaneous magnetization the entropy which has already been removed by short range magnetic order amounts to about 55%.

No clear evidence for magnetic Bragg peaks was observed in the present study down to 7K as seen in Fig. 3.4 which shows the low temperature data sets with the 200K data subtracted.

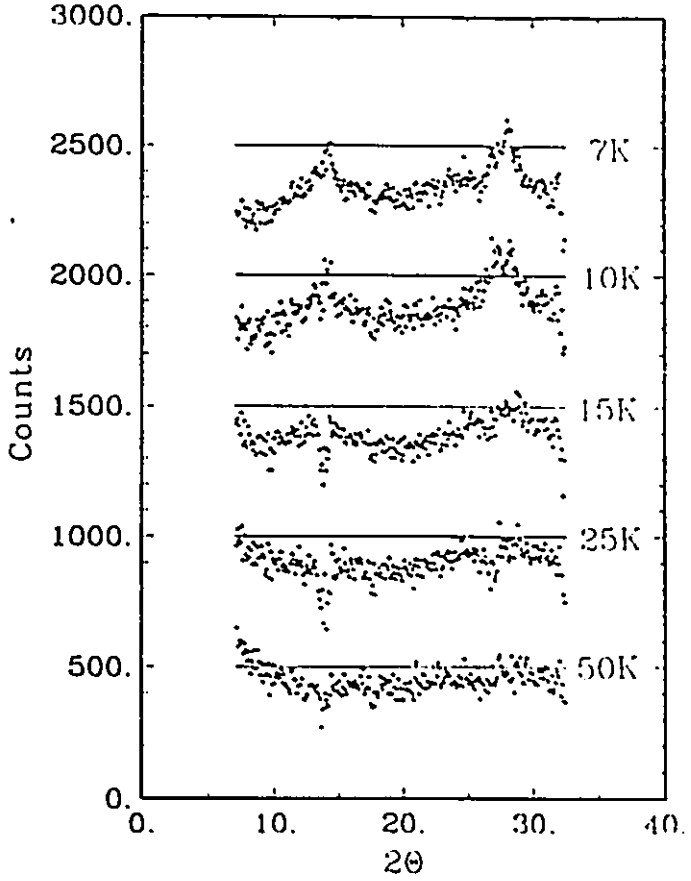

Fig 3.4 Low temperature neutron diffraction data for $Y_2Mn_2O_7$ after subtracting the 200K data. The data sets are offset for clarity.

As the temperature is lowered the magnetic scattering is seen to concentrate more and more near 14° and 27° in 2θ, which corresponds to d-spacings of 5.7 and 3.0 Å respectively. One can see by inspection that the Q-integrated scattering for all data sets is negative. This means that there must be a buildup of positive scattering somewhere outside the range of the data.

Better insight into the short range correlations can be obtained by Fourier transforming the data according to (3.9). Fig. 3.5 shows the Fourier transforms of the five low temperature data sets.

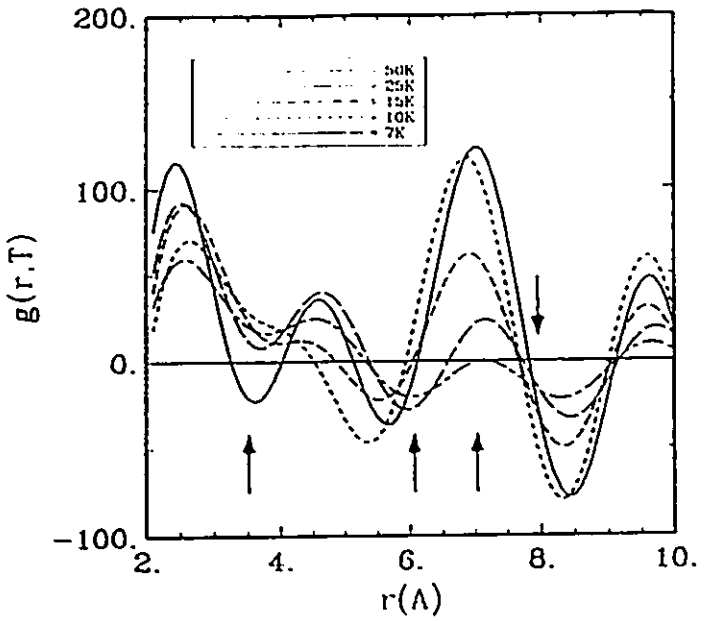

Fig 3.5 Real space radial correlation function (in arbitrary units) for $Y_2Mn_2O_7$ at various temperatures.

The arrows indicate the first four neighbor Mn-Mn bond distances. One can see that from 50K down to 10K ferromagnetic correlations are developing for the second and third coordination shells. This is consistent with the apparent ferromagnetic behavior observed in the high temperature susceptibility. As a result of the highly frustrated nature of nearest neighbor interactions on the Mn sublattice, only below 10K is there any evidence for antiferromagnetic correlations for the first neighbor coordination shell.

Thus we see that the presence of further neighbor ferromagnetic interactions can give misleading results for magnetic susceptibility data. In particular the CW behavior at high temperatures and magnetization data from 10 to 20K are both consistent with ferromagnetism. However below 10K both the ac and dc susceptibility decrease as T $\rightarrow$ 0, for *zfc* samples, clearly indicating the presence of antiferromagnetic interactions. The inability of the magnetization to saturate at 1.8K gives further support to this

argument.

A number of results obtained on $Y_2Mn_2O_7$ are very similar to those found in conventional spin glasses. These include 1) sample history dependence in the susceptibility, 2) frequency dependence of χ'(max), 3) absence of features associated with long range order in the heat capacity but the observation of a power law at low temperatures, 4) removal of almost all the magnetic entropy by 2K without long range order.

3.2.2 FeF_3:

The high temperature susceptibility has been described elsewhere[Fe 86] and will not be discussed further here except to say that no Curie-Weiss law behavior is observed up to 300K. Below 120K the high field susceptibility (1T) shows a broad maximum at 85K (Fig. 3.6) which is most likely a result of short range ordering of the Fe^{3+} moments.

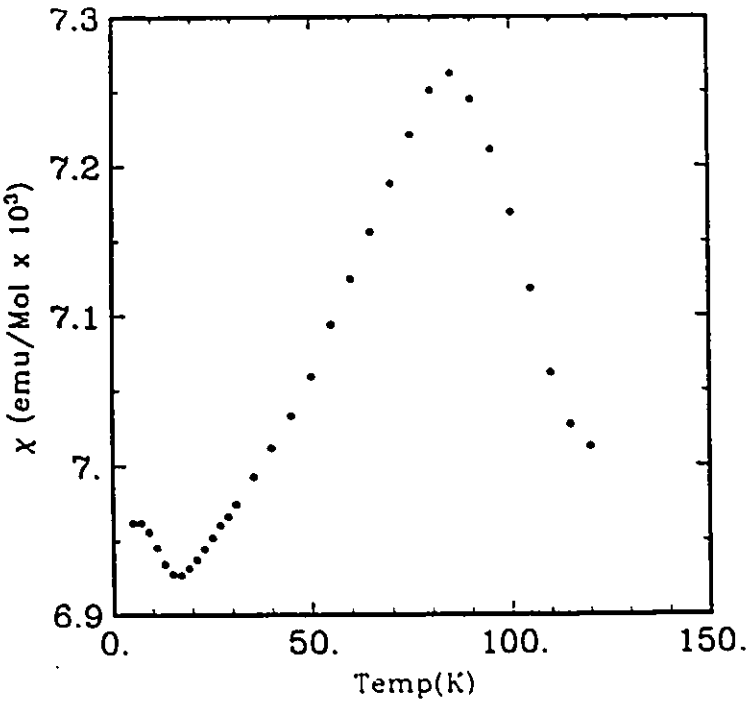

Fig 3.6 Low temperature susceptibility data for FeF_3 measured at an applied field of 1T on a residual field cooled sample

The minimum at 16K coincides with the temperature where long range order sets in.

Further evidence for strong short range correlations is furnished by sample history dependence at lower temperatures. To see the history dependence the sample is cooled from the starting temperature down to 5K in a high field (1T). The field is then reduced to 0.01T and the sample is measured while warming, cooled again and remeasured, with the field fixed at 0.01T. This procedure ensures that the high field cooled (*hfc*) and low field cooled (*lfc*) runs are both measured with the same applied field. Fig. 3.7 shows the results for a starting temperature of 300K.

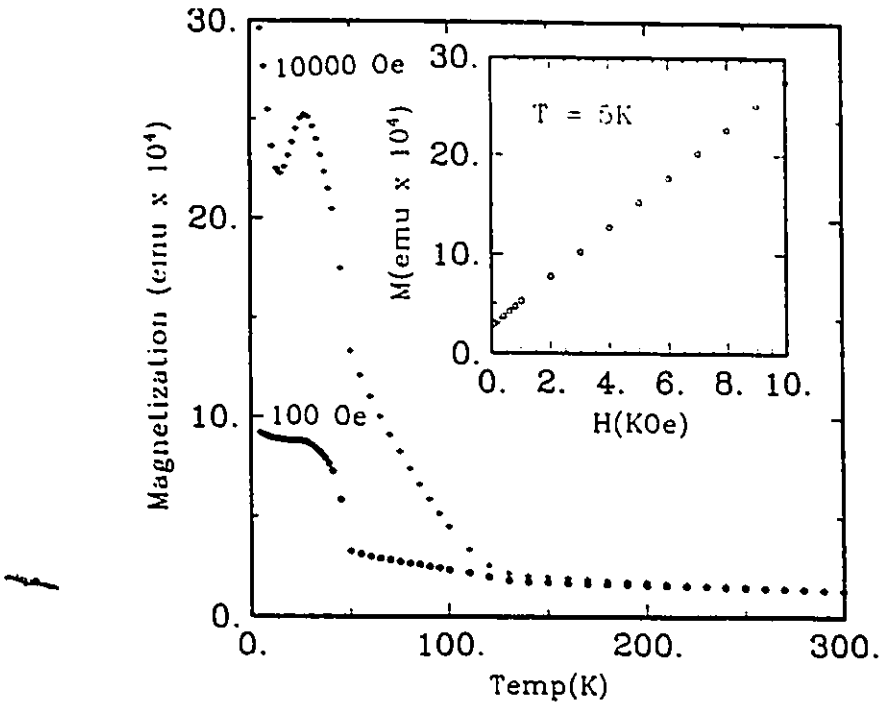

***Fig. 3.7** Magnetization data for FeF_3 showing sample history dependence. The inset shows the linear behavior of the magnetization with applied field.*

The history dependence is seen to persist up to 130K which is an order of magnitude higher than 15.5K where long range order sets in. Just below 50K another sharp feature can be seen in both the *hfc* and *lfc* runs. The inset in Fig. 3.7 shows the linear behavior of the magnetization with field at 5K, indicating that the relaxation time in the sample is smaller than the time scale of the experiment. Fig. 3.8 is similar to Fig. 3.7, with a starting temperature of 70K, *i. e.* here the sample was cooled in residual field (≈ 2mT) to 70K before ramping the field up to 1T.

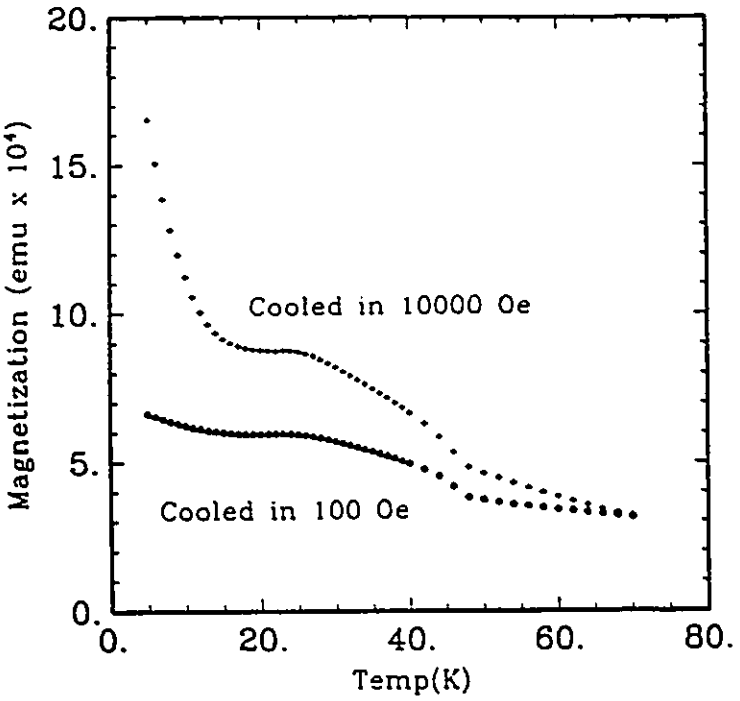

Fig. 3.8 As in Fig. 3.7 with a starting temperature of 70K which is inside the short range order regime.

Again the sharp feature below 50K is present, however the strong maximum at = 30K in the *hfc* run has been reduced to a plateau. This dramatic history dependence of the magnetization is believed to be due to the onset of strong short range correlations below about 130K and the high degree of frustration.

Low temperature neutron diffraction data sets are shown in Fig. 3.9, the room temperature (273K) data set was subtracted thus removing nuclear and paramagnetic scattering.

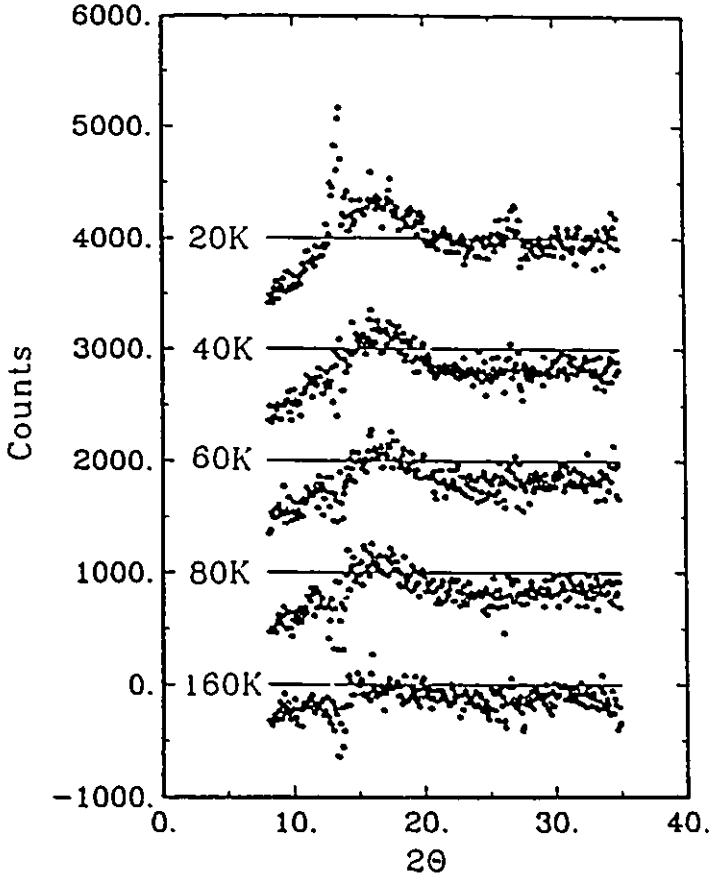

Fig 3.9 Neutron scattering data for FeF_3 showing diffuse scattering due to short range correlations of Fe^{3+} moments

The roughening in the data at about 13° in 2θ is due to the presence of a very strong nuclear [111] Bragg reflection. At 20K one can see that a small amount of Bragg scattering (approximately 5% of the original peak) is left over after the subtraction which can be attributed to either changes in the nuclear Debye Waller factor, or magneto-striction effects.

The dominant feature in these data sets is the broad feature at ≈15° in 2θ and depletion of scattering near 10° 2θ, resulting from short range ordering of the Fe^{3+} moments. Significant short range ordering sets in below 160K which is consistent with susceptibility data. Fig. 3.10 shows the Fourier transforms of the five low temperature data sets.

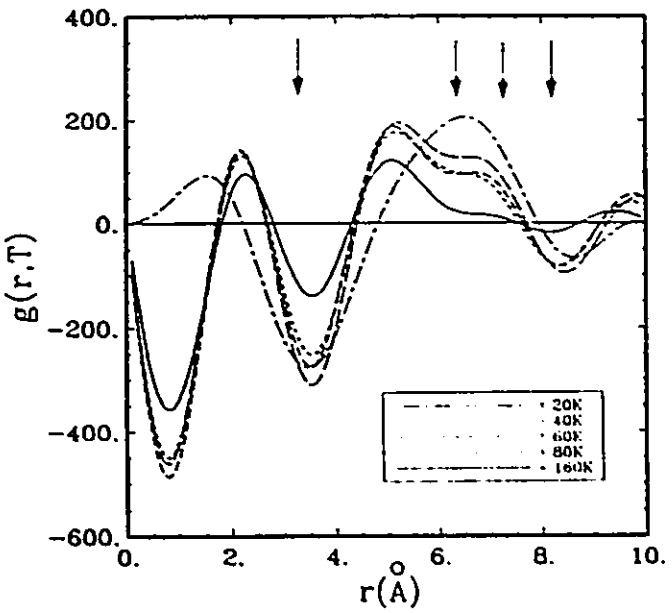

Fig. 3.10 Real space radial correlation functions for FeF_3 (in arbitrary units). Arrows indicate the four nearest neighbor bond distances for the Fe^{3+} sub-lattice

The arrows indicate the first four neighbor Fe-Fe bond distances. We can see that there are strong antiferromagnetic correlations between first neighbors at all temperatures. Below 80K ferromagnetic correlations between second and third neighbors develop. Also the 20K data set shows qualitative differences from all the other data sets. The resolution provided by this analysis is not good enough to separate the contributions from the second and third neighbor correlations.

3.2.3 $Mn_2Sb_2O_7$:

Fig. 3.11 shows a Curie-Weiss law plot of the susceptibility data (corrected for diamagnetism) at an applied field of 1T for $Mn_2Sb_2O_7$, in the temperature range 50-100K.

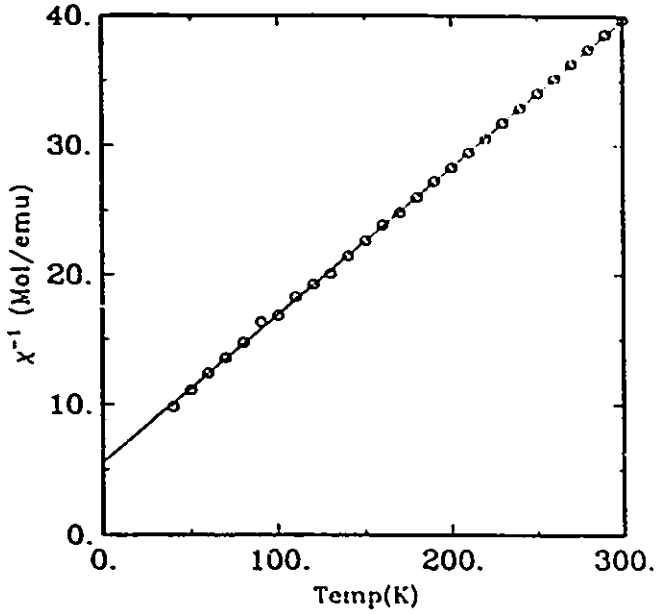

Fig. 3.11 Curie-Weiss law fit to the inverse susceptibility data for $Mn_2Sb_2O_7$ giving μ = 5.92(1) μ_B and θ = -48.9(6)K.

The least-squares fit yielded an effective moment μ = 5.92(1) μ_B as expected for S = $\frac{5}{2}$, and θ = -48.9(6)K indicating predominantly antiferromagnetic interactions. Below 50K the data show deviations from Curie-Weiss behavior indicating the onset of short range order.

Fig. 3.12 shows the sample history dependence for $Mn_2Sb_2O_7$ magnetization data, obtained by employing the same procedure used for FeF_3 with a starting temperature of 70K.

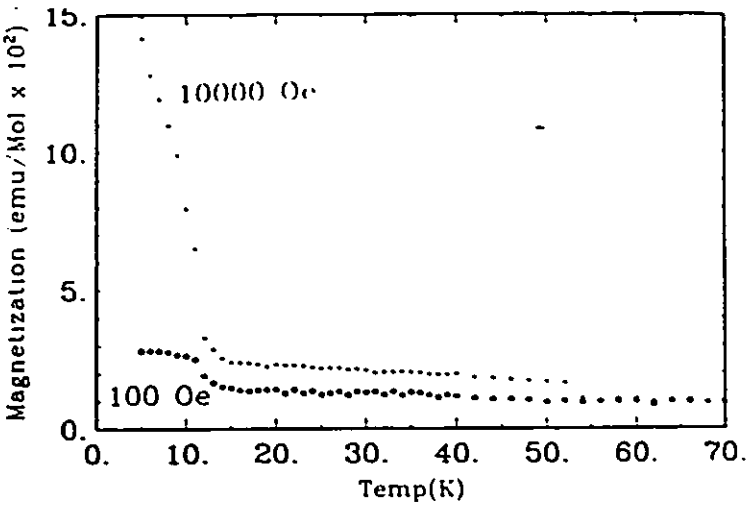

Fig. 3.12 Magnetization for $Mn_2Sb_2O_7$, following the procedure employed for FeF_3, showing sample history dependence below about 55K.

Again the history dependence persists up to 55K far above the long range ordering temperature of 13K. Thus we have evidence for the onset of short range correlations below about 55K.

The neutron scattering data (with the 300K data subtracted) for $Mn_2Sb_2O_7$ (Fig. 3.13) is very similar to that of FeF_3 for the higher temperatures, again having the broad feature near $2\theta = 15^{\circ}$.

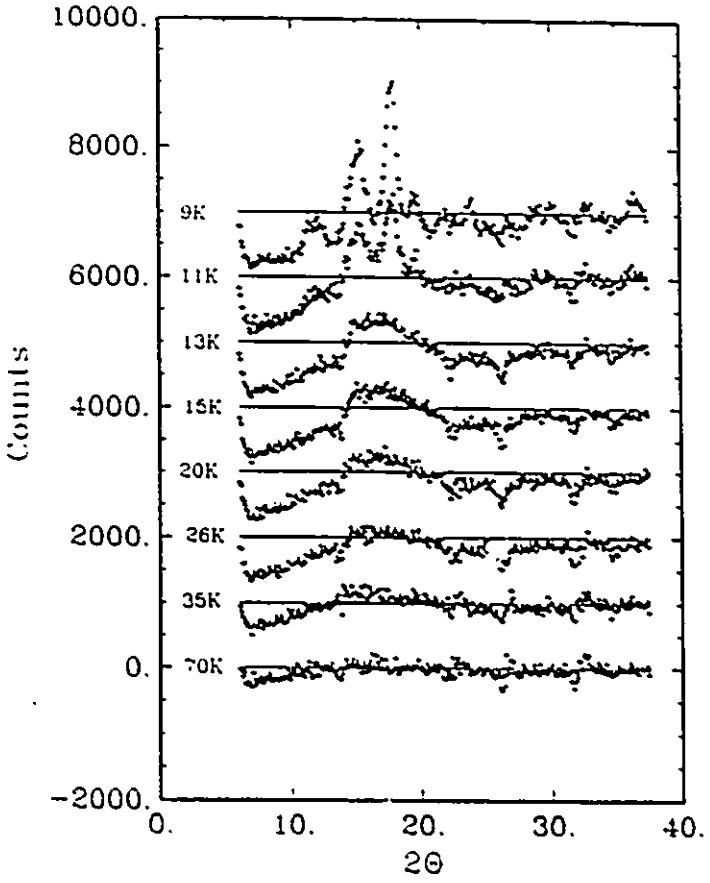

***Fig. 3.13** Neutron scattering data for $Mn_2Sb_2O_7$ showing diffuse scattering due to short range correlations of Mn^{2+} moments*

Below 13K, resolution limited magnetic Bragg peaks discussed in chapter 2, begin to develop. Again the Fourier analysis (Fig. 3.14) indicates strong antiferromagnetic first neighbor, and ferromagnetic second and third neighbor, spin-spin correlations.

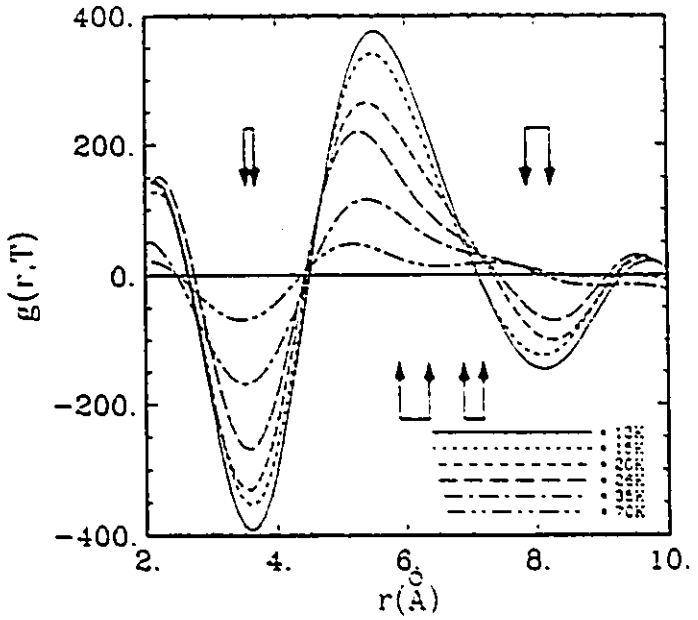

Fig 3.14 Real space radial correlation functions for $Mn_2Sb_2O_7$ (in arbitrary units). Arrows indicate upper and lower limits on the four nearest neighbor coordination shells in the Mn^{2+} sub-lattice

Here the coordination shells are defined w.thin a range of bond distances calculated from Scott's refinement of the crystal structure in the space group $P3_121$[Sc87].

3.2.4 $Y_2Mo_2O_7$:

The sample was prepared by M. Sato[Sa86]. Previous susceptibility measurements on $Y_2Mo_2O_7$ [Gr 86](Fig. 3.15) show classic spin glass behavior in the form of a cusp in χ at 22K and marked sample history dependence below 22K.

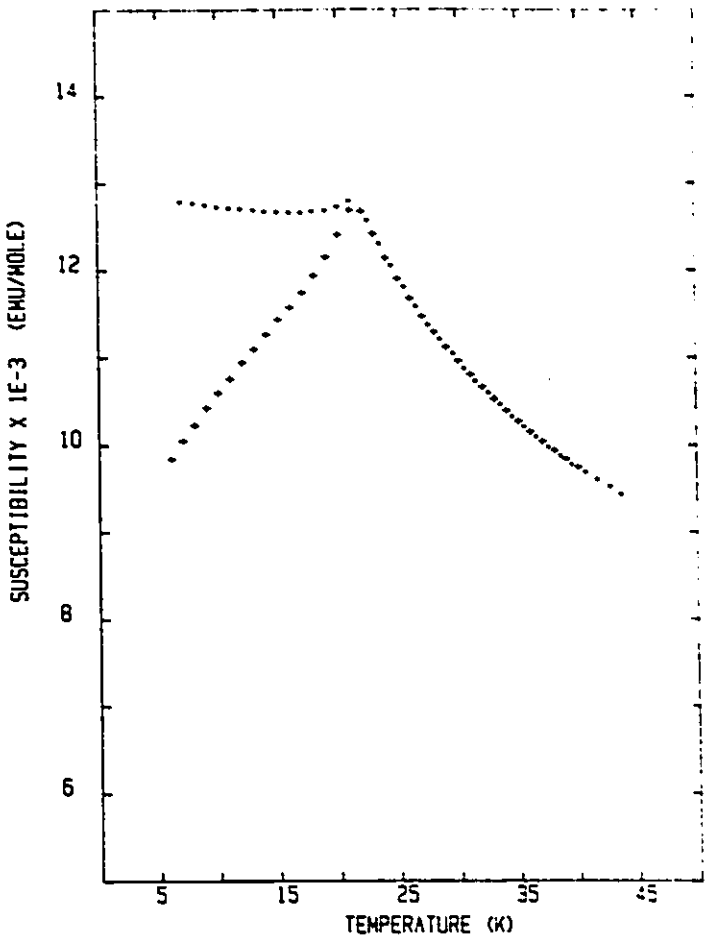

Fig. 3.15) ***D.c. susceptibility for $Y_2Mo_2O_7$ measured at 0.01T, (+) zero field cooled and (·) field cooled[Gr86].***

As is it generally believed that spin glasses must have some chemical disorder and the question as to the degree of crystallinity in $Y_2Mo_2O_7$ naturally arises. However a careful neutron diffraction study at room temperature[Re88] showed no evidence for chemical disorder. In particular cation disorder can be ruled out on the basis of bond distance arguments. Also attempts to refine the structure with oxygen disorder were not successful.

The subtracted 9K and 24K data sets are shown in Fig. 3.16.

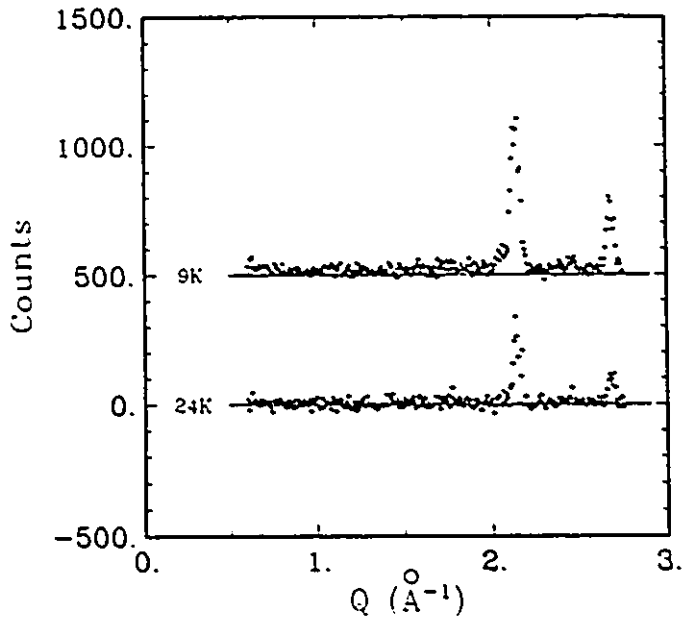

Fig 3.16 Low temperature wide angle neutron diffraction data for $Y_2Mo_2O_7$ after subtracting the 150K data.

No obvious signs of diffuse magnetic scattering are visible in the background for either data set. However resolution limited peaks are present at the (113) and (331) Bragg angles. The intensity of these peaks are on the order of 5 to 10% of the un-subtracted nuclear peaks and increase with decreasing temperature. The relative intensities are in accord with the relative intensities of the original nuclear peaks. Also there is no possible magnetic structure that is consistent with the absence of the (111), (200) and (220) reflections simultaneously (see appendix A for details). Thus we conclude that the origin of the peaks is purely nuclear and could possibly be explained in terms of changes in thermal vibration with temperature. The lack of evidence for long range order is consistent with the previous results indicating the presence of a spin glass phase. Any diffuse scattering that may be present due to short range ordering of the Mo moments will probably be unobservable due to the small Mo^{4+} moment. This null

result for $Y_2Mo_2O_7$ will however be quite useful in interpreting the diffuse scattering results for $Tb_2Mo_2O_7$ discussed next.

3.3 $A_2B_2O_7$ Systems With Both A and B magnetic:

3.3.1 $Tb_2Mo_2O_7$:

The sample was prepared by S. L. Penny following the procedure of M. Sato[Sa 86]. Dc magnetization data[Pe89b][Gr90a] (applied field = 2mT) are shown in Fig. 3.17, the behavior is similar in many respects to that normally found for spin glasses. The dc magnetization is independent of sample cooling history above 25K.

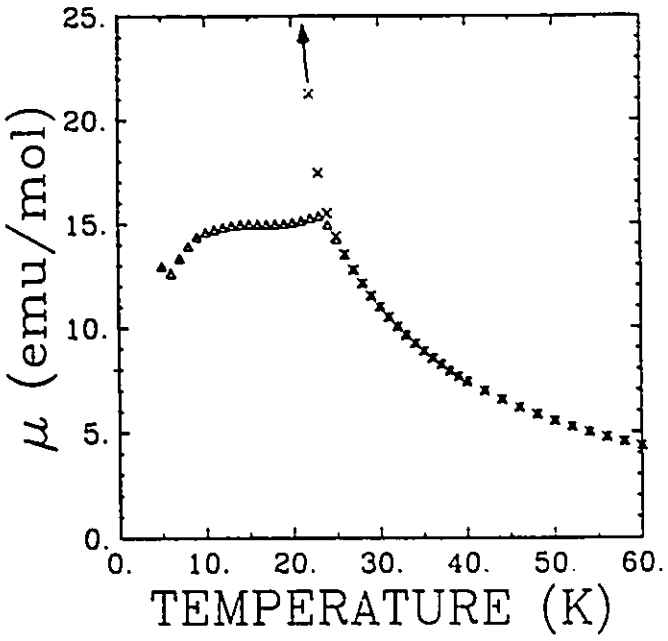

Fig. 3.17 Magnetic moment versus temperature for $Tb_2Mo_2O_7$ at an applied field of 0.002T: Δ - zero-field cooled; × - cooled in 0.1 T[Pe89b][Gr90a].

Below this temperature the magnetization becomes history dependent, displaying a cusp or weak maximum for the zero-field-cooled data and diverging for the field-cooled case. This is consistent with the magnetization results from Ali *et.al.*[Al 89]. However the data of Ali *et.al.* were measured at a slightly higher applied field

(0.01T) and no maximum was observed. Thus small fields are sufficient to destroy the antiferromagnetism in the material.

Neutron scattering data sets for various temperatures[Pe89b][Gr90] are shown in Fig. 3.18.

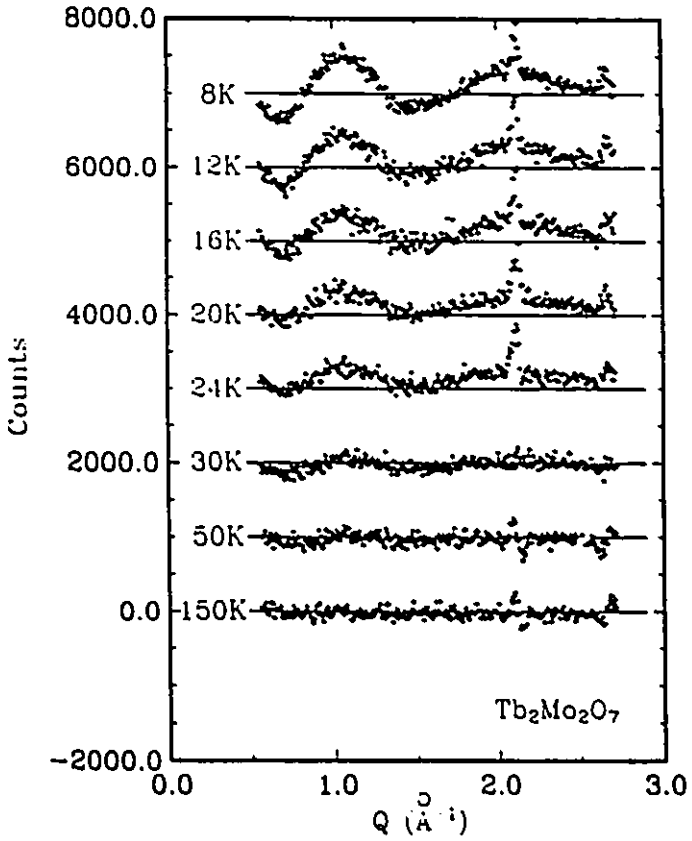

Fig. 3.18 Low temperature wide angle neutron diffraction data for $Tb_2Mo_2O_7$ after subtracting the 300K data[Pe89a][Gr90a].

As before the high temperature data (273K) has been subtracted. Below 30K broad features appear near Q = 1 and 2 $\mathring{A}^{-1}$, as the temperature was lowered the intensity of the features increased whereas the half-width remained constant. The resolution limited scattering near Q = 2.1 and 2.7 $\mathring{A}^{-1}$ is again believed to be purely nuclear in

origin for the reasons described above. It is interesting to note that the peaks disappear right at the spin-freezing temperature 25K.

The Fourier transformed data are shown in Fig. 3.19 with the first four neighbor bond distances indicated.

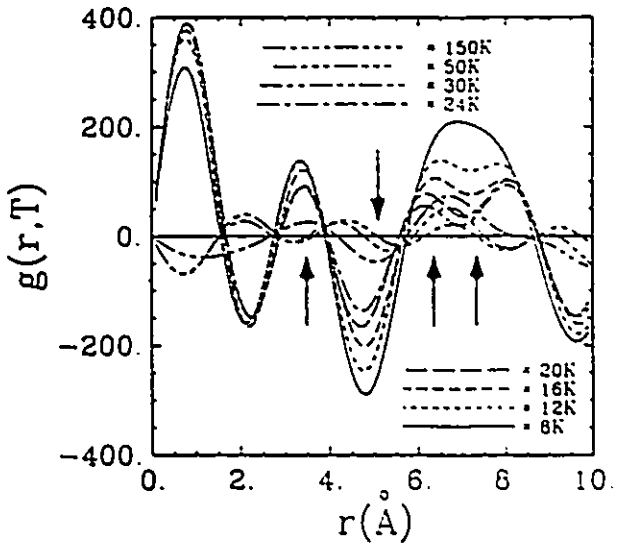

Fig. 3.19 Real space radial correlation function (in arbitrary units). Arrows indicate the fours nearest coordination shell distances for the metal atoms.

Only the second neighbor correlations are net antiferromagnetic. An abrupt change in the qualitative features of the correlation function occurs between 24 and 30K which is in accord with the onset of spin-glass-like behavior at 25K from the magnetization results.

Because the scattering is so strong more quantitative results can be obtained by modeling the subtracted data with the cross section (3.8), applied here to the pyrochlore system.

$$I(Q) = N\left[\tfrac{1}{2}\gamma r_o f_m(Q)\right]^2 \tfrac{2}{3} \sum_{i=1}^{4} c_i \gamma_i \frac{\sin QR_i}{QR_i} \qquad (3.12)$$

where

$$\gamma_1 = 2\langle Tb \cdot Mo\rangle_{R1} + \langle Tb \cdot Tb\rangle_{R1} + \langle Mo \cdot Mo\rangle_{R1} \qquad (3.13a)$$

$$\gamma_2 = 2\langle Tb \cdot Mo\rangle_{R2} \qquad (3.13b)$$

$$\gamma_3 = 2\langle Tb \cdot Mo\rangle_{R3} + \langle Tb \cdot Tb\rangle_{R3} + \langle Mo \cdot Mo\rangle_{R3} \qquad (3.13c)$$

$$\gamma_4 = \langle Tb \cdot Tb\rangle_{R4} + \langle Mo \cdot Mo\rangle_{R4} . \qquad (3.13d)$$

The summation is over coordination shells from a central atom and the R_i and c_i are bond distances and numbers of neighbors known from crystallographic data. Only the sum of correlations at each bond distance can be determined from the data. Of course one would expect γ_1, γ_3 and γ_4 to be dominated by Tb-Tb correlations as the Tb moment is about nine times larger than the Mo moment. In fact the lack of diffuse scattering for $Y_2Mo_2O_7$ indicates that <Mo·Mo> correlations can be neglected in this analysis. It is for this reason that the difference between the magnetic form factors for Tb^{3+} and Mo^{4+} was ignored in cross section. Figure 3.20 (top) shows the temperature dependence of the four γ values, determined by fitting the subtracted data with the above cross section.

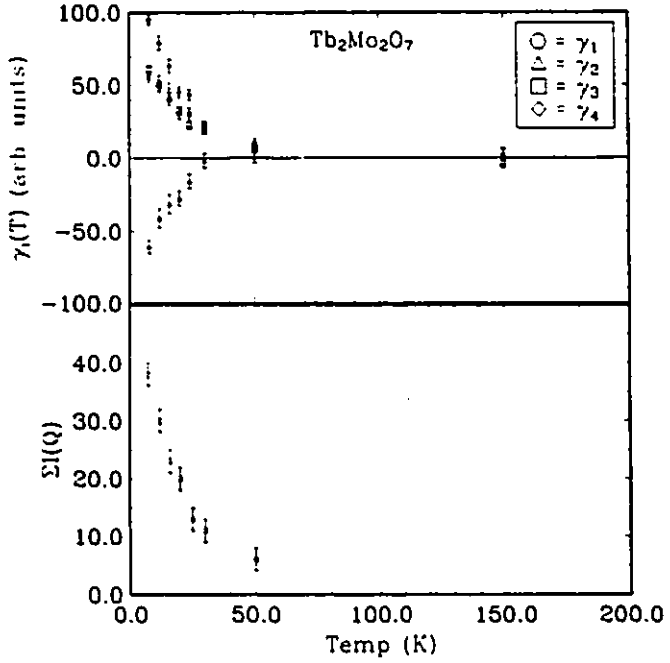

Fig. 3.20 Top: Temperature dependence of the correlation coefficients (see text) obtained by profile fitting the subtracted data for $Tb_2Mo_2O_7$ at each temperature. Bottom: temperature dependence of the Q-integrated magnetic SANS data.

The absolute values of the γ_i increase sharply below about 25K. Only γ_2, corresponding to the Tb-Mo coupling is negative.

SANS data difference plots (Fig 3.21) show enhanced scattering only for Q > 0.04 $\mathring{A}^{-1}$.

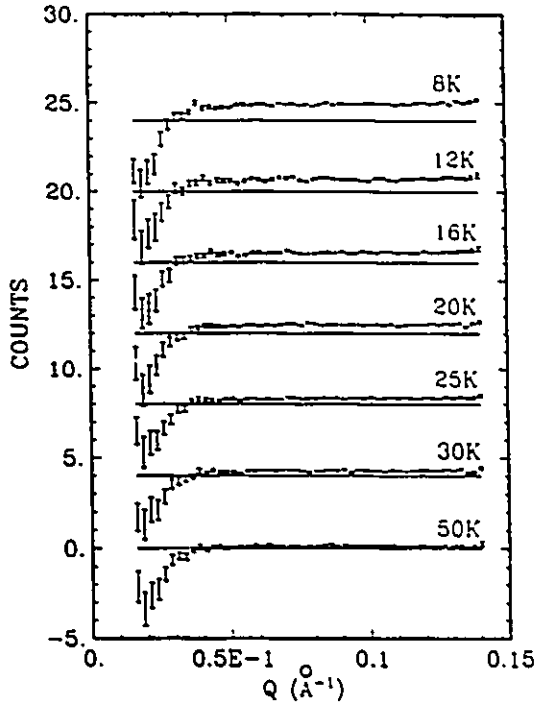

Fig. 3.21 SANS data for $Tb_2Mo_2O_7$ with the 300K data subtracted.

The temperature dependence of this excess SANS (Fig. 3.20 bottom) follows closely that of the correlation coefficients. The fact that the magnetic SANS occurs only for high Q provides reinforcement of the conclusion, drawn from the analysis of the diffuse scattering, that antiferromagnetic exchange predominates in this material.

The wide angle scattering was remeasured[Ga90] on a triple-axis instrument with the analyzer set to zero energy transfer in order to check that the static approximation employed in the above analysis is valid. The results show that the Q-dependence of the diffuse scattering remains qualitatively similar to that of the energy integrated scattering in Fig. 3.18.

Energy scans at various temperatures[Ga90][Gr90a] are shown in Fig. 3.22 for $Q = 1.05\ \text{Å}^{-1}$ where the diffuse magnetic scattering is strongest.

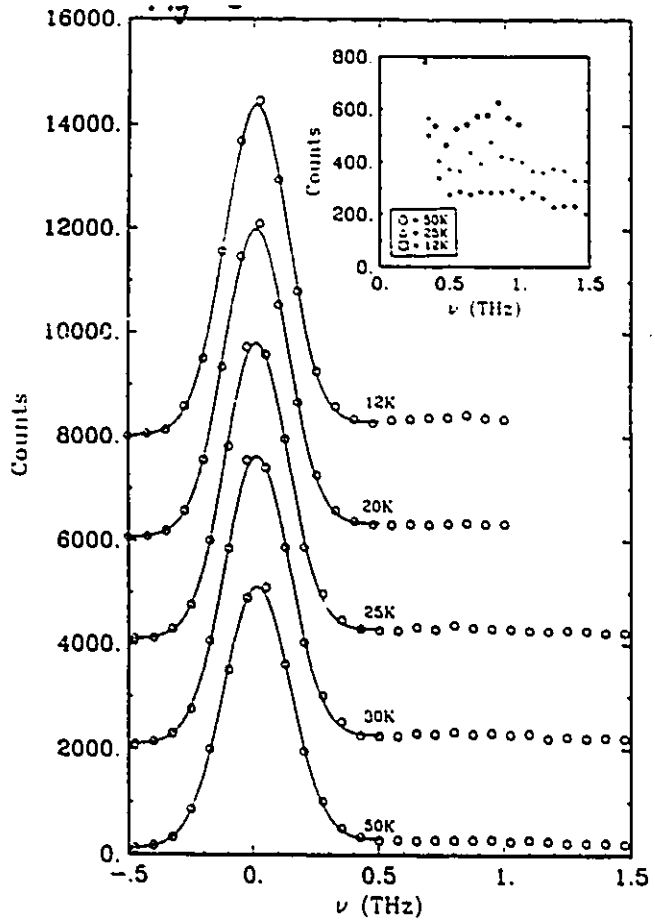

Fig. 3.22 Observed (°) and calculated (-) energy scans for $Tb_2Mo_2O_7$ at Q = 1.05 $\mathring{A}^{-1}$. The inset shows the development of a weak inelastic peak at ν = .85 THz below 50K[Ga90][Gr90a].

The scans are dominated by an almost resolution limited elastic peak. However evidence for a very weak inelastic peak at ν = .85 THz is seen to develop at low temperature (inset Fig. 3.22). The elastic peak was modeled with the following somewhat phenomenological cross-section satisfying detailed balance:

$$\frac{d\sigma}{d\nu} = \frac{\frac{\hbar\nu}{kT}}{1 - \exp\left(-\frac{\hbar\nu}{kT}\right)} \times \left\{ A(T)\exp\left(-4\mathrm{Ln}2\frac{(\nu-\nu_o)^2}{H(T)^2} \right) + \nu\, B(T) + C(T) \right\} \qquad (3.14)$$

where

A(T) is the peak intensity

B(T) and C(T) are sloping background parameters

H(T) is the full width at half maximum

and ν_o is the peak position.

A non zero ν_o was important for a good fit but $\nu_o \ll H(T)$ for all temperatures. Strictly speaking this cross section should really be a Lorentzian convoluted with the Gaussian resolution function but since over 90% of the halfwidth is from the experimental resolution the Lorentzian part of the scattering function was ignored.

The temperature dependence of the peak intensity and background constant are shown in Fig. 3.23a. The half-width and background slope are plotted in Fig. 3.23b where abrupt changes are seen to occur at the spin-freezing temperature, 25K.

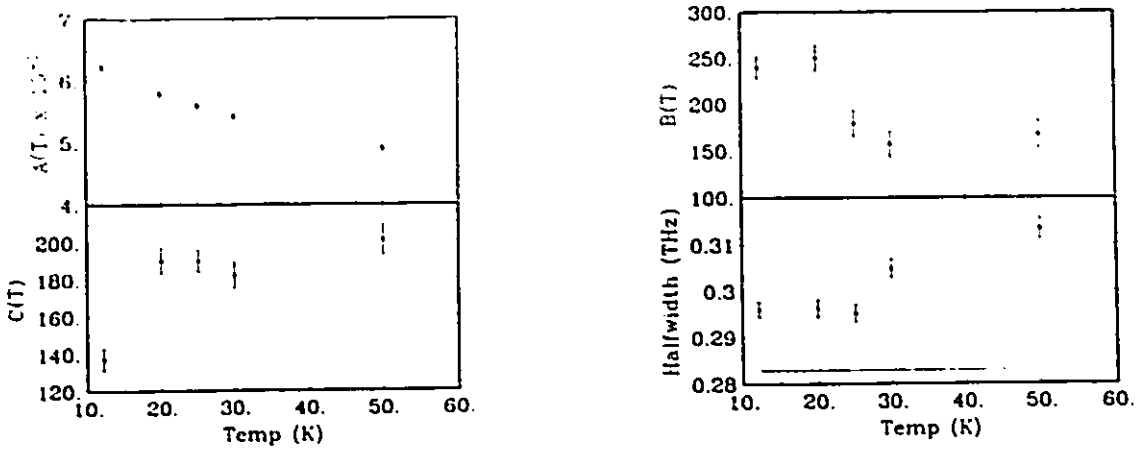

(a) (b)

Fig. 3.23 (a) Temperature dependence of the peak intensity (top) and the background constant (bottom). (b) Temperature dependence of the back ground slope (top) and the full width at half maximum (bottom) for the $Tb_2Mo_2O_7$ inelastic scans. The resolution halfwidth is indicated by the solid line.

The sudden increase in halfwidth at 25K can be interpreted as a shortening of the time scale over which the spins are moving, in other words an unfreezing of the spins as the temperature increases.

As in the case of $Y_2Mn_2O_7$ and $Y_2Mo_2O_7$ we have a significant amount of evidence for spin-glass-like behavior with T_f = 25K. 1) Weak cusp in χ at T_f 2) Strong sample history dependence in χ, 3) Onset of strong local spin-spin correlations below T_f and 4) direct evidence for some degree of spin freezing below T_f.

3.3.2 $Nd_2Mo_2O_7$:

The low temperature SANS data[Ba89][Gr90a] for $Nd_2Mo_2O_7$ with the 200K data subtracted are shown in Fig. 3.24.

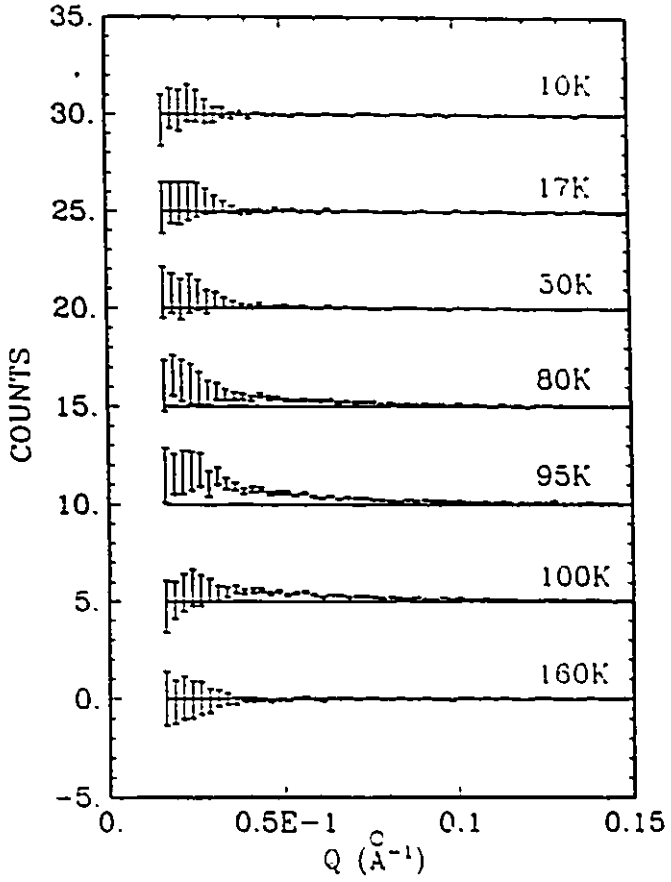

Fig. 3.24 SANS data for $Nd_2Mo_2O_7$ with the 200K data subtracted[Ba89][Gr90a].

Magnetic scattering at low Q can be seen at 100, 95, and 80K. This can be understood in terms of critical scattering from the [000] reflection. Fig. 3.25 shows the Q integrated scattering from .04 $\mathring{A}^{-1} \leq Q \leq .15\ \mathring{A}^{-1}$.

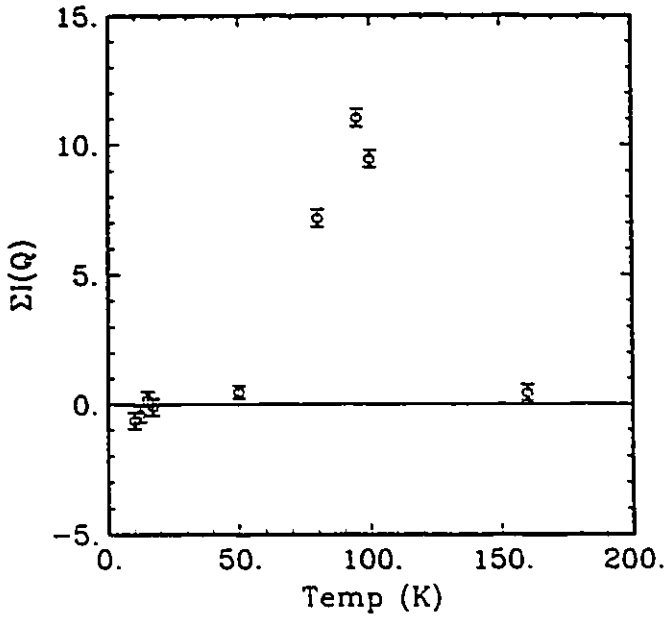

Fig. 3.25 Q integrated (.04 $\mathring{A}^{-1} \leq Q \leq .15\ \mathring{A}^{-1}$) magnetic SANS for $Nd_2Mo_2O_7$

The maximum at 95K is in accord with the T_c observed in the magnetization data[Sa 86]. The lack of scattering at 50K should not be interpreted as a lack of scattering at (000) (and thus lack of net magnetization) but merely reflects the fact that the system is long range ordered with virtually no critical scattering.

Chapter 4

Mean Field Calculations

4.1 Introduction

In chapter 1 the mean field theory was introduced in order to derive the Curie Weiss law for magnetic susceptibility. A much more general approach is applied here that will enable one to predict the stability of complicated antiferromagnetic spin structures. The calculation will be carried out in a more elegant manner through use of the density matrix concept. The density matrix contains information about the relative probabilities of various microscopic states as a function of any external parameters such as temperature and applied magnetic field. The density matrix plays an analogous role to the square of the wave function in quantum theory. For a macroscopic system the density matrix is an intractable object, however I will assume the density matrix can be approximated as a product of single spin density matrices this is the mean field approximation.

The calculation will also be simplified greatly by choosing a symmetry adapted basis set to describe the microscopic states of the system. For crystal lattices the most fundamental symmetry is translational, and the corresponding symmetry adapted basis set consists of Fourier modes labeled by wavevectors $\vec{k}$. Because the translational invariance is discrete the wavevectors will be bounded. Thus the minimum possible translation in the x direction is the unit cell edge a and k_x will vary from $\frac{\pi}{a} \leq k_x \leq \frac{\pi}{a}$. The allowed volume of $\vec{k}$ space is known as the first Brillouin zone (the first zone, for short). The zone is equivalent to a unit cell of reciprocal lattice discussed in section 2.1.2.

4.2 Mean Field Theory Formalism:

We consider a system with the Hamiltonian:

$$\mathcal{H} = -\frac{1}{2}\sum_{ij} J_{ij}\,\vec{S}_i\cdot\vec{S}_j - \vec{H}\cdot\sum_i \vec{S}_i \tag{4.1}$$

where the J_{ij} are isotropic exchange interactions ($J > 0$ corresponds to ferromagnetic coupling), $\vec{H}$ is a uniform external field and $\vec{S}_i$ is an n component unit spin at lattice site i. The stability of the system is governed by the free energy which has the form

$$F = \mathrm{Tr}(\rho\mathcal{H}) + T\,\mathrm{Tr}(\rho\ln\rho)\,. \tag{4.2}$$

Here ρ is the full density matrix of the system which, within the mean field approximation, is approximated by a product of single spin density matrices.

$$\rho(\{\vec{S}\}) = \prod_i \rho_i(\vec{S}_i)\,. \tag{4.3}$$

Following the procedure of Harris *et al.*[Ha84], I substitute (4.3) into (4.2) and minimize with respect to the ρ_i, subject to the constraints (which keep the internal energy fixed)

$$\mathrm{Tr}(\rho_i) = 1 \tag{4.4a}$$

$$\mathrm{Tr}(\rho_i\vec{S}_i) = \vec{B}_i\,, \tag{4.4b}$$

obtaining

$$\frac{\partial}{\partial \rho_i} \mathrm{Tr}\left(\rho_i \ln \rho_i - \rho_i(\lambda_i + \vec{A}_i \cdot \vec{S}_i)\right) = 0$$

or

$$\rho_i = C_i^{-1} \exp(\vec{A}_i \cdot \vec{S}_i)\,. \tag{4.5}$$

where λ_i and $\vec{A}_i$ are Lagrange multipliers for the constraints (4.4a) and (4.4b) respectively, and C_i is determined by the normalization condition (4.4a). For n component classical spins the trace has the form of an integral over the surface of an n dimensional hypersphere, thus

$$C_i(A_i) = \int d\Omega \exp(\vec{A}_i \cdot \vec{S}_i)$$

$$= \frac{(2\pi)^{\nu+1} \; I_\nu(A_i)}{A_i^\nu}, \qquad \nu \geq 0 \tag{4.6}$$

where $I_\nu(A_i)$ is a modified Bessel function, $A_i = |\vec{A}_i|$ and $\nu = n/2\text{-}1$. It is also useful to obtain an expression for the order parameters $\vec{B}_i$:

$$\mathrm{Tr}(\rho_i \vec{S}_i) = C_i^{-1} \int d\Omega \, \vec{S}_i \exp(\vec{A}_i \cdot \vec{S}_i)$$

$$= \frac{\vec{\nabla}_{\vec{A}} \; C_i(A_i)}{C_i(A_i)}$$

$$= \hat{A}_i \frac{\dfrac{\partial C_i(A_i)}{\partial A_i}}{C_i(A_i)}$$

$$\vec{B}_i = \hat{A}_i \frac{I_{\nu+1}(A_i)}{I_\nu(A_i)} \tag{4.7a}$$

or
$$B_i = \frac{I_{\nu+1}(A_i)}{I_\nu(A_i)}. \tag{4.7b}$$

The $\vec{A}_i$'s can be interpreted as local effective fields acting on the spins and are collinear with the order parameters $\vec{B}_i$. Substituting expressions (4.4), (4.5) and (4.7) into (4.2), one obtains an expression for the free energy of the system in terms of the order parameters, $\vec{B}_i$.

$$F(T,\vec{H}) = -\frac{1}{2}\sum_{ij} J_{ij}\,\vec{B}_i\cdot\vec{B}_j - \vec{H}\cdot\sum_i \vec{B}_i + T\sum_i \left(B_i \Lambda(B_i) - \ln\left[C|\Lambda(B_i)| \right] \right) \tag{4.8}$$

$$\Lambda(B_i) = A_i \tag{4.9}$$

The function $\Lambda(B_i)$ is the inverse of (4.7b). The stability conditions for the system can be obtained by minimizing $F(T,\vec{H})$ with respect to the $\vec{B}_i$'s or the $\vec{A}_i$'s. For simplicity I choose the former option, yielding the mean field equations for this problem.

$$\vec{\nabla}_{\vec{B}_i} F(T,\vec{H}) = -\vec{M}_i\cdot\vec{B}_i + T\,\vec{A}_i = 0 \tag{4.10}$$

$$\vec{M}_i = \sum_j J_{ij}\,\vec{B}_j + \vec{H} \tag{4.11}$$

4.3 The Landau Expansion:

Because the relationship between B_i and A_i is nonlinear the mean field equations (4.10) cannot be solved analytically. Above T_c the B_i are zero and just below T_c one might expect that the B_i will be very small and thus make a good expansion parameter. Small B_i expansions of the entropy term in (4.8) and relations (4.7) and (4.9) will be useful for a Landau expansion.

$$B(A) = \frac{A}{n} - \frac{A^3}{n^2(n+2)} + 2\frac{A^5}{n^3(n+2)(n+4)} - \frac{A^7(5n+12)}{n^5(n+2)^2(n+4)(n+6)} + \ldots \tag{4.12}$$

$$A(B) = nB + \frac{n^2B^3}{n+2} + \frac{n^3(n+8)B^5}{(n+2)^2(n+4)} + \frac{n^4(n^2+14n+120)B^7}{(n+2)^3(n+4)(n+6)} + \ldots \tag{4.13}$$

$$-S_i = \ln\left(\frac{\Gamma\left(\frac{n}{2}\right)}{2\sqrt{\pi}^n}\right) + \frac{nB_i^2}{2} + \frac{n^2B_i^4}{4(n+2)} + \frac{n^3(n+8)B_i^6}{6(n+2)^2(n+4)} + \ldots \tag{4.14}$$

In order to take advantage of the translational symmetry of the lattice, I also expand the order parameters B_i in terms of Fourier components. When considering non-Bravias lattices, it is convenient to label the spins in terms of unit cell coordinates and a sublattice index within the unit cell.

$$\vec{B}_i^a = \sum_{\vec{q}} \vec{B}_{\vec{q}}^a \exp(i\vec{q}\cdot\vec{R}_i) \tag{4.15}$$

$$J^{ab}_{\vec{R}_{ij}} = \frac{1}{N}\sum_{\vec{q}} J^{ab}_{\vec{q}} \exp[-i\vec{q}\cdot\vec{R}_{ij}] \tag{4.16}$$

Here i and j refer to unit cells and a and b refer to sublattices. To obtain the Landau theory I substitute (4.14), (4.15) and (4.16) into (4.8). Keeping terms up to fourth order in the order parameters, the free energy per unit cell is

$$\begin{aligned} F(T,\vec{H})/N = f(T,\vec{H}) &= p\,T \ln\left(\frac{\Gamma\left(\frac{n}{2}\right)}{2\sqrt{\pi^n}}\right) - \sum_a \vec{H}\cdot\vec{B}^a_0 \\ &+ \frac{1}{2}\sum_{\vec{q}}\sum_{ab} \vec{B}^a_{\vec{q}}\cdot\vec{B}^b_{-\vec{q}}[nT\delta^{ab} - J^{ab}_{\vec{q}}] \\ &+ \frac{Tn^2}{4(n+2)}\sum_a \sum_{\{\vec{q}\}}{}' (\vec{B}^a_{\vec{q}_1}\cdot\vec{B}^a_{\vec{q}_2})(\vec{B}^a_{\vec{q}_3}\cdot\vec{B}^a_{\vec{q}_4}) \end{aligned} \tag{4.17}$$

where $$\sum_{\{\vec{q}\}}{}' = \sum_{\vec{q}_1\vec{q}_2\vec{q}_3\vec{q}_4} \delta(\vec{q}_1+\vec{q}_2+\vec{q}_3+\vec{q}_4)$$

for a system with N unit cells and p spins per unit cell, and δ^{ab} is a Kronecker delta. Diagonalizing the second order term requires transforming to normal modes of the system

$$\vec{B}^a_{\vec{q}} = \sum_i U^{ai}_{\vec{q}}\vec{\phi}^i_{\vec{q}} \tag{4.18}$$

where $U_{\vec{q}}$ is a unitary matrix that diagonalizes $J_{\vec{q}}$ with eigenvalues $\lambda_{\vec{q}}$.

$$\sum_b J^{ab}_{\vec{q}}\, U^{bi}_{\vec{q}} = \lambda^i_{\vec{q}}\, U^{ai}_{\vec{q}} \tag{4.19}$$

The convention that indices (*ab*) label sublattices and indices (*ijkl*) label the normal modes will be used. Thus $U_{\vec{q}}^{ai}$ is the *a*'th component of the *i*'th eigenvector of $J_{\vec{q}}^{ab}$. In general, diagonalizing the second order term has the effect of complicating the form of the fourth order term in the expansion.

$$\begin{aligned} f(T,\vec{H}) &= p\,T \ln\left(\frac{\Gamma\left(\frac{n}{2}\right)}{2\sqrt{\pi}^{n}}\right) - \sum_{ai} U_0^{ai}\,\vec{H}\cdot\vec{\phi}_0^{i} \\ &\quad + \frac{1}{2}\sum_{\vec{q}}\sum_{i}\vec{\phi}_{\vec{q}}^{\,i}\cdot\vec{\phi}_{-\vec{q}}^{\,i}\,[nT-\lambda_{\vec{q}}^{i}] \\ &\quad + \frac{Tn^2}{4(n+2)}\sum_{\{\vec{q}\}}{}'\sum_{ijkl}(\vec{\phi}_{\vec{q}_1}^{\,i}\cdot\vec{\phi}_{\vec{q}_2}^{\,j})(\vec{\phi}_{\vec{q}_3}^{\,k}\cdot\vec{\phi}_{\vec{q}_4}^{\,l})\sum_{a} U_{\vec{q}_1}^{ai}U_{\vec{q}_2}^{aj}U_{\vec{q}_3}^{ak}U_{\vec{q}_4}^{al} \end{aligned} \tag{4.20}$$

Obviously the characteristic physics of the system is contained in the $\lambda_{\vec{q}}^{i}$ and the $U_{\vec{q}}^{ai}$. The first ordered state of the system will occur at a temperature

$$T_c = \frac{1}{n}\max\{\lambda_{\vec{q}}^{i}\} \tag{4.21}$$

where max{ } indicates a global maximum for all *i* and $\vec{q}$.

4.4 Application to The Pyrochlore Lattice:

4.4.1 The Primitive Unit Cell:

In order to simplify the calculations somewhat, the system will be described in a non-standard rhombohedral setting with a unit cell having one quarter the volume of the cubic cell. The lattice vectors of the two systems are related by

$$\begin{bmatrix} \vec{a} \\ \vec{b} \\ \vec{c} \end{bmatrix}^{\text{Rhom}} = \begin{bmatrix} 0 & \frac{1}{2} & \frac{1}{2} \\ \frac{1}{2} & 0 & \frac{1}{2} \\ \frac{1}{2} & \frac{1}{2} & 0 \end{bmatrix} \begin{bmatrix} \vec{a} \\ \vec{b} \\ \vec{c} \end{bmatrix}^{\text{Cubic}} . \qquad (4.22)$$

The advantage of the rhombohedral basis is that there are only 8 metal atoms per unit cell (4 of the type 16c and 4 of the type 16d), as opposed to 32 per cell in the cubic system. The corresponding space group is R$\bar{3}$m, which is a subgroup of Fd$\bar{3}$m. Thus the rhombohedral representation has the disadvantage that some of the inherent symmetry is hidden. Table 4.1 shows a list of metal positions for both systems along with their nearest neighbors (NN's) listed by atom number (#). The factor of 2 in front of each list of NN's indicates that there are two of each type of NN, which are related by spatial inversion.

Table 4.1

Pyrochlore metal atom positions in rhombohedral and cubic basis

site	atom #	position rhom	position cubic	nearest neighbors
16c	1	(0,0,0)	(0,0,0)+F.C.[a]	2 × (2,3,4,6,7,8)[b]
16c	2	$(\frac{1}{2},0,0)$	$(0,\frac{1}{4},\frac{1}{4})$+F.C.	2 × (1,3,4,5,7,8)
16c	3	$(0,\frac{1}{2},0)$	$(\frac{1}{4},0,\frac{1}{4})$+F.C.	2 × (1,2,4,5,6,8)
16c	4	$(0,0,\frac{1}{2})$	$(\frac{1}{4},\frac{1}{4},0)$+F.C.	2 × (1,2,3,5,6,7)
16d	5	$(\frac{1}{2},\frac{1}{2},\frac{1}{2})$	$(\frac{1}{2},\frac{1}{2},\frac{1}{2})$+F.C.	2 × (2,3,4,6,7,8)
16d	6	$(0,\frac{1}{2},\frac{1}{2})$	$(\frac{1}{2},\frac{1}{4},\frac{1}{4})$+F.C.	2 × (1,3,4,5,7,8)
16d	7	$(\frac{1}{2},0,\frac{1}{2})$	$(\frac{1}{4},\frac{1}{2},\frac{1}{4})$+F.C.	2 × (1,2,4,5,6,8)
16d	8	$(\frac{1}{2},\frac{1}{2},0)$	$(\frac{1}{4},\frac{1}{4},\frac{1}{2})$+F.C.	2 × (1,2,3,5,6,7)

[a] F.C. stands for the Face Centering operation $(0,0,0;\ 0,\frac{1}{2},\frac{1}{2};\ \frac{1}{2},0,\frac{1}{2};\ \frac{1}{2},\frac{1}{2},0)$

[b] nearest neighbors are listed by atom #.

4.4.2 The General NN Coupling Matrix:

From the Fourier transform of (4.16) and the information in Table 4.1, one can calculate the matrix $J_{\vec{q}}^{ab}$ for the general pyrochlore problem with nearest neighbor interactions. I first define

$$\mathcal{J}_{intra} = 2\begin{bmatrix} 0 & \cos(q_x) & \cos(q_y) & \cos(q_z) \\ \cos(q_x) & 0 & \cos(q_x-q_y) & \cos(q_z-q_x) \\ \cos(q_y) & \cos(q_x-q_y) & 0 & \cos(q_y-q_z) \\ \cos(q_z) & \cos(q_z-q_x) & \cos(q_y-q_z) & 0 \end{bmatrix}$$

$$\mathcal{J}_{inter} = 2\begin{bmatrix} 0 & \cos(q_y-q_z) & \cos(q_z-q_x) & \cos(q_x-q_y) \\ \cos(q_y-q_z) & 0 & \cos(q_z) & \cos(q_y) \\ \cos(q_z-q_x) & \cos(q_z) & 0 & \cos(q_x) \\ \cos(q_x-q_y) & \cos(q_y) & \cos(q_x) & 0 \end{bmatrix}$$

which are respectively the intra-sublattice and the inter-sublattice coupling matrices for the 16c and the 16d sites. The full coupling matrix now has the form

$$J_{\vec{q}}^{ab} = \begin{bmatrix} J_1 \mathcal{J}_{intra} & J_{12} \mathcal{J}_{inter} \\ J_{12} \mathcal{J}_{inter} & J_2 \mathcal{J}_{intra} \end{bmatrix} \qquad (4.23)$$

where J_1 and J_2 are couplings for metal atoms within the 16c and 16d sublattices respectively, and J_{12} is the coupling between 16c and 16d.

In the next section systems will be considered in which only one of the metal atoms is magnetic. This is applicable to materials such as FeF_3[5], $Y_2Mo_2O_7$[7,9] and $Y_2Mn_2O_7$[8] where the yttrium atoms are diamagnetic.

4.4.3 One magnetic sublattice (one of A or B is magnetic):

For this model there are four magnetic atoms per unit cell and

$$J_{\vec{q}}^{ab} = J_1 \mathcal{J}_{intra} \tag{4.24}$$

which can be diagonalized explicitly. By defining

$$Q = \frac{1}{2}\Big(\cos(2q_x) + \cos(2q_y) + \cos(2q_z) + \cos(2q_x-2q_y) + \cos(2q_y-2q_z) + \cos(2q_z-2q_x) \Big) \tag{4.25}$$

We have

$$\lambda_{\vec{q}}^{1} = \lambda_{\vec{q}}^{2} = -2J_1$$

$$\lambda_{\vec{q}}^{3} = 2J_1 \left(1 - \sqrt{1+Q} \right)$$

$$\lambda_{\vec{q}}^{4} = 2J_1 \left(1 + \sqrt{1+Q} \right). \tag{4.26}$$

Note that λ^1 and λ^2 are completely independent of $\vec{q}$ and that these are the maximal eigenvalues for the system when $J_1 < 0$. Dispersion curves for the four modes are shown in Fig. 4.1, from which one can see that mode 3 is also degenerate with 1 and 2 at $\vec{q} = 0$.

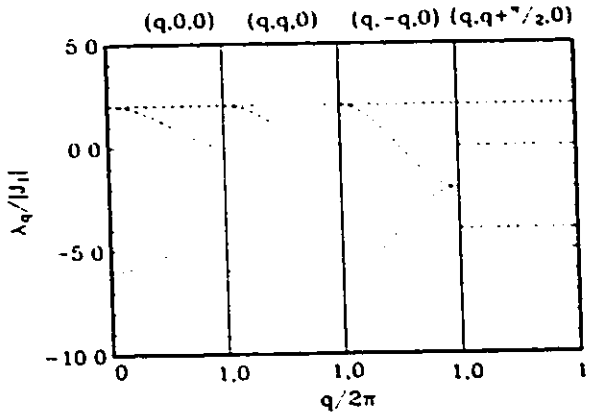

Fig. 4.1 Dispersion curves along certain symmetry directions, for one sublattice pyrochlore systems with only NN exchange interactions. The unstable or critical modes will have the largest eigenvalue λ_q which is measured in units of J_1 which is the NN coupling constant.

Bertaut was aware of this high degree of degeneracy but only along certain high symmetry directions in q̄-space[Be61]. Thus mean field theory predicts a special temperature, $T_c = \frac{2}{3}|J_1|$ below which the system preferentially samples modes 1 and 2, i.e. a phase space with half the dimensionality of the high temperature phase space. The heat capacity for this system should show an entropy change of kln2 over a rather broad temperature range. Whether or not this entropy change will appear in the form of a Schottky anomaly is not yet clear.

In light of this information one can see that any sort of long range order (within the MF approximation) in this system can only arise from the presence of further neighbor interactions, such as second neighbor exchange, dipole forces or perhaps an external field. It is therefore interesting to examine the effects of further neighbor interactions by considering the first four coordination shells. Table 4.2 shows the type of neighbors and their distances for atom 1. The neighbors for atoms 2, 3 and 4 are easily obtained by permuting atom labels.

Table 4.2

Neighbors and exchange constants for one-sublattice pyrochlores

Shell #	Neighbors	Distance/a_{Rh}	Coupling constant
1	2(2,3,4)	$1/2^a$	J_1
2	4(2,3,4)	$\sqrt{3}/2$	J_2
3	12(1)	1	J_3
4	4(2,3,4)	$\sqrt{5}/2$	J_4

^{a}Distances in units of rhombohedral cell edge.

The $J_{\vec{q}}^{ab}$ matrix now becomes significantly more complicated and the matrix elements are written out explicitly in Appendix B. In order to get a qualitative idea of the effects of these weak further neighbor interactions, it is useful to look at how the eigenvalues for the four modes behave for the six exchange models listed in Table 4.3.

Table 4.3

Six exchange models considered

model	J_1	J_2	J_3	J_4	Figure
I_a	-1	> 0	0	0	4.2a
I_b	-1	< 0	0	0	4.2b
II_a	-1	0	> 0	0	4.3a
II_b	-1	0	< 0	0	4.3b
III_a	-1	0	0	> 0	4.4a
III_b	-1	0	0	< 0	4.4b

Dispersion curves for these models are shown in Figs. 4.2, 4.3 and 4.4.

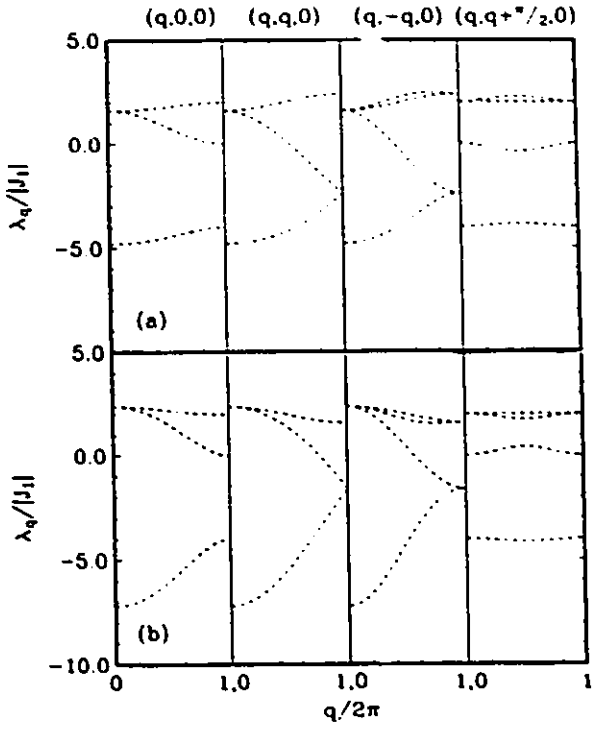

Fig. 4.2 As in Fig. 2 with the addition of a small 2nd neighbor interaction. $J_2 > 0$ in a and $J_2 < 0$ in b.

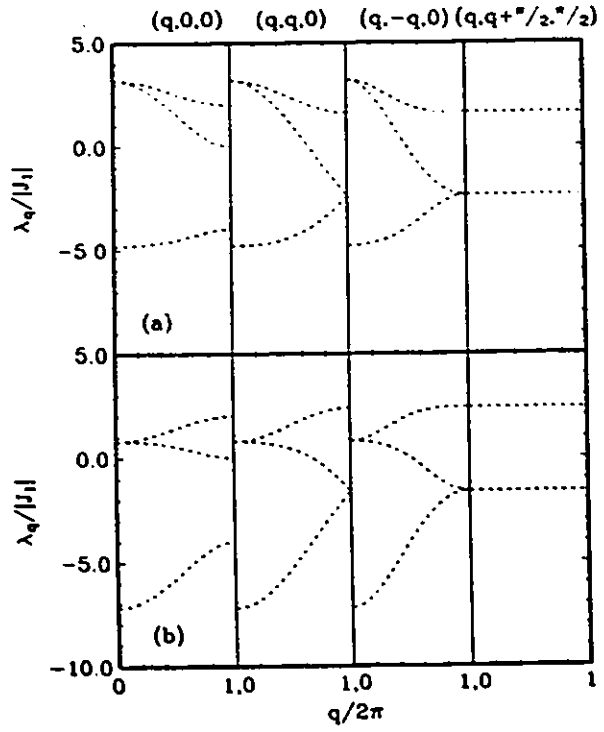

Fig. 4.3 As in Fig. 2 with the addition of a small 3rd neighbor interaction. $J_3 > 0$ *in a and* $J_3 < 0$ *in b.*

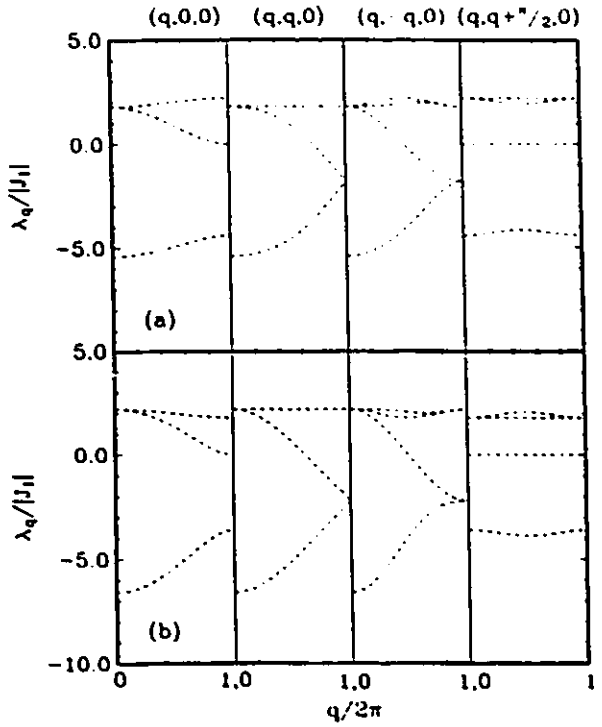

Fig. 4.4 As in Fig. 2 with the addition of a small 4th neighbor interaction. $J_4 > 0$ *in a and* $J_4 < 0$ *in b.*

Model I_a will order in an incommensurate phase with wave vector $(q_o,-q_o,0)$ or $(q_o,q_o,2q_o)$ where q_o is an irrational function of J_1/J_2. By permuting the indices one can see that the two points above are each six fold degenerate, making a total of 12 independent ordering wave vectors in the first zone. Models I_b and II_a order with wave vector (0,0,0), where three out of the four modes are degenerate. This corresponds to the type of ordering observed in FeF_3, as determined by neutron diffraction, which will be discussed further in the next section. The last three models

have critical modes which are dispersionless along certain symmetry directions. Thus no long range order is expected for these models (within the MF approximation).

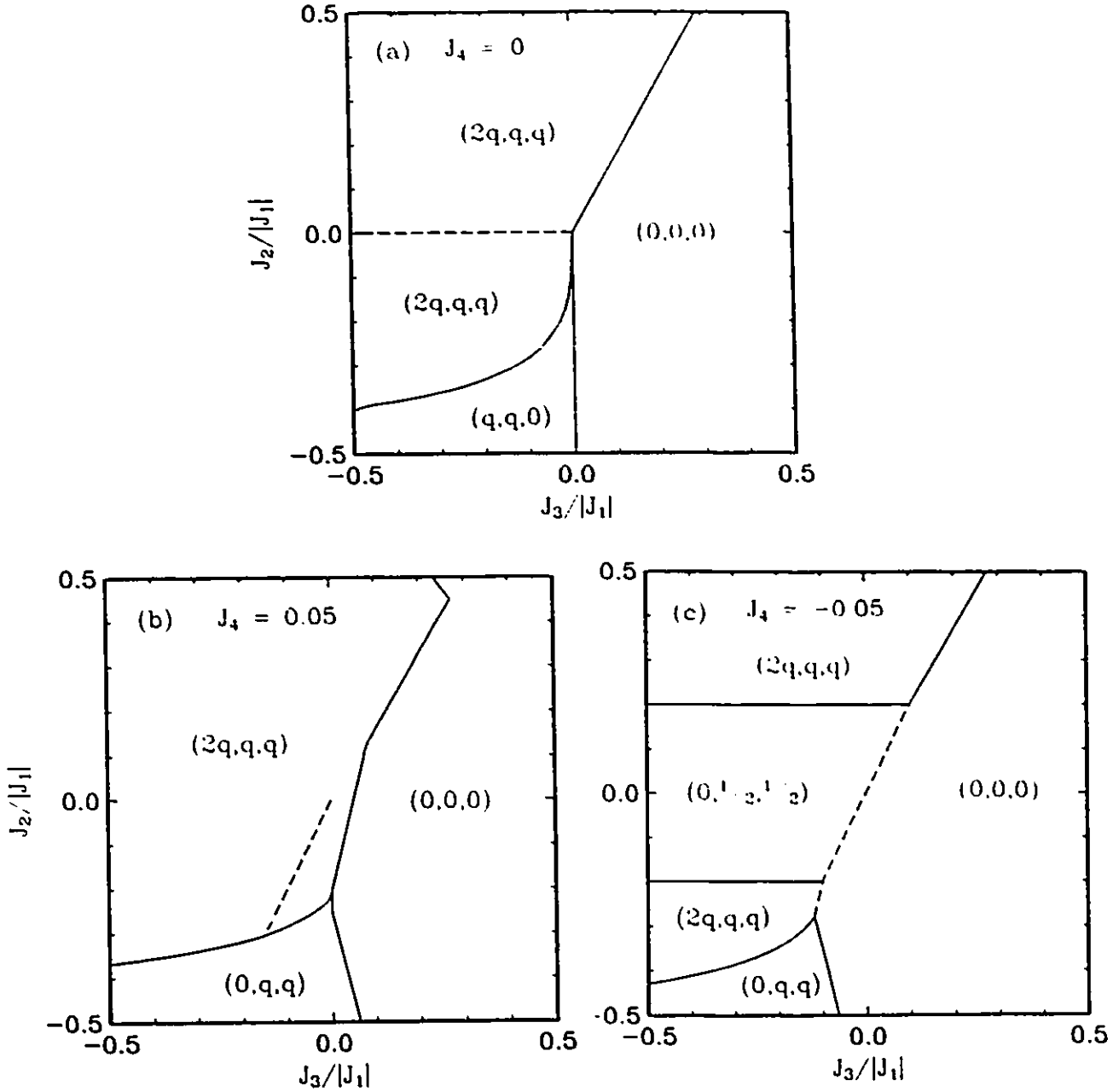

Fig. 4.5 Ordering wavevectors in the coupling parameter space J_3 and J_2 with J_1 = -1 and J_4 = 0 in a, J_4 = 0.05 in b and J_4 = -0.05 in c. Along the dashed line the system is continuously degenerate and critical along the $(q,q+\frac{\pi}{2},\frac{\pi}{2})$ direction.

Figures 4.5 (a,b, and c) show the ordering wave vectors in the coupling constant space J_2 and J_3 for J_1 = -1 and three different choices of J_4. In the (2q,q,q) and (0,q,q) regions the critical modes are, in general, incommensurate with finite degeneracy. Dotted lines indicate regions where the system is continuously unstable along certain directions in $\vec{q}$ space with infinite degeneracy and therefore no long range order. Note that for consistency all $\vec{q}$ vectors discussed in this work are in the rhombohedral basis. Table 4.4 lists all ordering wave vectors in both systems, as well as the associated multiplicities required by cubic symmetry.

Table 4.4

Relevant $\vec{q}$ vectors in the rhombohedral and cubic bases

rhombohedral	Cubic	Multiplicity
(0,0,0)	(0,0,0)	1
(0,q,q)	(2q,0,0)	6
(2q,q,q)	(0,2q,2q)	6
(0,q,-q)	(0,-2q,2q)	6
(0,1/2,1/2)	(1,0,0)	6

Unstable modes characterized by $\vec{q}$ = (2q,q,q) are actually 12 fold degenerate corresponding to the star of (q,q,0) directions in the cubic basis, *i.e.*, directions (2q,q,q) and (0,q,-q) in the rhombohedral basis are equivalent by symmetry.

4.4.4 Landau Theory for $\vec{q}$ = 0 (one magnetic sublattice):

The normal modes of J_0^{ab} are listed in Table 4.5 and the critical temperature at $\vec{H}$ = 0 is

$$T_c = -\frac{1}{n} 2(J_1 + 2J_2 - 6J_3 + 2J_4) \qquad (4.27)$$

Table 4.5

Eigenvectors and eigenvalues of the coupling matrix J_0^{ab} for one-sublattice pyrochlores

eigenvectors	eigenvalues
$\vec{\Psi}_1 = \frac{1}{2}(1, 1,-1,-1)$	$-2(J_1 + 2J_2 - 6J_3 + 2J_4)$
$\vec{\Psi}_2 = \frac{1}{2}(1,-1, 1,-1)$	$-2(J_1 + 2J_2 - 6J_3 + 2J_4)$
$\vec{\Psi}_3 = \frac{1}{2}(1,-1,-1, 1)$	$-2(J_1 + 2J_2 - 6J_3 + 2J_4)$
$\vec{\Psi}_4 = \frac{1}{2}(1, 1, 1, 1)$	$6(J_1 + 2J_2 + 2J_3 + 2J_4)$

It is important to remember that $J_1 < 0$, and one expects that $|J_1| \gg |J_2|$ and $|J_1| \gg |J_3|$. Substituting the information in Table 4.5 into expression (4.20) and considering only the $\vec{q} = 0$ terms in the summations, one obtains the Landau free energy for this model.

$$f = \mu_o - 2\vec{H}\cdot\vec{\Phi}_4 + \frac{1}{2} r_o m^2 + \frac{1}{2} r_1 \Phi_4^2$$

$$+ \frac{1}{4} u \left[(m^2+\Phi_4^2)^2 + 4(a^2+b^2+c^2)\right]$$

$$+ \frac{1}{6} v \left[(m^2+\Phi_4^2)^3 + 12(m^2+\Phi_4^2)(a^2+b^2+c^2) + 48\,abc\right] + \ldots \qquad (4.28)$$

where

$$\mu_o = 4\,T \ln\left(\frac{\Gamma\left(\frac{n}{2}\right)}{2\sqrt{\pi^n}}\right) \qquad (4.29)$$

$$r_o = n(T-T_c) \tag{4.30a}$$

$$r_1 = n(T+3T_c)-48J_3 \tag{4.30b}$$

$$u = \frac{Tn^2}{4(n+2)} \tag{4.31a}$$

$$v = \frac{Tn^3(n+8)}{16n(n+2)^2(n+4)} \tag{4.31b}$$

$$m^2 = \phi_1^2 + \phi_2^2 + \phi_3^2 \tag{4.32}$$

$$a = \vec{\Phi}_1 \cdot \vec{\Phi}_2 + \vec{\Phi}_3 \cdot \vec{\Phi}_4 \tag{4.33a}$$

$$b = \vec{\Phi}_1 \cdot \vec{\Phi}_3 + \vec{\Phi}_2 \cdot \vec{\Phi}_4 \tag{4.33b}$$

$$c = \vec{\Phi}_1 \cdot \vec{\Phi}_4 + \vec{\Phi}_2 \cdot \vec{\Phi}_3 . \tag{4.33c}$$

One can see right away that the direction of $\vec{\Phi}_4$ is determined by the external field and minimizing with respect to a, b and c gives the conditions

$$a = b = c = 0. \tag{4.34}$$

Equations (4.34) and (4.32) impose 4 constraints on $\vec{\Phi}_1$, $\vec{\Phi}_2$ and $\vec{\Phi}_3$ leaving $3n$-4 degrees of freedom. Thus there is no restriction on the relative magnitudes of $\vec{\Phi}_1$, $\vec{\Phi}_2$ and $\vec{\Phi}_3$ which for $n = 3$ corresponds to an internal 2 dimensional degeneracy of the ordered phase, and also no restriction that one of the modes must be parallel to $\vec{\Phi}_4$ for $n \geq 3$. Also note that only r_o is critical and not r_1. The sixth order term has been included in order to check for tri-critical behavior. Setting $\vec{\Phi}_4$ parallel to $\vec{H}$ and imposing condition (4.34), the Landau free energy is expressed in terms of the two variables m and Φ_4, where m should be interpreted as the order parameter for the antiferromagnetism and Φ_4 the higher energy non-critical ferromagnetic mode that

couples to the external field.

$$f = \mu_o - 2H\Phi_4 + \frac{1}{2}(r_o m^2 + r_1\Phi_4^2) + \frac{1}{4}u(m^2+\Phi_4^2)^2 + \frac{1}{6}v(m^2+\Phi_4^2)^3 + \ldots \quad (4.35)$$

with equilibrium conditions

$$\left(r_o + u(m^2+\Phi_4^2) + v(m^2+\Phi_4^2)^2\right)m = 0, \quad (4.36)$$

$$\left(r_1 + u(m^2+\Phi_4^2) + v(m^2+\Phi_4^2)^2\right)\Phi_4 = 2H. \quad (4.37)$$

In the paramagnetic region where $m = 0$ one has

$$\Phi_4 = \frac{2H}{r_1}\left(1 - \frac{u}{r_1}\left(\frac{2H}{r_1}\right)^2 - \frac{v}{r_1}\left(\frac{2H}{r_1}\right)^4 + \ldots\right), \quad (4.38)$$

and from (4.36) and (4.37) in the ordered regime:

$$\Phi_4 = \frac{2H}{(r_1 - r_o)} = \frac{H}{2(nT_c - 12J_3)} = h, \quad (4.39)$$

which is independent of temperature and exact to all orders in $(m^2+\Phi_4^2)$ within the mean field approximation as explained in more detail in Appendix C. I have also defined h which is the reduced field for the system. When (4.39) is substituted into (4.35) the second and fourth order coefficients in m are respectively:

$$\frac{1}{2}\left(r_o + uh^2 + vh^4\right) \quad (4.40)$$

$$\frac{1}{4}\left(u + 2vh^2\right) \tag{4.41}$$

The fourth order coefficient is positive definite and therefore no tri-critical point exists within the mean field approximation. Setting (4.40) equal to zero determines a line of second order phase transitions in the (H,T) plane. Neglecting the v term one has

$$h = 2\sqrt{\frac{T_c - T}{T}\,\frac{n+2}{n}} \tag{4.42}$$

which presumably saturates at low temperature due to the higher order terms in the Landau expansion. At zero temperature

$$\sum_i B_i^2 = \sum_i \phi_i^2 = m^2 + \phi_4^2 = 4. \tag{4.43}$$

Substituting (4.39) into (4.43) and setting $m = 0$ defines the critical field at zero temperature:

$$h_c = 2 \tag{4.44a}$$

or

$$H_c = 4(nT_c - 12J_3) \tag{4.44b}$$

Fig. 4.6 shows the mean field phase diagram for $\vec{q} = 0$ systems.

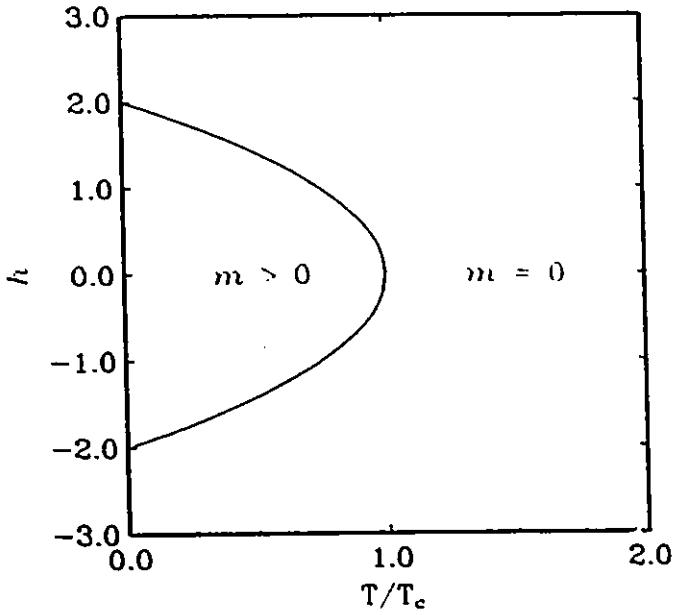

Fig. 4.6 (H,T) phase diagram for the $\vec{q} = 0$ systems with $J_1 < 0$. h is defined in (4.16), T_c in (4.4) and m is the order parameter for modes 1,2 and 3. The solid line indicates a line of second order phase transitions.

Ferey *et. al.*[5] have proposed the following spin structure (Fig. 2.6) for FeF_3 based on powder diffraction

$$\begin{aligned} &\vec{S}_1 \text{ along } (1,1,1) \\ &\vec{S}_2 \text{ along } (1,-1,-1) \\ &\vec{S}_3 \text{ along } (-1,1,-1) \\ &\vec{S}_4 \text{ along } (-1,-1,1) \end{aligned} \tag{4.45}$$

The magnetic (1,1,1) reflection in FeF_3 was absent which means for a powder that the structure factors $\vec{F}_{111} = \vec{F}_{1\text{-}1\text{-}1} = \vec{F}_{\text{-}11\text{-}1} = \vec{F}_{\text{-}1\text{-}11} = 0$. One can solve this system of equations explicitly and show that indeed (4.45) is the only possible spin structure. In terms of the normal modes one has

$$\vec{\Phi}_1 = \frac{1}{\sqrt{3}}(m,0,0)$$
$$\vec{\Phi}_2 = \frac{1}{\sqrt{3}}(0,m,0)$$
$$\vec{\Phi}_3 = \frac{1}{\sqrt{3}}(0,0,m) \qquad (4.46)$$

which is consistent with but much more restrictive than (4.32), (4.33) and (4.34). There must therefore be some anisotropy in FeF_3 that breaks the 5 dimensional degeneracy of the ordered state predicted by mean field theory. This uniaxial anisotropy is consistent with local site symmetry of the Fe^{3+} ions, as dictated by the space group symmetry. In principle one should be able to determine from powder neutron diffraction the magnitudes and directions of $\vec{\Phi}_1$, $\vec{\Phi}_2$ and $\vec{\Phi}_3$ for any $\vec{q} = 0$ system.

4.4.5 Two Magnetic Sublattices (both A and B are magnetic):

For this problem one is dealing with an 8×8 coupling matrix as defined in (4.23) and a three dimensional coupling parameter space spanned by J_1, J_2 and J_{12}. The effects of further neighbor interactions will not be considered here. In general the magnetic species on the two sublattices will have different moments which can be absorbed into the J's in such a way that all spins are still unit vectors. Figures 4.7a and 4.7b show maps in parameter space of J_2 and J_{12} for $J_1 = 0$ and $J_1 = -1$ respectively, which covers all cases of interest.

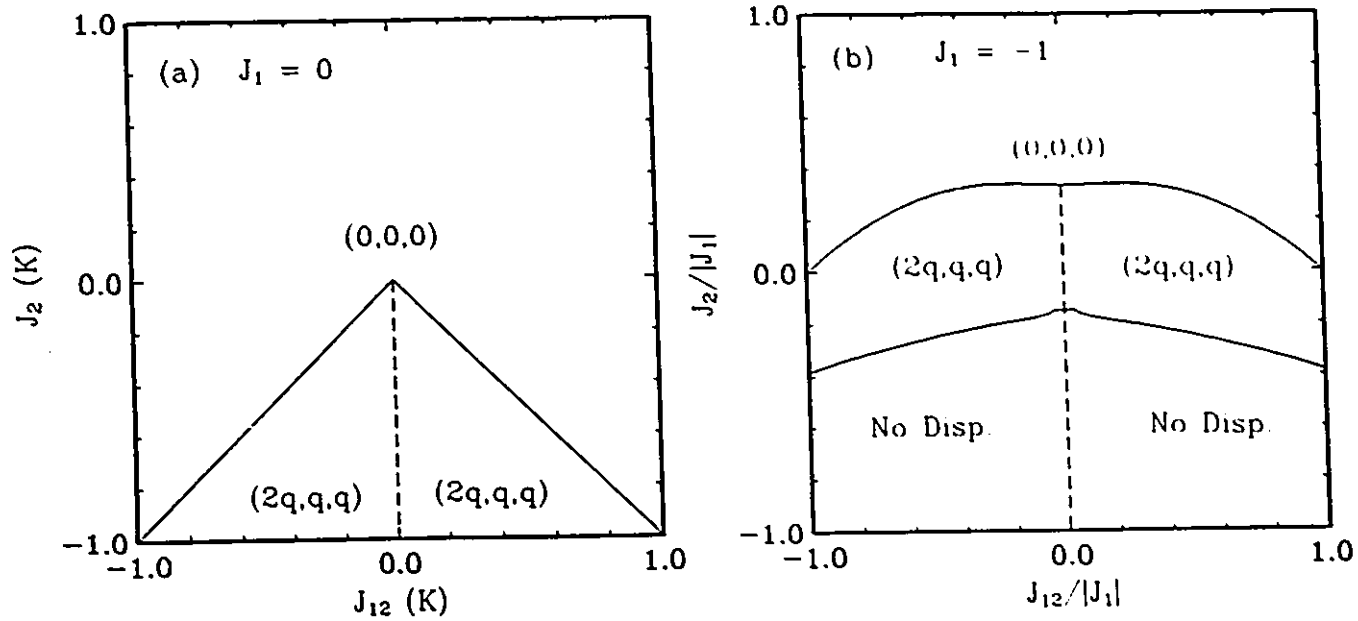

Fig. 4.7 Ordering wavevectors in the coupling parameter space J_2 and J_{12} with $J_1 = 0$ in a and $J_1 = -1$ in b for two sublattice pyrochlores with NN interactions. Along the dashed line the system is continuously degenerate and critical throughout the whole zone. "No Disp." indicates that the system is continuously degenerate along the (0,q,q) directions.

The phase diagram is seen to be invariant under changes in the sign of J_{12}. As before there are large regions where the $\vec{q} = 0$ mode becomes ordered below T_c, and also regions of (2q,q,q) incommensurate phases. The dotted lines along $J_{12} = 0$ in both diagrams indicate regions where the whole zone is degenerate. This stems from the fact that the two sublattices are decoupled and thus have the $\vec{q}$-independent eigenvalues shown in (4.26). Of particular interest is the large region in Fig. 4.7b where the system is degenerate along the (0,q,q) direction. Again one expects no long range order for such model systems.

4.4.6 Landau Theory for $\vec{q} = 0$ (Two Magnetic Sublattices):

Table 4.6

Eigenvectors and eigenvalues of the coupling matrix J_0^{ab} for two-sublattice pyrochlores

eigenvectors	eigenvalues
$\vec{\Psi}_1 = (\varepsilon, \varepsilon, \varepsilon, \varepsilon, \frac{1}{\varepsilon}, \frac{1}{\varepsilon}, \frac{1}{\varepsilon}, \frac{1}{\varepsilon})^a$	$3(\alpha+\beta)^a$
$\vec{\Psi}_2 = (\frac{1}{\varepsilon}, \frac{1}{\varepsilon}, \frac{1}{\varepsilon}, \frac{1}{\varepsilon}, -\varepsilon, -\varepsilon, -\varepsilon, -\varepsilon)$	$3(\alpha-\beta)$
$\vec{\Psi}_3 = (\varepsilon, \varepsilon, -\varepsilon, -\varepsilon, \frac{1}{\varepsilon}, \frac{1}{\varepsilon}, -\frac{1}{\varepsilon}, -\frac{1}{\varepsilon})$	$-(\alpha+\beta)$
$\vec{\Psi}_4 = (\varepsilon, -\varepsilon, \varepsilon, -\varepsilon, \frac{1}{\varepsilon}, -\frac{1}{\varepsilon}, \frac{1}{\varepsilon}, -\frac{1}{\varepsilon})$	$-(\alpha+\beta)$
$\vec{\Psi}_5 = (\varepsilon, -\varepsilon, -\varepsilon, \varepsilon, \frac{1}{\varepsilon}, -\frac{1}{\varepsilon}, -\frac{1}{\varepsilon}, \frac{1}{\varepsilon})$	$-(\alpha+\beta)$
$\vec{\Psi}_6 = (\frac{1}{\varepsilon}, \frac{1}{\varepsilon}, -\frac{1}{\varepsilon}, -\frac{1}{\varepsilon}, -\varepsilon, -\varepsilon, \varepsilon, \varepsilon)$	$-(\alpha-\beta)$
$\vec{\Psi}_7 = (\frac{1}{\varepsilon}, -\frac{1}{\varepsilon}, \frac{1}{\varepsilon}, -\frac{1}{\varepsilon}, -\varepsilon, \varepsilon, -\varepsilon, \varepsilon)$	$-(\alpha-\beta)$
$\vec{\Psi}_8 = (\frac{1}{\varepsilon}, -\frac{1}{\varepsilon}, -\frac{1}{\varepsilon}, \frac{1}{\varepsilon}, -\varepsilon, \varepsilon, \varepsilon, -\varepsilon)$	$-(\alpha-\beta)$

[a] α, β and ε are defined in the text.

Again I list the eigenvalues and eigenvectors of J_0^{ab} in Table 4.6 where

$$\alpha = \frac{J_1 + J_2}{2} \tag{4.47}$$

$$\beta = \frac{J_{12}}{|J_{12}|}\sqrt{\left(\frac{J_1 - J_2}{2}\right)^2 + J_{12}^2} \tag{4.48}$$

$$\varepsilon^2 = \frac{\beta}{J_{12}} + \sqrt{\left(\frac{\beta}{J_{12}}\right) - 1} \tag{4.49}$$

thus

$$\frac{\beta}{J_{12}} = \frac{1}{2}\left(\varepsilon^2 + \frac{1}{\varepsilon^2}\right) = \cosh\left(2\ln(\varepsilon)\right) . \tag{4.50}$$

The normalization factor for all eigenvectors is

$$\frac{1}{2}\sqrt{\frac{J_{12}}{\beta}} . \tag{4.51}$$

$\vec{\Psi}_1$ and $\vec{\Psi}_2$ can be interpreted as ferromagnetic and ferrimagnetic modes of the system respectively, where the intra-sublattice alignment is ferromagnetic. $\vec{\Psi}_3$, $\vec{\Psi}_4$ and $\vec{\Psi}_5$ correspond to degenerate modes where the A sublattice is aligned ferromagnetically with the B sublattice, with intra-sublattice coupling being antiferromagnetic. $\vec{\Psi}_6$, $\vec{\Psi}_7$ and $\vec{\Psi}_8$ have antiferromagnetic inter- and intra-sublattice alignment.

The fourth order term in the Landau free energy has the general form

$$\frac{u}{4}\frac{J_{12}^2}{\beta^2}\Bigg(\frac{1}{2}(M_1^2 + M_2^2)^2 + (\delta_o + SM_1^2)^2 + (\delta_o - SM_2^2)^2 + \sum_{i=1}^{3}\left((\delta_i + 2Sa_i)^2 + (\delta_i - 2Sb_i)^2 + 2\,(a_i + b_i)^2 \right) \Bigg) \tag{4.52}$$

$$M_1^2 = \phi_1^2 + \phi_3^2 + \phi_4^2 + \phi_5^2 = \phi_1^2 + m_1^2 \tag{4.53a}$$

$$M_2^2 = \phi_2^2 + \phi_6^2 + \phi_7^2 + \phi_8^2 = \phi_2^2 + m_2^2 \tag{4.53b}$$

$$m_1^2 = \phi_3^2 + \phi_4^2 + \phi_5^2 \tag{4.54c}$$

$$m_2^2 = \phi_6^2 + \phi_7^2 + \phi_8^2 \tag{4.54d}$$

$$S = \frac{1}{2}\left(\varepsilon^2 - \frac{1}{\varepsilon^2}\right) = \sinh[2\ln(\varepsilon)] \tag{4.55}$$

$$\delta_o = \vec{\Phi}_1\cdot\vec{\Phi}_2 + \vec{\Phi}_3\cdot\vec{\Phi}_6 + \vec{\Phi}_4\cdot\vec{\Phi}_7 + \vec{\Phi}_5\cdot\vec{\Phi}_8 \tag{4.56a}$$
$$\delta_1 = \vec{\Phi}_1\cdot\vec{\Phi}_6 + \vec{\Phi}_2\cdot\vec{\Phi}_3 + \vec{\Phi}_4\cdot\vec{\Phi}_8 + \vec{\Phi}_5\cdot\vec{\Phi}_7 \tag{4.56b}$$
$$\delta_2 = \vec{\Phi}_1\cdot\vec{\Phi}_7 + \vec{\Phi}_2\cdot\vec{\Phi}_4 + \vec{\Phi}_3\cdot\vec{\Phi}_8 + \vec{\Phi}_5\cdot\vec{\Phi}_6 \tag{4.56c}$$
$$\delta_3 = \vec{\Phi}_1\cdot\vec{\Phi}_8 + \vec{\Phi}_2\cdot\vec{\Phi}_5 + \vec{\Phi}_3\cdot\vec{\Phi}_7 + \vec{\Phi}_4\cdot\vec{\Phi}_6 \tag{4.56d}$$

$$a_1 = \vec{\Phi}_1\cdot\vec{\Phi}_3 + \vec{\Phi}_4\cdot\vec{\Phi}_5 \tag{4.57a}$$
$$a_2 = \vec{\Phi}_1\cdot\vec{\Phi}_4 + \vec{\Phi}_3\cdot\vec{\Phi}_5 \tag{4.57b}$$
$$a_3 = \vec{\Phi}_1\cdot\vec{\Phi}_5 + \vec{\Phi}_3\cdot\vec{\Phi}_4 \tag{4.57c}$$

$$b_1 = \vec{\Phi}_2\cdot\vec{\Phi}_6 + \vec{\Phi}_7\cdot\vec{\Phi}_8 \tag{4.58a}$$
$$b_2 = \vec{\Phi}_2\cdot\vec{\Phi}_7 + \vec{\Phi}_6\cdot\vec{\Phi}_8 \tag{4.58b}$$
$$b_3 = \vec{\Phi}_2\cdot\vec{\Phi}_8 + \vec{\Phi}_6\cdot\vec{\Phi}_7 \tag{4.58c}$$

We first minimize with respect to the δs, a's and b's obtaining a set of 7 conditions on the relative angles of the normal modes and a greatly simplified form for the free energy

$$\delta_o = \frac{S}{2}(M_2^2 - M_1^2) \tag{4.59}$$
$$\delta_i = S(b_i - a_i) \qquad i = 1..3 \tag{4.60}$$
$$a_i + b_i = 0 \qquad i = 1..3 \tag{4.61}$$

$$f(T,\vec{H}) = \mu_o \; -2H\left(\sqrt{\frac{\beta+J_{12}}{\beta}}\,\phi_1 + \sqrt{\frac{\beta-J_{12}}{\beta}}\,\phi_2 \right)$$

$$+ \frac{1}{2}(r_1 m_1^2 + r_2 m_2^2 + r_1' \phi_1^2 + r_2' \phi_2^2)$$

$$+ \frac{u}{4}(m_1^2 + m_2^2 + \phi_1^2 + \phi_2^2)^2 \qquad (4.62)$$

where

$$r_1 = n(T-T_c^1) = nT+\alpha+\beta \qquad (4.63a)$$

$$r_2 = n(T-T_c^2) = nT+\alpha-\beta \qquad (4.63b)$$

$$r_1' = n(T-T_c^{1'}) = nT-3(\alpha+\beta) \qquad (4.63c)$$

$$r_2' = n(T-T_c^{2'}) = nT-3(\alpha-\beta) \qquad (4.63d)$$

$$T_c^{1'} = -3T_c^1 \qquad (4.64a)$$

$$T_c^{2'} = -3T_c^2 . \qquad (4.64b)$$

As in the one-sublattice problem, there are no conditions determining the relative magnitudes of modes 3, 4 and 5, or modes 6, 7 and 8. Thus when either of m_1 or m_2 are magnetized, the internal 2 dimensional degeneracy discussed in Section 1 will be present. Which r's are critical depends on the signs of α and β and also on whether or not $|\alpha| < |\beta|$. Fig. 4.8 shows which regions of α, β space stabilize the $\vec{q} = 0$ modes.

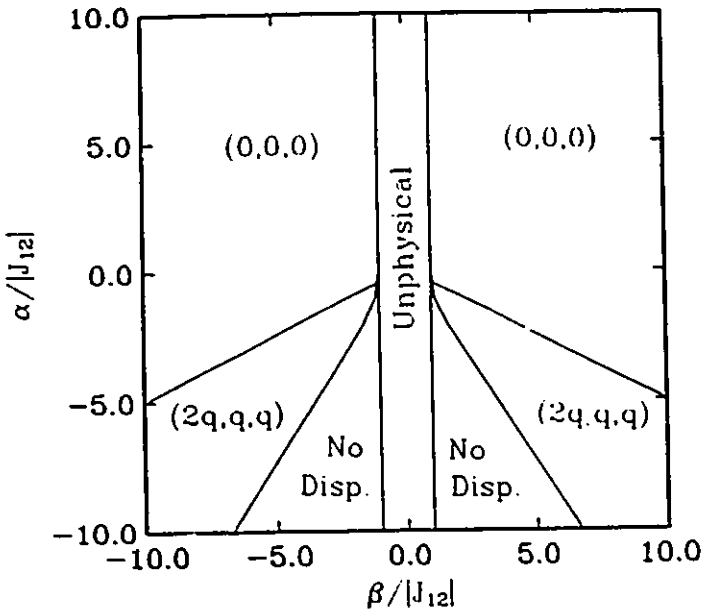

Fig. 4.8 Similar to Fig. 4.7 except parameterized in terms of α and β (defined in (5.1) and (5.2)) with $|J_{12}| = 1$.

One can see that, for $\alpha < 0$ in a region where $|\alpha| > |\beta|$ the system is incommensurate or dispersionless. This leaves three essentially different cases to consider.

Case 1: $|\alpha| < |\beta|$, $\beta > 0$

Modes Φ_1 and m_2 order spontaneously. The order of the T_c's is determined by α

$$0 < T_c^2 < T_c^{1'} \qquad \text{for } \beta > \alpha > -\frac{\beta}{2} \tag{4.65a}$$

$$0 < T_c^{1'} < T_c^2 \qquad \text{for } -\frac{\beta}{2} > \alpha > -\beta \tag{4.65b}$$

Case 2: $|\alpha| < |\beta|$, $\beta < 0$

Modes Φ_2 and m_1 order spontaneously. The order of the T_c's is determined by α

$$0 < T_c^1 < T_c^{2'} \qquad \text{for } -\beta > \alpha > \frac{\beta}{2} \tag{4.66a}$$

$$0 < T_c^{2'} < T_c^1 \qquad \text{for } \frac{\beta}{2} < \alpha < \beta \tag{4.66b}$$

Case 3: $|\alpha| > |\beta|$, $\alpha > 1$

Modes Φ_1 and Φ_2 order spontaneously. The order of the T_c's is determined by the sign of β

$$0 < T_c^{1'} < T_c^{2'} \qquad \text{for } \beta > 0 \tag{4.67a}$$

$$0 < T_c^{2'} < T_c^{1'} \qquad \text{for } \beta < 0 \tag{4.67b}$$

In general, then, all these systems will have two transition temperatures, and thus rather complex behavior can be expected from magnetization and susceptibility measurements. As an example I have calculated the thermal evolution of the uniform magnetization at zero field by solving the mean field equations (4.10) numerically. Fig. 4.9 shows the results for $J_1 = -1$, $J_2 = \frac{1}{2}$ and $J_{12} = -1$, which corresponds to case 2 with $T_c^{2'} > T_c^1$.

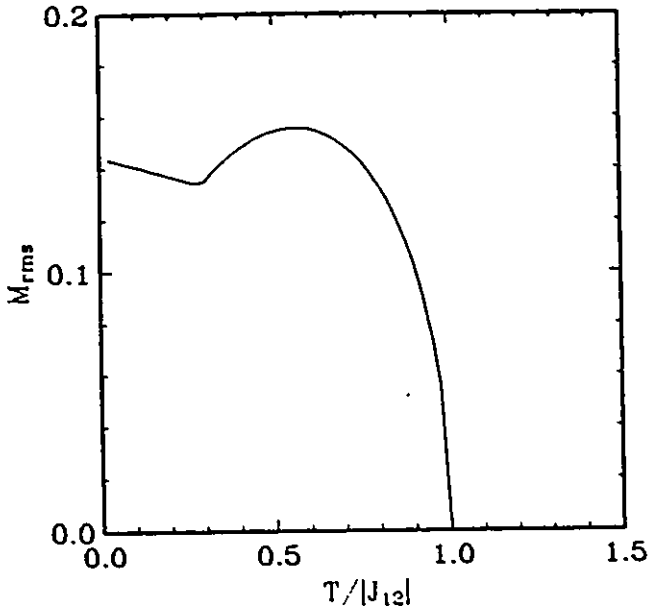

Fig. 4.9 Unusual temperature dependence of the uniform magnetization (calculated numerically from (4.10)) of a two sublattice system with exchange parameters $J_1 = -1, J_2 = \frac{1}{2}$ *and* $J_{12} = -1$, *corresponding to case 2.*

It is interesting to note that the numerical solutions of the mean field equations (4.10) also show that the value of ε (which determines the relative magnetizations of the A and B sublattices) deviates very slightly from the value given in (4.49) and is temperature dependant.

4.5 Discussion:

The prevailing theme throughout this chapter has been the unusually high degree of degeneracy in the ordered phases of pyrochlores. These degeneracies are of two sorts, the first being the internal 2 dimensional degeneracy with respect to the relative magnitudes of the three ordering modes $\vec{\Phi}_1$, $\vec{\Phi}_2$ and $\vec{\Phi}_3$. This sort of degeneracy is also present in type I fcc antiferromagnets[He87,La90] but not in triangular systems at zero field. Mean field analysis of the classical XY model on a triangular lattice[Le84] and classical dipoles on a honeycomb lattice[Zi88] also show a one dimensional internal degeneracy with respect to the relative orientations of the ordering sublattices.

The other type of degeneracy is the complete $\vec{q}$ independence of two of the eigenvalues of the coupling matrix for the NN one sublattice model. This means that for every possible $\vec{q}$ in the zone, there are two modes with the same free energy independent of $\vec{q}$ (within the MF approximation). This degeneracy is macroscopic, and no long range order is predicted within the MF approximation. For 3-dimensional systems such dispersionless modes over the whole zone are so far unique to the corner-sharing tetrahedral lattice. No such degeneracy occurs for stacked triangular lattice systems. It is interesting to note that Rastelli *et. al.*[Ra88] have found that the so-called "Rhombohedral Antiferromagnet" is degenerate along certain lines in $\vec{q}$ space, which they call "Degeneration lines". A similar sort of degeneracy occurs in the fcc Ising antiferromagnet with NN interactions[Da64]. Further neighbor interactions in the pyrochlore system will in general select the $\vec{q} = 0$ or incommensurate phases. The same sort of degeneracies arise in the two-sublattice (both A and B are magnetic) pyrochlore systems. In particular, over a large region of coupling parameter space, the system is dispersionless along the (0,q,q) direction.

One might expect that thermal fluctuations will reduce the degree of degeneracy

in these systems. In fact through low temperature expansions Larson and Henley[He87,La90] have shown that thermal fluctuations will select collinear ordered states in fcc antiferromagnets.

The mean field calculations presented here are certainly consistent with 1) the observed long range order in FeF_3, 2) the lack of long range order in many other pyrochlores and 3) some aspects of the unusual magnetization curves observed in $Nd_2Mo_2O_7$, $Sm_2Mo_2O_7$ and $Gd_2Mo_2O_7$[Sa86]. The question remains as to whether the dispersionless modes are responsible for the spin-glass-like behavior observed in the chemically ordered compounds, $Y_2Mo_2O_7$, $Y_2Mn_2O_7$ and $Tb_2Mo_2O_7$. It is plausible that the liquid-like magnetic neutron scattering, observed in $Tb_2Mo_2O_7$, is a result of the presence of many degenerate modes with different $\vec{q}$'s along (0,q,q). Other spin-glass-like properties, such as susceptibility cusps and sample history dependence can not really be described within the mean field approximation. They require a more sophisticated treatment.

Chapter 5

Thermal Fluctuations

5.1 Introduction:

In the last chapter on mean field theory some interesting and unusual results were obtained for pyrochlore antiferromagnets. In particular the complete degeneracy of all Fourier modes where NN interactions are concerned and the prediction of long range ordered $\vec{q} = 0$ phases which have degeneracies with respect to the relative orientation of the four magnetic sublattices. At this point an obvious question arises:

> What are the effects of going beyond mean field theory and including thermal fluctuations?

In general one might expect that thermal fluctuations lift some of the degeneracies. As well fluctuations can cause a second order phase transition, as predicted by mean field theory, to go first order. Such a transition is commonly known as a fluctuation induced first order transition and is common among systems with a large number of order parameter components.

The proper theoretical framework for dealing with thermal fluctuations involves rather sophisticated field theoretic techniques[Am88]. Work along these lines for the pyrochlore antiferromagnets is complicated by the non-bravias nature of the lattice, and would in itself be another full thesis. In order to deal with fluctuations I have chosen to use the Monte-Carlo technique described below. Monte-Carlo can in principle answer the above questions, unfortunately it cannot tell us why.

5.2 The Monte Carlo Method:

5.2.1 Introduction:

In general Monte-Carlo (MC) is a technique for evaluating high dimensional integrals. In statistical mechanics we are concerned with calculating averages of thermodynamic quantities

$$\langle A \rangle = \frac{1}{\mathcal{Z}} \sum_{\nu} A_{\nu} \exp\left[-\beta E_{\nu}\right] . \tag{5.1}$$

Where ν represents a point in the multidimensional phase space of the system. For a system of N classical spins (each with n componants)

$$\nu = \{\vec{S}_1, \vec{S}_2, \vec{S}_3, \ldots \vec{S}_N\} \tag{5.2}$$

we have an N(n-1) dimensional phase space. The summation (or set of integrals) in (5.1) rapidly becomes intractable in more than 6 phase space dimensions. A naive approach would be to choose points in phase space at random and approximate (5.1) over this finite set of points. In principle this will work however it is not very efficient since the Boltzmann factor, $\exp(-\beta E_{\nu})$, diminishes the contribution of high energy states in the summation considerably. At low temperatures (5.1) is completely dominated by the contribution of low energy states. A more efficient MC algorithm would give preference to points in phase space that make the largest contributions to (5.1). This is called importance sampling[Me53, Ch87, Bi79, Bi83, Mo84].

5.2.2 The Metropolis Algorithm:

Given some initial configuration of the spins, ν, one chooses a spin at random and moves it by a random amount generating a new configuration, ν'.

$$\begin{aligned} \nu &= \{\vec{S}_1, \vec{S}_2, \vec{S}_3, \ldots \vec{S}_i, \ldots \vec{S}_N\} \\ \nu' &= \{\vec{S}_1, \vec{S}_2, \vec{S}_3, \ldots \vec{S}'_i, \ldots \vec{S}_N\} \end{aligned} \tag{5.3}$$

Associated with this move is a change in energy $\Delta E_{\nu\nu'} = E_{\nu'} - E_{\nu}$ and a relative probability for the two states

$$\frac{P_{\nu'}}{P_{\nu}} = \exp\left[-\beta\Delta E_{\nu\nu'}\right] . \tag{5.4}$$

The master equation tells one that at equilibrium

$$-W_{\nu\nu'}P_{\nu} + W_{\nu'\nu}P_{\nu'} = 0 \tag{5.5}$$

where $W_{\nu\nu'}$ is transition rate from the state ν to ν'. Combining (5.4) and (5.5) we have

$$\frac{W_{\nu\nu'}}{W_{\nu'\nu}} = \frac{P_{\nu'}}{P_{\nu}} = \exp\left[-\beta\Delta E_{\nu\nu'}\right] . \tag{5.6}$$

A simple way of implementing this is to choose

$$W_{\nu\nu'} \propto \begin{cases} 1 & \text{if } \Delta E_{\nu\nu'} \le 0 \\ \exp(-\beta \Delta E\nu\nu') & \text{if } \Delta E\nu\nu' \ge 0 \end{cases} \tag{5.7}$$

which is known as the Metropolis algorithm [Me53]. Thus there is unit probability of accepting moves with $\Delta E \le 0$ and when ΔE is positive the move is accepted with exponential probability. An exponential probability is easily obtained by comparing a uniform random number distribution with the Boltzmann factor.

From the sequence of spin configurations provided by the Metropolis algorithm one can easily calculate the thermal expectation value of any quantity related to the spins. For example

$$\langle E \rangle = \frac{1}{N_\nu} \sum_\nu E_\nu . \tag{5.8}$$

5.2.3 The Histogram Method:

During the MC (Monte Carlo) simulation thousands of spin configurations are generated with a range of internal energies. An efficient way of storing all of this data is in the form of a histogram $H_\beta(E)$ where $\beta = 1/T$. To be more specific $H_\beta(E)$ is the number of spin configurations generated with energy between E and E+ΔE. The histogram is very easily converted into an approximation of the energy probability distribution

$$P_\beta(E_\nu) = \frac{H_\beta(E_\nu)}{\mathcal{Z}_\beta} \tag{5.9}$$

$$\mathcal{Z}_\beta = \sum_\nu H_\beta(E_\nu) \tag{5.10}$$

Through a simple transformation[Fe88,Fe89a,Fe89b] one can (in principle) now calculate the probability distribution at any temperature β'

$$P_{\beta'}(E_\nu) = \frac{P_\beta(E_\nu)\ \exp\left[(\beta-\beta')E_\nu\right]}{\sum_\nu P_\beta(E_\nu)\ \exp\left[(\beta-\beta')E_\nu\right]}$$

$$= \frac{P_\beta(E_\nu)\ \exp\left[(\beta-\beta')E_\nu\right]}{\mathcal{Z}_{\beta'}}. \qquad (5.11)$$

As a bonus one also obtains information about the temperature dependence of the partition function $\mathcal{Z}_\beta$ and therefore the free energy $F_\beta = -\beta^{-1}\ln(\mathcal{Z})$ to within a constant. It is now a trivial matter to calculate the moments $\langle E\rangle_\beta$, $\langle E^2\rangle_\beta$ etc, as continuous functions of temperature. For the work presented below a more general distribution $P_\beta(E,m_s)$ has been calculated, thus allowing the order parameter $\langle m_s\rangle_\beta$ and its fluctuations to be calculated.

$P_\beta(E)$ is usually a sharply peaked function about $\langle E\rangle_\beta$. In the tails of the distribution $H_\beta(E)$ is very small with poor counting statistics, resulting in a large relative error in $P_\beta(E)$ in the tails. The upshot is that $P_\beta(E)$ really only contains information on the distributions (through 5.11) at nearby temperatures. Thus one must still simulate at a number of temperatures in order to calculate thermodynamic functions over a wide temperature range. Ferrenberg and Swendsen have proposed an optimized method of combining histogram data for different temperatures[Fe89a,Fe89b], which has been implemented.

5.2.4 Limitations of Monte-Carlo:

MC calculations are plagued by finite simulation lengths and finite lattice size effects. In order to get a factor of 2 improvement in statistical errors of thermodynamic quantities one must increase the simulation length by a factor of 4. However the histogram method gives a considerable improvement in data quality over conventional MC techniques, for an equal investment in computer time.

Near a phase transition finite size effects become important for two reasons

1) The relaxation time (τ_{relax}) becomes long (diverges for infinite systems) near T_c. This is known as critical slowing down.

2) The correlation length becomes larger then the system size.

To overcome the critical slowing down problem one must simply increase the length of the simulation such that $\tau_{sim} >> \tau_{relax}$.

There is no way to avoid finite size effects, which tend to round off sharp features in the thermodynamic quantities at T_c. However Fisher[Fi71,Fi72,La76a, La76b] has proposed scaling laws obeyed by the free energy and the order parameter for finite systems

$$F(t,L) = L^{(2-\alpha)/\nu} f(L^{1/\nu}t) \tag{5.12}$$

$$m_s(t,L) = L^{-\beta/\nu} f_m(L^{1/\nu}t) \tag{5.13a}$$

$$\chi_s(t,L) = L^{\gamma/\nu} f_\chi(L^{1/\nu}t) \tag{5.13b}$$

$$C_H(t,L) = C_1 + L^{\alpha/\nu} f_C(L^{1/\nu}t) \tag{5.13c}$$

where

L is the system size, $N \propto L^3$

$t = (T-T_c(\infty))/T_c(\infty)$ is the reduced temperature

α, β, γ and ν are critical exponents.

$\mathcal{f}$, $\mathcal{f}_m$, $\mathcal{f}_\chi$, and $\mathcal{f}_C$ are unknown scaling functions.

For example (5.13a) tells us that for a plot of $m_s L^{\beta/\nu}$ vs $L^{1/\nu}t$, all of the data for different lattice sizes should collapse onto a single line, if the critical exponents and $T_c(\infty)$ are chosen correctly. Through finite size scaling one can actually obtain estimates of infinite lattice exponents by simulating systems with $N \leq 10^4$.

5.3 Results for $J_1 = -1$ and $J_{NNN} = 0$:

For this model with antiferromagnetic nearest neighbor interactions and no further neighbor interactions, the mean field theory predicted no long range order because of the complete $\vec{q}$ degeneracy of the Fourier modes. Long range order is always accompanied by a sharp phase transition with anomalies in the thermodynamic quantities. In particular one might expect an anomaly and finite size effects in the heat capacity. Simulations for two lattice sizes L = 2 with 128 spins and L = 4 with 1024 spins, were carried out. Periodic boundary conditions were implemented to eliminate surface effects. Data were obtained in the temperature range $.05 \leq T/|J_1| < 6.0$ with simulation lengths ranging from 50000 to 400000 Monte-Carlo steps per spin (MCS), depending on temperature.

The internal energy and heat capacity for the two lattice sizes are shown in Fig. 5.1.

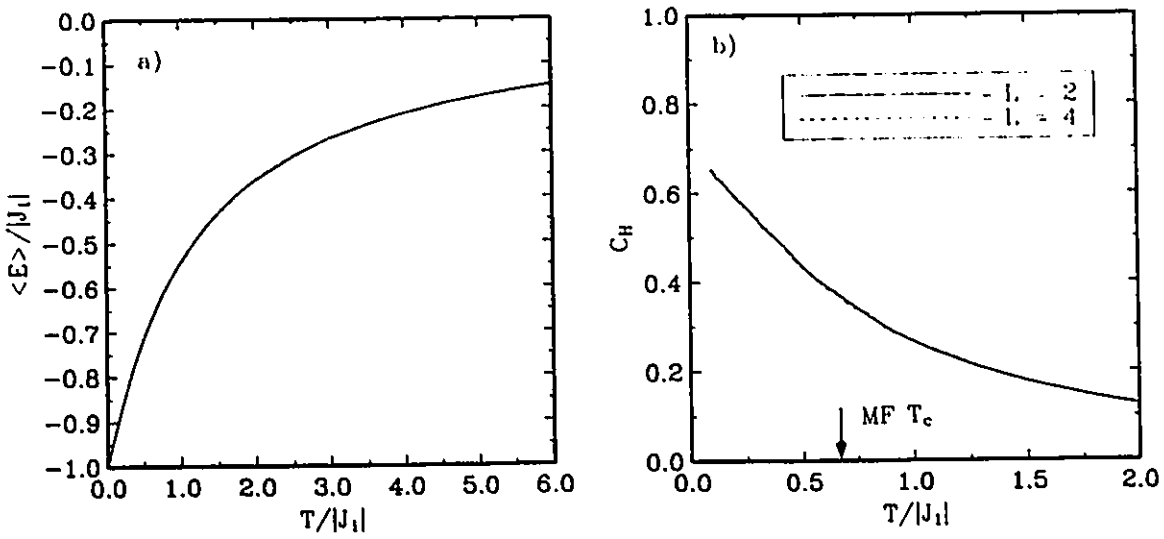

Fig. 5.1 Internal energy per spin (left) and the heat capacity per spin (right) for the NN pyrochlore antiferromagnet.

Except for a little noise in the heat capacity data there are no anomalies or finite size effects. At low temperatures the internal energy is seen to approach a ground state energy near -1.0. In fact a linear extrapolation gives E(T=0) = -1.0 to within .01%.

In light of the fact that the order parameter for this model is not known I have chosen to calculate the mean sublattice magnetization which is a measure of the $\vec{q} = 0$ Fourier modes.

$$m_s^2 = \frac{4}{N^2}\left\langle \sum_{a=1}^{4} m_a^2 \right\rangle \tag{5.14}$$

where

$$\vec{m}_a = \sum_i \vec{S}_i^a \tag{5.15}$$

and as before i labels a unit cell and a labels a sublattice within the unit cell. The sublattice magnetization and its associated staggered susceptibility are shown in Fig. 5.2

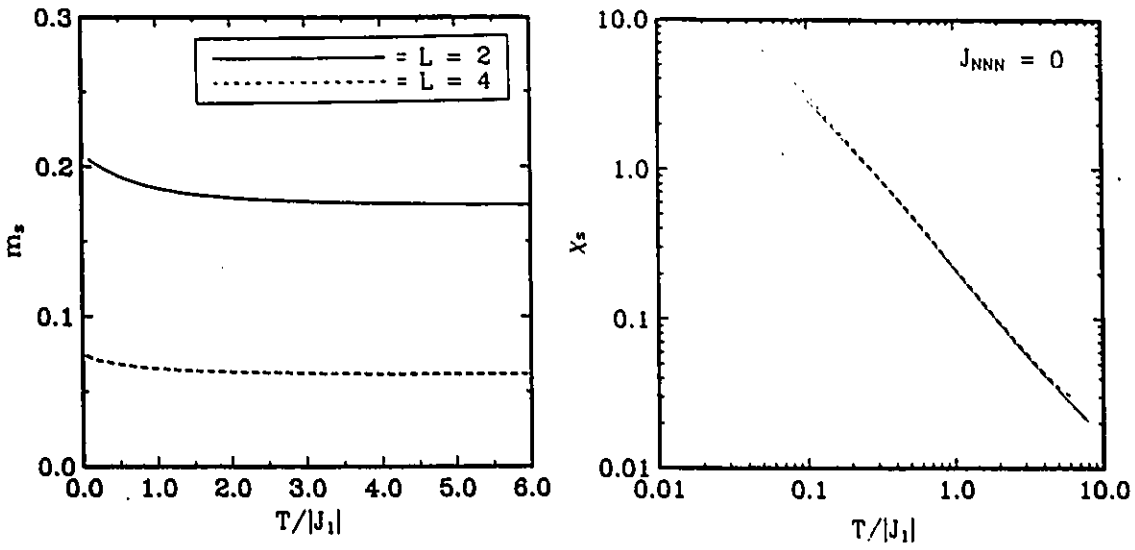

Fig. 5.2 Sublattice magnetization and susceptibility for the NN pyrochlore antiferromagnet.

Dramatic size effects are seen in m_s between L = 2 and L = 4. However the size effects have nothing to do with a phase transition. As one increases the system size

the number of allowed Fourier modes also increases thus decreasing the relative contribution of the $\vec{q} = 0$ mode and m_s. The log-log plot of the susceptibility indicates a T^{-1} behavior over about two and half decades in temperature. As χ_s is defined by

$$\chi_s = \frac{1}{T}(\langle m_s^2 \rangle - \langle m_s \rangle^2) \tag{5.16}$$

we see that the average fluctuations in m_s remain roughly constant at all temperatures.

As stated previously the histogram method enables one to calculate the partition function $\mathcal{Z}$ to within a multiplicative constant. This results in an unknown temperature dependant term in the free energy and a related unknown constant in the entropy. These unknown constants have been determined by fixing the infinite temperature entropy per spin to equal $\ln(4\pi)$. The resulting free energy and entropy are shown in Fig. 5.3.

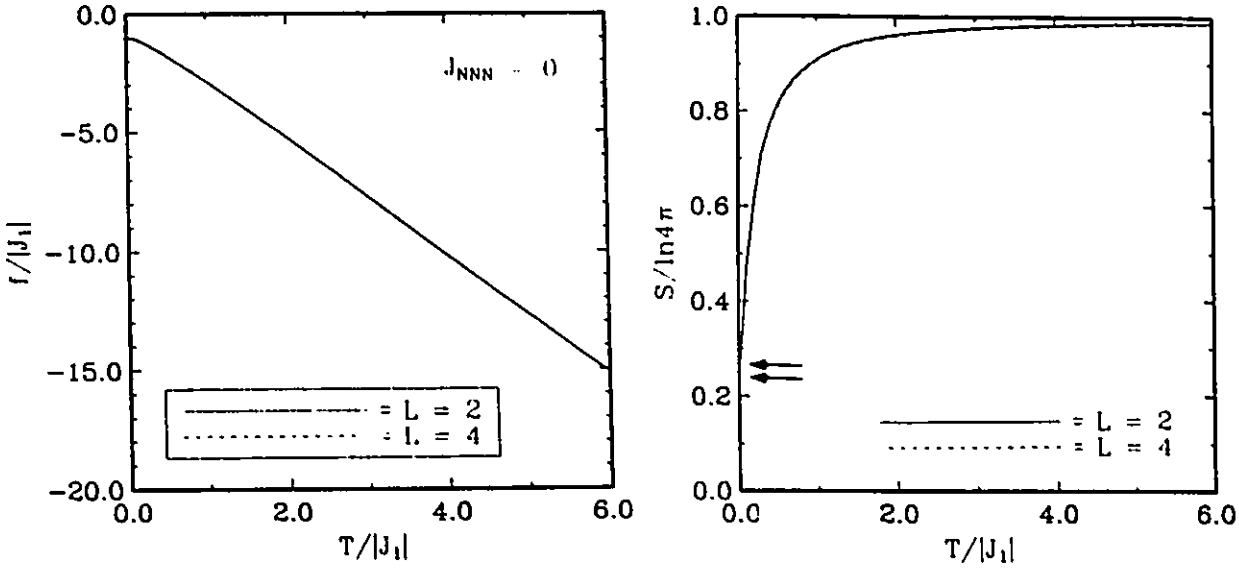

***Fig 5.3** Free energy per spin (left) and the entropy per spin (right) for the NN pyrochlore antiferromagnet. The arrows indicate the extrapolated ground state entropy for the two lattice sizes.*

At zero temperature one sees that the free energy approaches -1.0 which is equal to the ground state energy as expected. Of more interest is the entropy which talks about the degree of randomness in the system. Below T = $|J_1|$ the entropy starts to decrease rapidly. This can be understood in terms of short range ordering of the spins. The entropy a T = 0 is very difficult to determine because of the very strong temperature dependence of S at low temperatures. A carefull extrapolation procedure gives S(T=0,L=2) ≈ .22 and S(T=0,L=4) = .26. Whether or not the system has a finite ground state entropy is a rather important question. Since Monte-Carlo is not very

efficient at low temperatures the answer will be confirmed by other means.

Through a simple application of counting degrees of freedom we can see why the ground state entropy per spin should be finite. Each spin has two degrees of freedom $\{\theta,\phi\}$ for a total of 2N degrees of freedom for a system with N spins. There are N/2 tetrahedra in the system (four spins per tetrahedron and each spin is shared by two tetrahedra). The ground state condition for a single tetrahedron is

$$\vec{S}_1 + \vec{S}_2 + \vec{S}_3 + \vec{S}_4 = 0 \tag{5.17}$$

which gives at most $\frac{3}{2}$N constraints on the system that must be satisfied in the ground state. I say at most $\frac{3}{2}$N, because it will require a little more thought to decide whether or not all of the conditions are linearly independent. In any case this leaves at least N/2 remaining continuous degrees of freedom in the system. which means that the ground state entropy is proportional to N and the entropy per spin will remain finite in the thermodynamic limit ($N \to \infty$).

All of the evidence seems to indicate that the NN pyrochlore antiferromagnet does not order at any temperature. There are a number models with no long range order at non-zero temperature that do order at T = 0, *i.e.* have zero ground state entropy per spin. All 1 dimensional systems and the 2 dimensional Heisenberg model are examples. In these systems the density of states above the ground state manifold is so high that entropy effects will destroy long range order at any non-zero temperature. There are also some interesting systems such as the fcc ising antiferromagnet with infinite ground state degeneracy that order at finite temperature due to entropy effects[Da64]. This is opposite to the situation for one dimensional systems. Finally there are models that remain paramagnetic at all temperatures. Examples include 2-d antiferromagnetic triangular and Kagomé lattices with ising spins[Li86]. The pyrochlore NN antiferromagnet seems to belong to this group.

5.4 Results for $J_1 = -1$ and $J_3/|J_1| = 0.1$

For this model the mean field theory predicted a $\vec{q} = 0$ ordered phase with a nine component order parameter made up from the three modes $\vec{\varphi}_1$, $\vec{\varphi}_2$ and $\vec{\varphi}_3$ (see table 4.5) and

$$T_c/|J_1| = \frac{1}{3}(2 + 12J_3/|J_1|) = 1.06666 . \qquad (5.18)$$

Simulations were performed for a number of lattice sizes L = {3,4,5,6,7,8,10} with simulation lengths ranging from 20000 to 100000 MCS at each temperature. The longest runs were near T_c. For the largest lattice L=10 corresponds to 16000 spins which not far from being state of the art in MC simulations with Heisenberg spins (by far the most difficult case).

Fig. 5.4 shows the temperature dependence of the internal energy and the heat capacity.

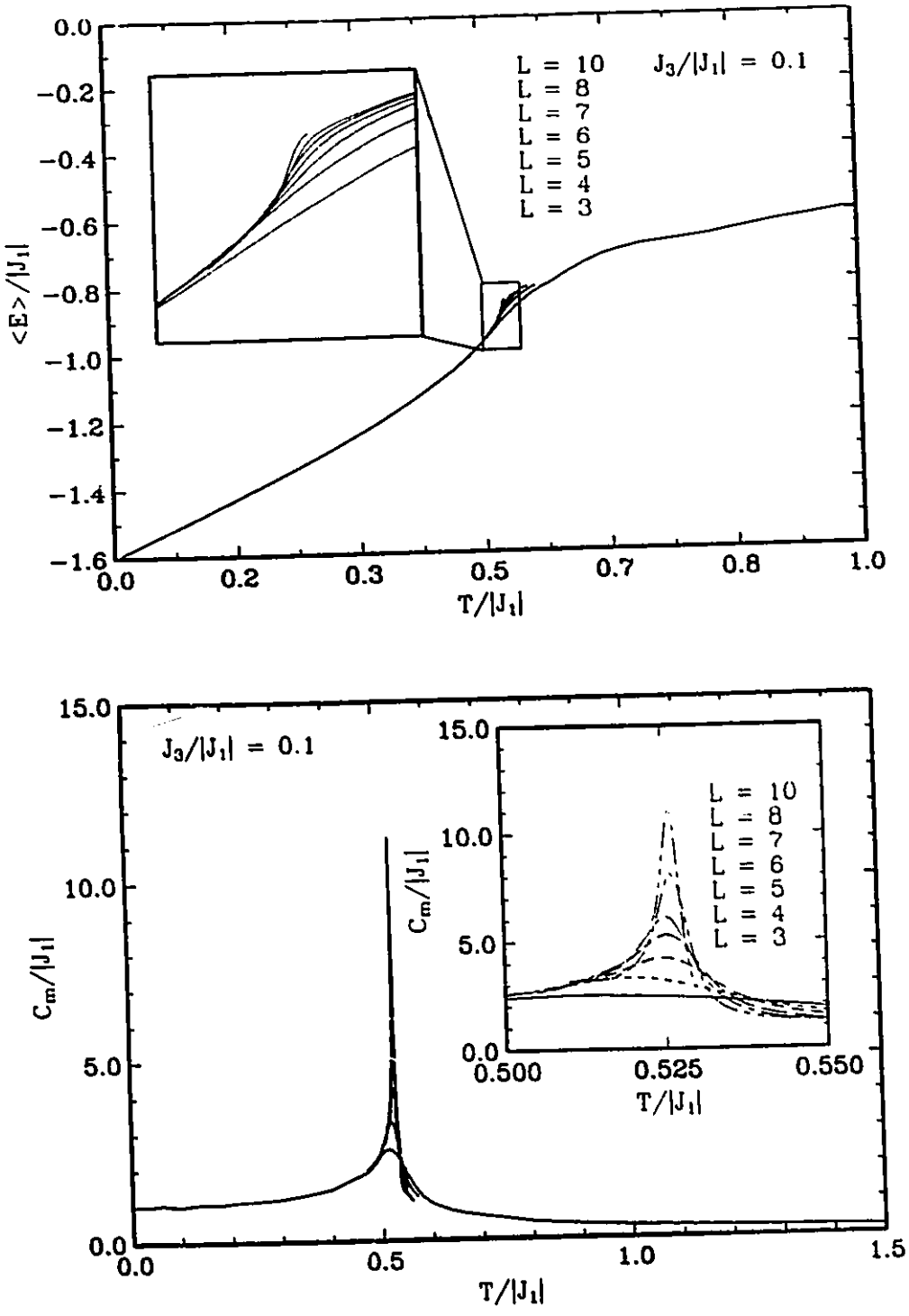

Fig. 5.4 Internal energy (top) and the heat capacity (bottom) for the antiferromagnetic pyrochlore with NNN interaction.

The energy approaches $-1.6|J_1|$ as $T \to 0$ which is in agreement with a simple ground state calculation. Near $T = .5|J_1|$ one can see in the heat capacity clear evidence for a phase transition. The mean field transition temperature has been renormalized by almost a factor of $\frac{1}{2}$ by thermal fluctuations. Since this is a $\vec{q} = 0$ ordered phase the order parameter defined in (5.14) should be relevant. Fig. 5.5 shows the behavior of m_s and χ_s.

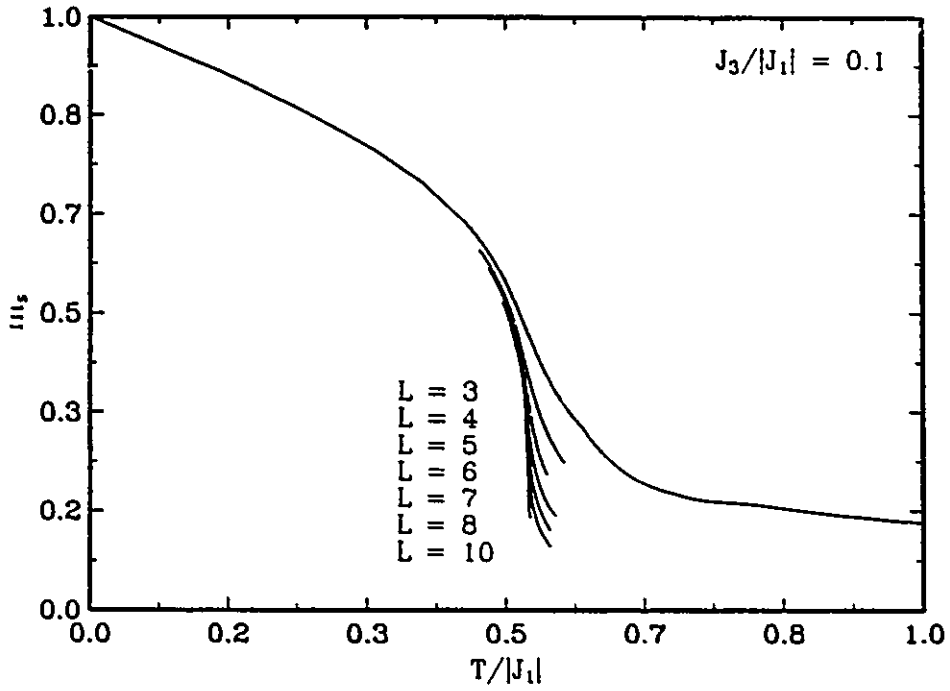

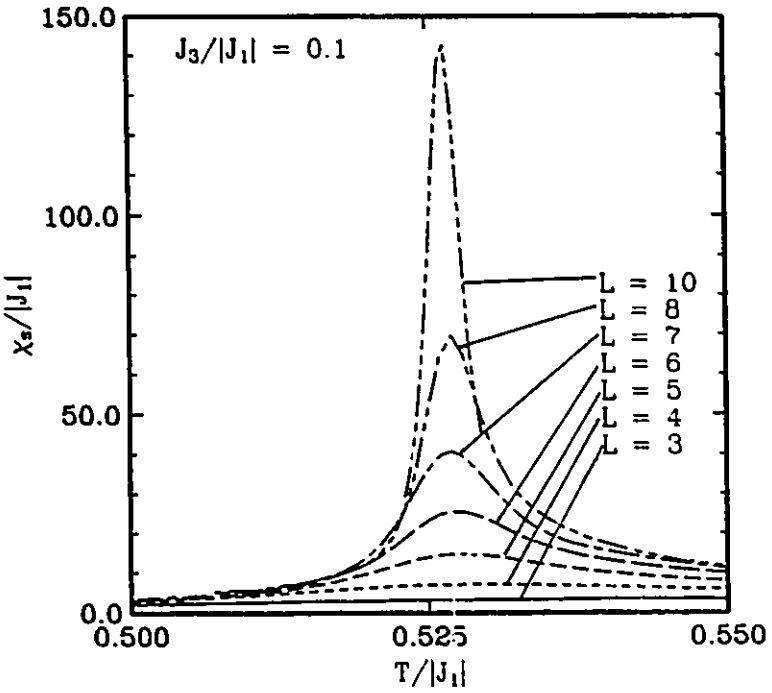

Fig. 5.5 Temperature dependence of the order parameter m_s and its fluctuations χ_s for the pyrochlore antiferromagnet with NNN interaction.

The fact that χ_s seems to be diverging at T_c indicates that m_s is the correct order parameter.

The first question to answer when investigating critical phenomena in an unknown system is whether the transition is first order or second order. Mean field theory tells us that it is second order, but mean field results are often wrong in this respect. Considering the large number of order parameter components this transition may be a fluctuation induced first order transition. The first thing is to check for discontinuities in <E> and m_s, however no such discontinuities are evident in Fig. 5.4. A more sophisticated approach is to investigate how the maximum in C_H and χ_s scale with the lattice size L. Scaling predicts the following behavior for large enough L

First Order:

$$C_{max} \propto C_1 + C_2 L^d \tag{5.19a}$$

$$\chi_{max} \propto \chi_1 L^d \tag{5.19b}$$

Second Order

$$C_{max} \propto C_1 + C_2 L^{\alpha/\nu} \tag{5.20a}$$

$$\chi_{max} \propto \chi_1 L^{\gamma/\nu}. \tag{5.20b}$$

Here C_1 is the regular or non-critical part of the heat capacity. One immediate problem is how do we know if L is "large enough" for the scaling laws to work? A best fit for the neat capacity data is shown in Fig. 5.6 giving α/ν = 1.8(20) which is unusually large but far from d = 3..

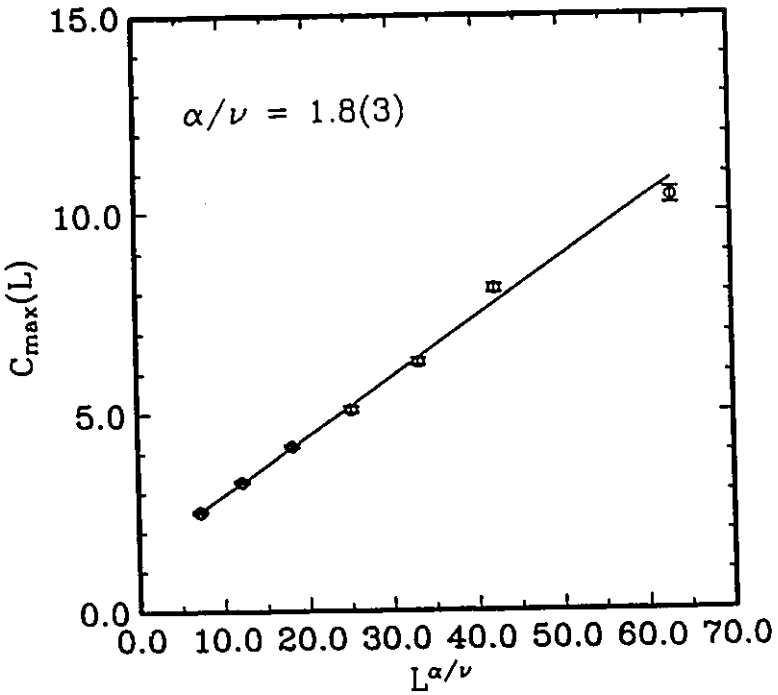

Fig 5.6 Size dependence of the heat capacity maximum giving α/ν = 1.8(20).

The effect of not including data for the smaller lattice sizes has very little effect on α/ν. This result clearly points towards a second order transition. Similar analysis for the susceptibility data is less conclusive giving γ/ν = 3.3(2) when all data is included and γ/ν = 2.6(1) when only data for the larger lattice sizes is considered.

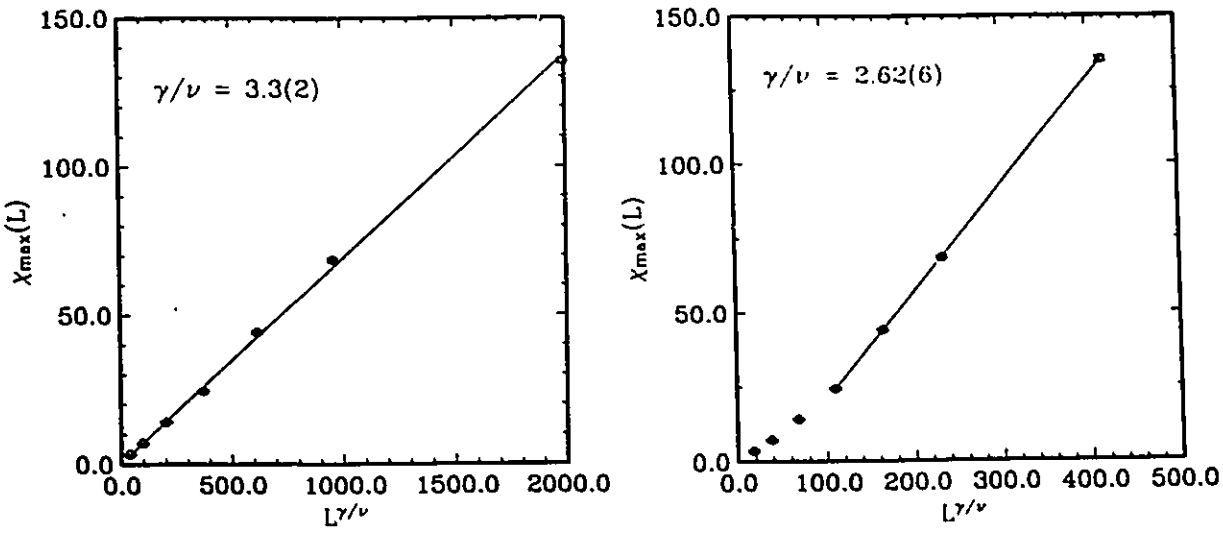

Fig. 5.7 Scaling analysis of χ_{max} giving $\gamma/\nu = 3.3(2)$ with all L (left) and $\gamma/\nu = 2.6(1)$ with $L \geq 5$ (right).

This result is consistent with both first and second order phase transitions.

Yet another rather sensitive test suggested by Binder[Bi82] is to examine the behavior of the fourth energy cumulant

$$U_L = 1 - \frac{\langle E^4 \rangle}{3\langle E^2 \rangle^2}. \tag{5.21}$$

This quantity is a measure of the deviation of the energy distribution P(E) from Gaussian form. Away from T_c $U_L = \frac{2}{3}$. For a second order transition U_L will

approach $\frac{2}{3}$ at T_c as $L \to \infty$. In the first order case U_L approaches some non-trivial value $U^* < \frac{2}{3}$ as $L \to \infty$. U_L will obey the folling scaling law

$$U_{min}(L) = U^* + CL^{-\alpha/\nu} \tag{5.22}$$

Fig. 5.8 shows the behavior of U_L with temperature and lattice size.

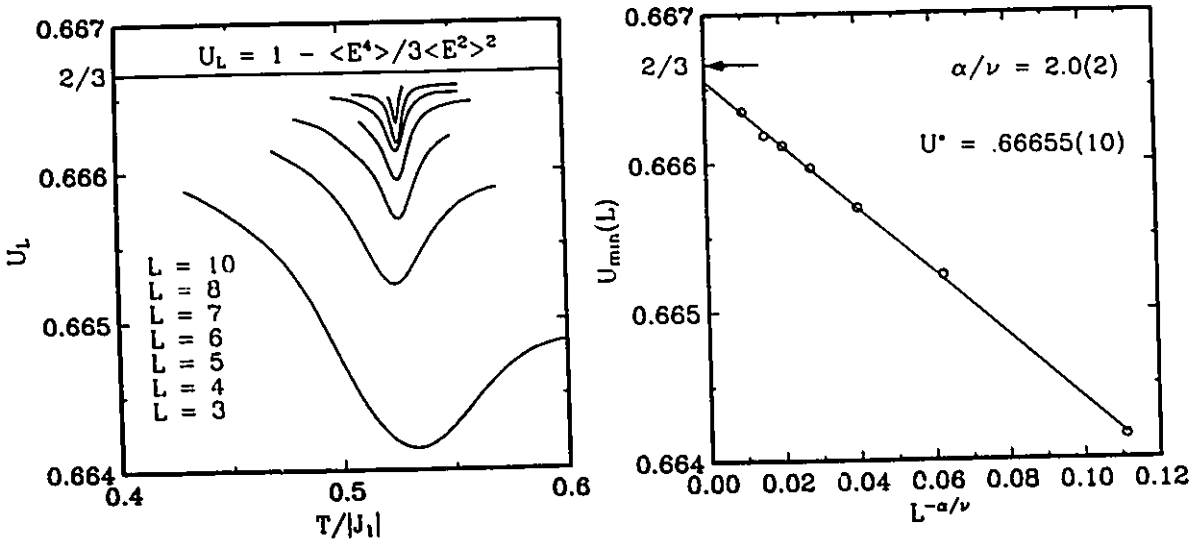

Fig 5.8 Left: the behavior of U_L with temperature for various lattice sizes. Right: Scaling if U_{min} giving $\alpha/\nu = 2.0(2)$ and $U^* = .66655(10)$.

The value obtained for α/ν reenforces the prediction from the heat capacity data. The deviation of U^* from 2/3 is on the order one part in 6000!. Things are starting to look second order ... for now.

The next item on the MC check list is to analyze the size dependence of T_c. For each lattice size we can define T_c in terms of $T(C_{max})$, $T(\chi_{max})$ and $T(U_{min})$. Scaling theory predicts

$$T_c(L) = T_c(\infty) + CL^{-1/d}, \quad \text{First Order} \tag{5.23a}$$

$$T_c(L) = T_c(\infty) + CL^{-1/\nu} \quad \text{Second Order.} \tag{5.23b}$$

A reasonable fit could only be obtained if the L = 3 and 4 data were not included.

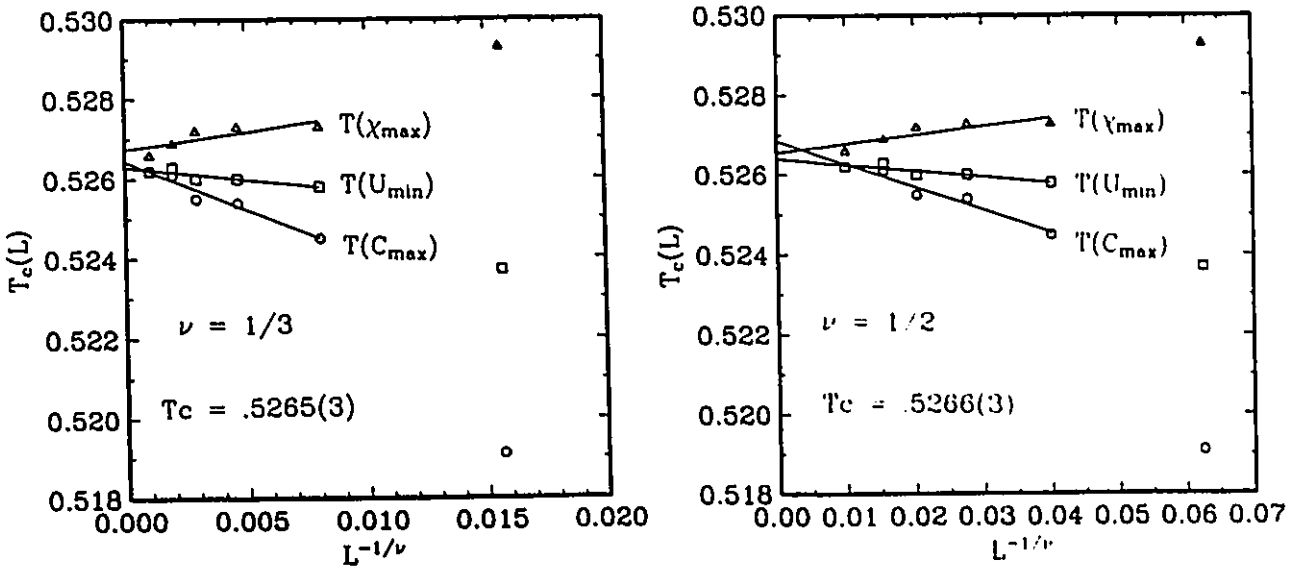

Fig. 5.9 Scaling of the T_c's for $\nu = 1/3 = 1/d$ (left) and $\nu = 1/2$ (right).

The quality of the fit was just as good for both values of ν, giving $T_c(\infty)$ =

.5265(3)$|J_1|$ in both cases. Here the great power of the histogram method is evident. T_c has been determined to within .06% which is an unheard of degree of accuracy in confentional MC data analysis. The fits became steadily worse for $\nu > 1/2$. Again an ambiguous result concerning the order the transition.

One final check to determine the nature of the transition is to inspect the probability distribution $P(E,m_s)$ (Fig 5.10) right at T_c. If $P(E,m_s)$ is double peaked with both peaks having the same intensity then the transition is first order, other wise it is second order with only one maximum.

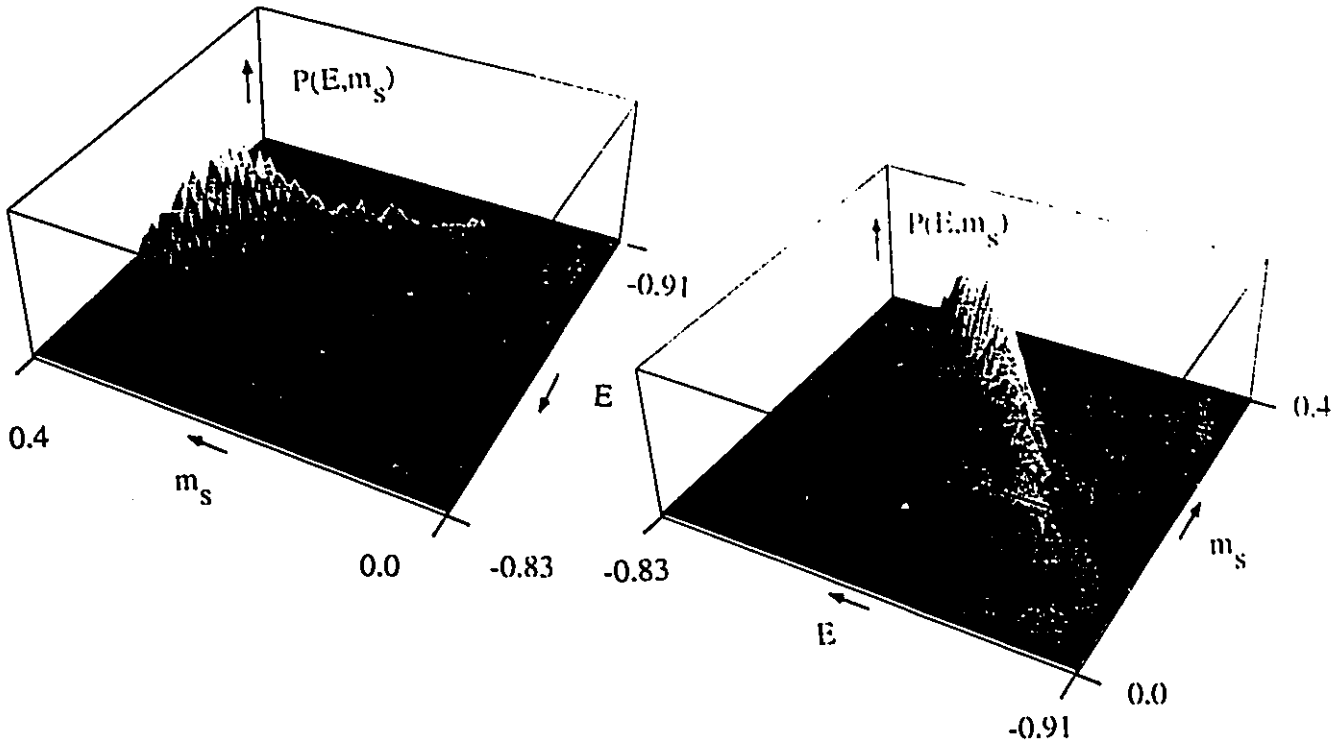

Fig. 5.10 The probability distribution $P(E,m_s)$ at T_c for L = 10 from two different angles.

$P(E,m_s)$ is seen to have essentially one maximum (except for sharp spikes due to noise) and is rather broad in m_s as reflected in the large values of χ_s. Of particular interest is the long tail in the distribution at low m_s and high E. There may actually be a very

weak local maximum at the end of the tail which indicates that there is a metastable phase that the system can sample. This is not consistent with a first order transition where the two maxima should be equal in intensity at T_c. If the maximum is real and not just an artifact of noise in the data, it may have a profound effect on the critical fluctuations in the system.

So far only the data at $T_c(L)$ has been considered. The finite-size scaling relations in (5.13) indicate that the data should scale away from T_c also. Fig. 5.11 shows the scaling fits for the order parameter and the ordering susceptibility.

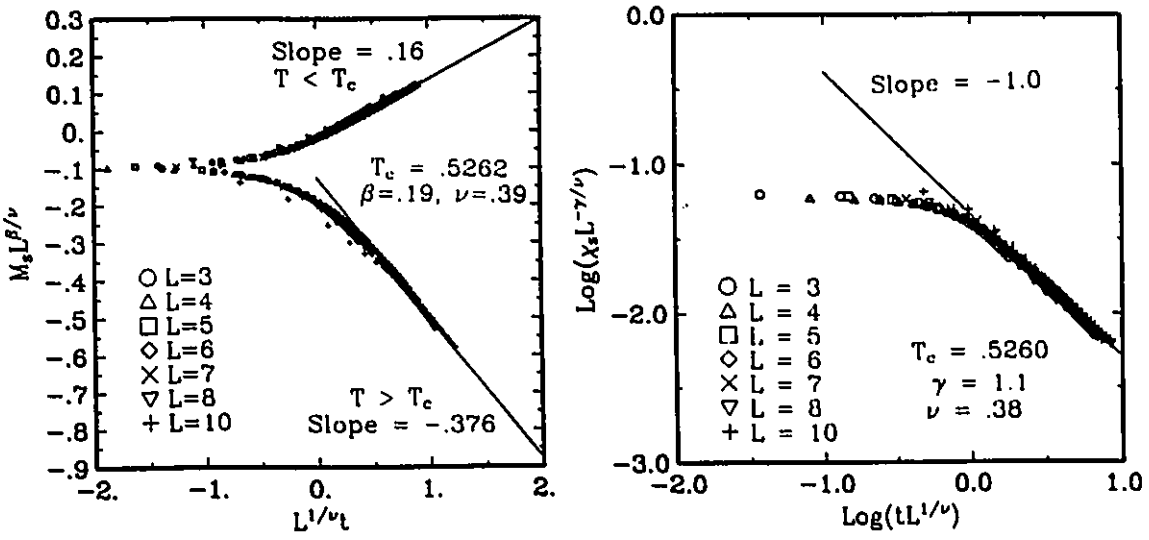

Fig. 5.11 Finite size scaling of the order parameter and the ordering susceptibility. best values for the exponents are listed in the figures.

For large x the scaling functions are expected to have the following asymptotic

behavior

$$\begin{aligned} \mathcal{M}(x) &= x^{\beta}, \quad T < T_c \\ \mathcal{M}(x) &= x^{\beta-3\nu/2}, \quad T > T_c \\ \mathcal{X}(x) &= x^{-\gamma} \end{aligned} \tag{5.24}$$

which are reasonably consistent with the linear fits to the data for large x in Fig. 5.11. Attempts to scale the susceptibility data above T_c were unsuccessful.

Scaling of the specific heat has also been attempted but this is much more difficult because the regular part of C_H is not known. Some progress can be made if we assume a very simple form for the regular part, C_1, by assuming that it is constant but different above and below T_c. Now one must search around in a five dimensional parameter space (T_c,α,ν,C_1^-,C_1^+) to get the data to scale as well as possible. This turns out to be very difficult particularly since the statistical errors in the data are not negligible.

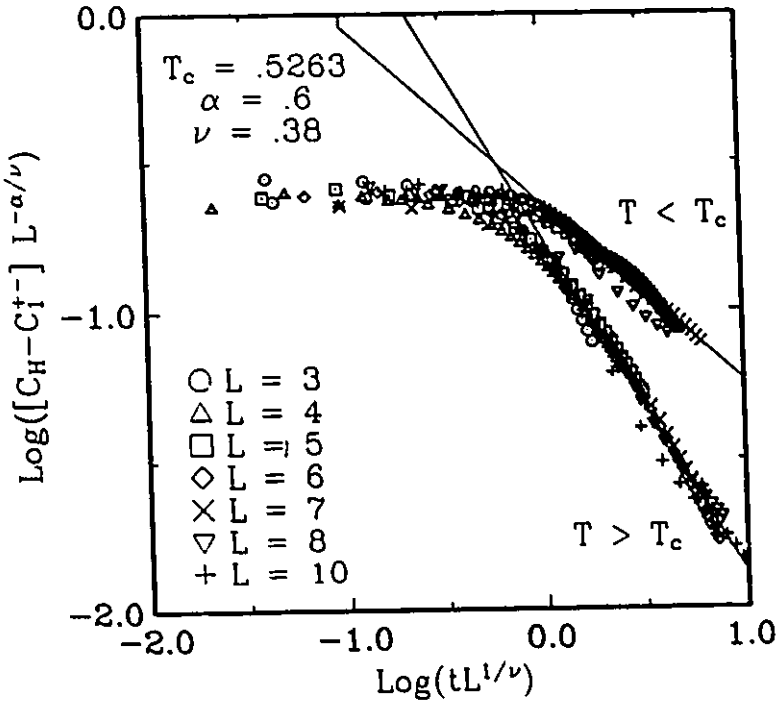

***Fig. 5.12** Finite size scaling of the heat capacity data with $C_1^- = 1.1$ and $C_1^+ = .8$. Other parameters are listed in the figure. The asymptotic slopes above and below T_c are -1.1(1) and -.60(2) respectively.*

The asymptotic behavior below T_c agrees very well with the expected behavior $f_C(x) \approx x^{-\alpha}$. This does not seem to work above T_c where the slope (-1.1) is far to large. One possible explanation for the discrepancy is that the regular part of the heat capacity C_1 is temperature dependant. Attempts to scale the data above T_c with a different value of α were unsuccessful.

If one believes that this phase transition is second order the we have the following set of critical exponents with liberal estimates for the errors

$$\begin{aligned} \beta &= .18(2) \\ \nu &= .39(2) \\ \gamma &= 1.1(1) \\ \alpha &= .6(1)\,. \end{aligned} \tag{5.25}$$

These exponents should be compared with the standard exponents in Table 1.1. They are not even remotely close to the exponents for any of the known universality classes!

Using rigorous thermodynamic arguments one can show that the following inequality (first derived by Rushbrooke[Ru63]) must hold.

$$\alpha + 2\beta + \gamma \geq 2 \tag{5.26}$$

As well phenomenological scaling theory[Wi65, Ka66, Ka67, Fi74] predicts that the equality in fact holds. Using the exponents above (5.25) one finds that $\alpha + 2\beta + \gamma =$ 2.06(15) which is on the right side of the rigorous inequality and also consistent with scaling. Another scaling law (more correctly a hyper-scaling law) which lies on much less rigorous grounds than (5.26) is

$$d\nu + \alpha = 2 \tag{5.27}$$

which involves the system dimensionality d. From (5.25) one obtains $d\nu + \alpha = 1.8(1)$ which is not in very good agreement with (5.27). Fisher has pointed out[Fi74] that this scaling breaks down (using the renormalization group language) in the presence of so called "dangerous irrelevant variables" and also in the presence of marginal variables. Further discussion of this point is beyond the scope of this thesis.

Recently there has been much interest (and controversy) in critical exponents for frustrated triangular lattice antiferromagnets. Kawamura[Ka88, Ka89] has shown

through MC simulations that these systems show so called non-universal critical exponents. These results have been verified by a number of experiments[Ma89, Ga88, Ka87].

Table 5.1

Critical exponents in Triangular lattice antiferromagnets[Ka88].

	XY	Heisenberg
β	0.25	0.28
γ	1.1	1.1
α	0.4	0.34
ν	0.53	0.55

This is understood by realizing that the symmetry of the order parameter (Fig. 1.2 120° structure) is drastically different than that for collinear systems. Since the exponents are therefore completely consistent with the universality hypothesis there is no reason to call them non-universal.

5.5 Measurement of β:

The two easiest exponents to measure on a powder sample are β (by neutron diffraction) and α. Below $T_c \approx 16K$ extra peaks appear in the diffraction pattern for FeF_3 which can be followed as a function of temperature. By doing a Rietveld refinement at each temperature on can obtain the ordered moments and β. No real compound can be expected to have the same hamiltonian as the ideal model system discussed in sec 5.4. However if we believe in universality then it is plausible that further neighbor interactions, dipole interactions and quantum effects are irrelevant.

Fig. 5.13 show a sample of one of the Rietveld fits and Fig. 5.14 shows the

Log-Log plot of the order parameter.

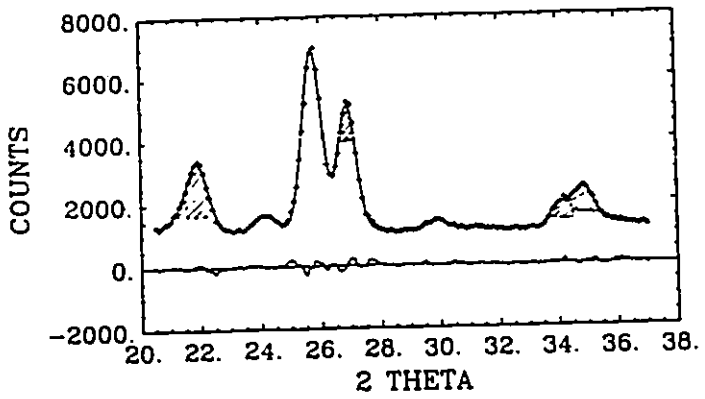

Fig 5.13 Rietveld fit of the nuclear and magnetic scattering for FeF_3 at 7K. Shading indicates where the magnetic scattering occurs.

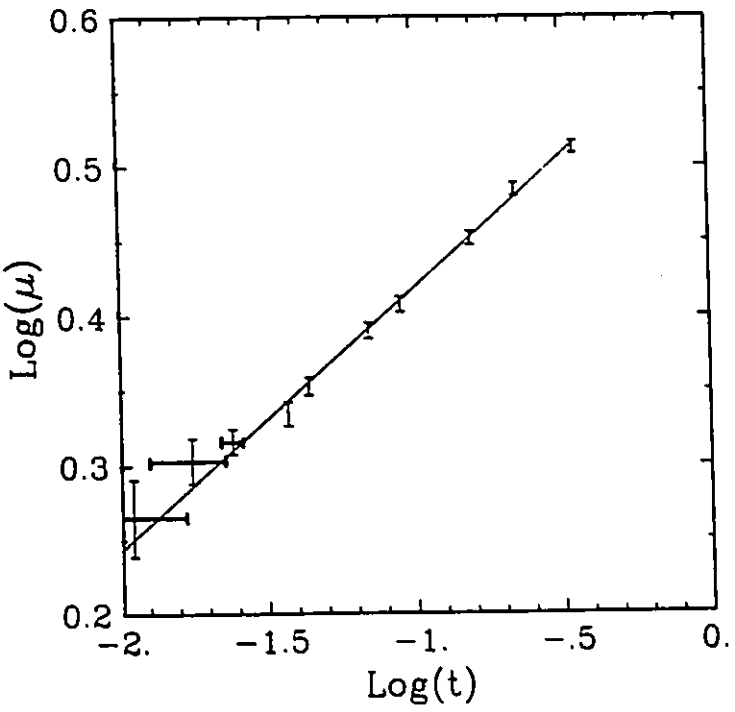

Fig. 5.14 Log-Log plot of the ordered moment μ vs. reduced temperature t for FeF_3 giving T_c = 15.4(1)K and β = .18(2).

Due to problems with removing critical scattering and temperature control it was only possible to obtain reliable data over a range of one and a half decades in reduced temperature t. Also because T_c could not be determined independently the uncertainty in β is increased. Nevertheless the agreement with the Monte-Carlo results (5.25) is encouraging.

5.6 Collinearity:

As stated previously mean field theory predicted that the relative magnitudes of

the three critical modes φ_1, φ_2 and φ_3 was indeterminate. Thus collinear structures such as ($\varphi_1 = m$, $\varphi_2 = 0$, $\varphi_3 = 0$) will be degenerate with noncollinear structures ($\varphi_1 = m/\sqrt{3}$, $\varphi_2 = m/\sqrt{3}$, $\varphi_3 = m/\sqrt{3}$). Fig. 5.15 shows this schematically.

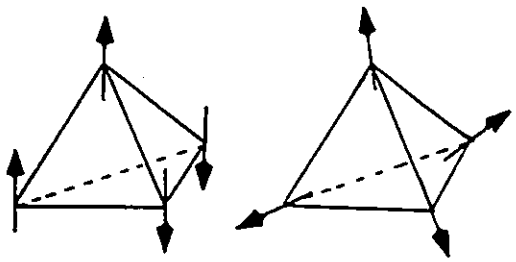

Fig. 5.15 A collinear spin arrangement (left) and a non-collinear spin arrangement (right).

Henley[He86, He90] has shown that type I and type III fcc antiferromagnets prefer collinear ordered states. In order to check that this is the case in pyrochlores I have defined and calculated (by Monte-Carlo) a "Collinearity function" for pyrochlores

$$\varphi_{cl} = \frac{1}{2}\left\{ \frac{\varphi_1^4+\varphi_2^4+\varphi_3^4}{\left[\varphi_1^2+\varphi_2^2+\varphi_3^2\right]^2} - \frac{1}{3} \right\}. \qquad (5.28)$$

For a collinear structure $\varphi_{cl} = 1$ and in the non-collinear limit $\varphi_{cl} = 0$. The probability distribution $P(\varphi_{cl})$ in shown in Fig. 5.16 for two lattice sizes.

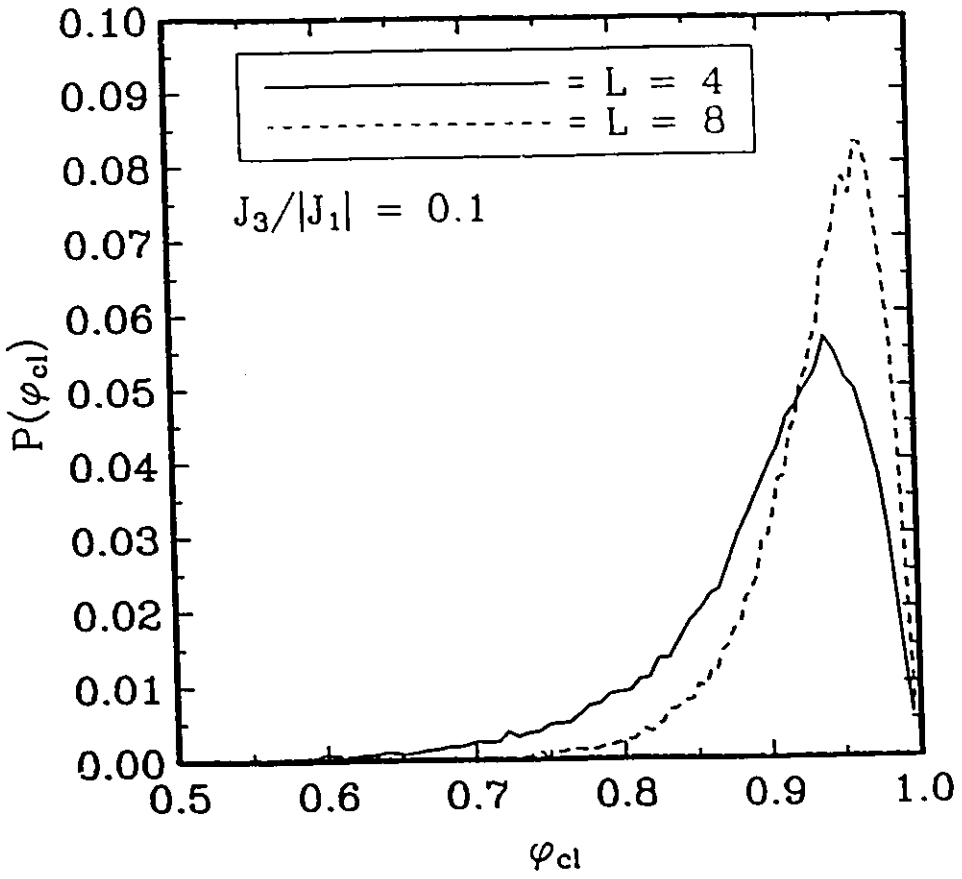

Fig. 5.16 Probability distribution for the collinearity function φ_{cl} (5.28).

One can see instantly that the system prefers on average to be collinear with significant fluctuations about the collinear state.

The ordered state of FeF_3 is certainly not collinear therefore there must be a uniaxial anisotropy strong enough to overcome the entropy forces that prefer the collinear state. This immediately raises the question as to whether or not the anisotropy in FeF_3 will affect the critical exponents. A simple answer would be yes! The anisotropy will lower the symmetry of the order parameter space and therefore change the critical exponents. A more sophisticated answer would be Yes and No! If the anisotropy is weak it will only be effective very close to T_c where $|T_c-T|$ is on the order of the anisotropy energy E_{aniso}. Thus when $|T_c-T| > E_{aniso}$ one will obtain

isotropic critical exponents since the system is fluctuating throughout the whole order parameter space. Crossover to anisotropic exponents will occur at $|T_c-T| \approx E_{aniso}$. A reasonable scenario for FeF_3 is that E_{aniso} is on the order .1K or less and thus beyond the temperature resolution of the experiment. In the presence of the anisotropy the ordered state is in fact two-fold degenerate corresponding to spin arrangements with all spins pointing inwards or outwards on a tetrahedron (Fig 5.15 right). Naively one might expect to see 3d Ising critical exponents for such a model although this is mere speculation.

Chapter 6

Conclusions and Suggestions For Further Work

It is of central importance for understanding this work to realize the the lattice of corner sharing tetrahedra (Fig 1.4) is very highly frustrated. Frustration means that all microscopic magnetic interactions cannot be simultaneously satisfied. This can be understood from inspection of Fig 1.1. In three instances we have seen clear evidence for long range antiferromagnetic order in pyrochlores. The first being $Nd_2Mo_2O_7$ which is most likely ferrimagnetic between 20 and 95K and antiferromagnetic below 20K. FeF_3 is seen to have an unusual non-coplanar type of long range order (Fig 2.6) below 16K. A complicated magnetic structure for $Mn_2Sb_2O_7$ is likely since the magnetic unit cell is large. The results for $Y_2Mn_2O_7$ are intriguing and deserve more careful consideration.

Except for $Nd_2Mo_7O_7$ and $Y_2Mo_2O_7$ all of the compounds showed diffuse magnetic scattering over a wide temperature range which indicates the presence of short range magnetic order. Three of the pyrochlores, $Y_2Mo_2O_7$, $Tb_2Mo_2O_7$ and $Y_2Mn_2O_7$ were very similar in behavior to spin glasses as evidenced by

1) Short range magnetic correlations over a wide temperature range
2) Cusps and irreversibilities in the magnetic susceptibility
3) Frequency dependence of $T(\chi_{max})$ ($Y_2Mn_2O_7$).
4) No anomalies in the heat capacity ($Y_2Mn_2O_7$)
5) Some degree of spin freezing below T_f ($Tb_2Mo_2O_7$)

As mentioned previously there seems to be no evidence for significant chemical disorder in these compounds. In fact the pyrochlore structure of $Y_2Mn_2O_7$ has been checked by single crystal X-ray diffraction[Su88]. These results are thus at odds with current ideas about spin glasses. It is generally believed that periodic (no disorder) frustrated systems are not candidates for spin glasses. There must be some degree of

randomness to get spin glass behavior. I can think of two possible explanations for the observed spin glass behavior in pyrochlores

1) The pyrochlore antiferromagnet is so frustrated that by some not yet understood mechanism, the spins freeze with random alignments below a certain temperature thus behaving like a spin glass in the absence of any disorder.

2) The pyrochlore antiferromagnet is so frustrated that the system will be sensitive to very small concentrations of defects (perhaps on the order of 1% or less) which generate spin glass behavior in a conventional manner.

Of the two explanations the first one is of course the most interesting and should not be ruled out at this point.

The mean field and monte carlo calculations show that the pyrochlore antiferromagnet with NN interactions and classical vector spins will not order at any temperature. The system is best described as a cooperative paramagnet[Vi79] which is not a spin glass. A theoretical model for a spin glass must exhibit spin freezing below a certain temperature. The MC results indicated that no spin freezing occurs with classical spins. If one can show that quantum spins will freeze in pyrochlore antiferromagnets then we would have strong support for explanation one above. This would indeed be an interesting result. Some work has already begun in this direction [Ha90] indicating that singlet pairs form in a random fashion with no long range order. Quantum Monte Carlo techniques may also be useful in augmenting these results and checking for spin freezing.

The Kagomé lattice[Li86] is in many respects a two dimensional analogue of the pyrochlore metal sublattice. Just like the pyrochlore lattice is a 3D network of

corner sharing tetrahedra the Kagomé lattice is a 2D network of corner sharing traingles. Mean field theory results for the Kagomé lattice antiferromagnet are almost identical to the results in chapter four for the pyrochlore problem. In particular there there is one $\vec{q}$-independant mode and no long range order is predicted. Recent experimental work (neutron scattering[Br90], magnetic susceptibility[Br90, Ra90] and heat capacity[Ra90a, Ra90b]) on the stacked Kagomé lattice system $SrCr_8Ga_4O_{19}$ show spin glass behaviour.

Weak further neighbor interactions, anisotropies and dipole forces will most likely force all pyrochlores to be long range ordered at low enough temperatures. The question is how low is low enough. Neutron diffraction experiments on compounds like $Tb_2Mo_2O_7$ at T = 1K, might be interesting. Particularly if some of the incommensurate phases predicted by the mean field calculations are observed. Of course there are many other compounds in the $RE_2Mo_2O_7$ and $RE_2Mn_2O_7$ series that are suitable for neutron scattering. $Ho_2Mo_2O_7$ and $Ho_2Mn_2O_7$ are good examples.

As mentioned in chapter one the free energy landscape in phase space develops a large number of degenerate local minima with essentially the same macroscopic properties. If one considers the flat dispersion curves for the NN pyrochlore antiferromagnet shown in Fig. 4.1 there are no local minima. However any small perturbation about this simple model will generate some local minima. It is possible that some combination of thermal and quantum fluctuations could generate a free energy landscape that is qualitatively similar to that of a spin glass. A major difference being that any local minima must necessarily be consistent with space group symmetry which is not the case in spin glasses.

As well as spin glass like behavior the critical properties in pyrochlore antiferromagnets that do order is also a very interesting topic of study. In particular the critical exponent $\beta = .18(2)$ in FeF_3 seems to be well confirmed by the Monte Carlo calculations. This is a record low value for β in three dimensional systems. As

well all of the other exponents except γ are unusual. $\alpha = .6(1)$ is a record high for any system. $\nu = .39(2)$ is a record low, in fact this is the only known instance where $\nu < \frac{1}{2}$!. Another exponent that has not been mentioned so far is η which describes the decay of the correlation function. At $T = T_c$ we have

$$C(R) = \langle S(0) \cdot S(R) \rangle = \frac{1}{R^{d-2+\eta}} \tag{6.1}$$

By integrating C(R) over all space one obtains the susceptibility and one can relate η to γ and ν

$$\eta = 2 - \frac{\gamma}{\nu}. \tag{6.2}$$

Using the the exponents from chapter 5 one obtains $\eta = -.8$. Usually η is very close to zero and positive, thus for the model simulated in chapter 5 we have yet another unusual result. As stated previously the MC technique will give one an approximate answer without telling us why. A renormalization group calculation will most likely give very interesting results and furnish some answers as to why the exponents are so unusual.

The large value of α should definitely be checked by heat capacity measurements. Other exponents like χ, ν and η can all be measured with neutron diffraction if large single crystals are available. The expected anisotropy and possible crossover effect will of course complicate the interpretation of any data from FeF3. The pyrochlore form of FeF_3 is meta-stable and transforms the a different isomorph above about 300C [Fe86] making crystal growth from the melt impossible. I believe in the old maxim "Where there is a will there is a way" and I think that the results obtained so far are interesting enough to provide the will. Since FeF_3 is stabilized by

the presence of ammonia in the lattice cavities it might be worthwhile attempting to grow a single crystal of $ND_3Fe_2F_6$.

Further study of pyrochlore compounds will perhaps answer some questions about spin glasses and critical phenomena at a general level.

Appendix A:

In order to prove that the simultaneous absence of the (111), (200) and (220) magnetic reflections in $Y_2Mo_2O_7$ is inconsistent with any non-zero ordered moment, we first write down the Mo^{4+} contribution to the magnetic structure factor a pyrochlore (2.20)

$$\vec{F}_{hkl} \propto \vec{S}_1^{\perp} + \vec{S}_2^{\perp} e^{i\pi(k+l)/2} + \vec{S}_3^{\perp} e^{i\pi(h+l)/2} + \vec{S}_4^{\perp} e^{i\pi(h+k)/2} \quad \text{(A1)}$$

where

$$S_x^{\perp} = S_x - h\frac{hS_x+kS_y+lS_z}{h^2+k^2+l^2} \quad \text{(A2)}$$

and similarly for y and z. In order for the (111) powder reflection to be absent we must have $\vec{F}(111) = 0$, $\vec{F}(1\bar{1}\bar{1}) = 0$, $\vec{F}(\bar{1}1\bar{1}) = 0$, and $\vec{F}(\bar{1}\bar{1}1) = 0$. Solving these four equations gives the following set of conditions on the spin vectors

$$S_{1x} = -S_{2y} = -S_{3z} \quad \text{(A3a)}$$

$$S_{2x} = -S_{1y} = -S_{4z} \quad \text{(A3b)}$$

$$S_{3x} = -S_{4y} = -S_{1z} \quad \text{(A3c)}$$

$$S_{4x} = -S_{3y} = -S_{2z}\,. \quad \text{(A3d)}$$

Similarly the absence of the (200) and (220) reflections gives

$$S_{1x} = S_{4x} \text{ and } S_{2x} = S_{3x} \tag{A4a}$$

$$S_{1y} = S_{3y} \text{ and } S_{2y} = S_{4y} \tag{A4b}$$

$$S_{1z} = S_{2z} \text{ and } S_{3z} = S_{4z} \tag{A4c}$$

and

$$\vec{S}_1 = \vec{S}_2 = \vec{S}_3 = \vec{S}_4 \tag{A5}$$

respectively. Conditions A3, A4 and A5 can only be simultaneously satisfied if all $\vec{S}_i = 0$ which implies no long range ordered moment. As well conditions (A3) and (A4) can only be simultaneously satisfied by Ferey's 109° spin arrangment Fig. 2.6 and eqn. (4.45).

Appendix B:

Here we write out the matrix elements of the $J_{\vec{q}}^{ab}$ matrix, including the first four coordination shells of neighbors. Since the lattice is centro-symmetric $J_{\vec{q}}^{ab}$ is real and symmetric.

$$J_{\vec{q}}^{11} = J_{\vec{q}}^{22} = J_{\vec{q}}^{33} = J_{\vec{q}}^{44} = 4J_3Q\,,$$

where Q is defined in Eq. (4.25).

$$J_{\vec{q}}^{12} = J_{\vec{q}}^{21} = 2J_1\cos(q_x) + 2J_2\left[\cos(2q_y-q_x)+\cos(2q_z-q_x)\right] + 4J_4\cos(2q_y-2q_z)\cos(q_x)\,,$$

$$J_{\vec{q}}^{13} = J_{\vec{q}}^{31} = 2J_1\cos(q_y) + 2J_2\Big(\cos(2q_z-q_y)+\cos(2q_x-q_y)\Big) + 4J_4\cos(2q_z-2q_x)\cos(q_y)\,,$$

$$J_{\vec{q}}^{14} = J_{\vec{q}}^{41} = 2J_1\cos(q_z) + 2J_2\Big(\cos(2q_x-q_z)+\cos(2q_y-q_z)\Big) + 4J_4\cos(2q_x-2q_y)\cos(q_z)\,,$$

$$J_{\vec{q}}^{23} = J_{\vec{q}}^{32} = 2J_1\cos(q_x-q_y) + 2J_2\Big(\cos(q_x+q_y)+\cos(2q_z-q_x-q_y)\Big) + 4J_4\cos(q_x-q_y)\cos(2q_z)\,,$$

$$J_{\vec{q}}^{24} = J_{\vec{q}}^{42} = 2J_1\cos(q_z-q_x) + 2J_2\Big(\cos(q_z+q_x)+\cos(2q_y-q_z-q_x)\Big) + 4J_4\cos(q_z-q_x)\cos(2q_y)\,,$$

$$J_{\vec{q}}^{34} = J_{\vec{q}}^{43} = 2J_1\cos(q_y-q_z) + 2J_2\Big(\cos(q_y+q_z)+\cos(2q_x-q_y-q_z)\Big) + 4J_4\cos(q_y-q_z)\cos(2q_x)\,.$$

Appendix C:

In order to prove that (4.39) is exact to all orders in $(m^2+\phi_4^2)$ note that at $\vec{q} = 0$ we need only consider the free energy in one unit cell. From the eigenvectors in Table 5, (4.18), and conditions (4.34) one can show that

$$(B^a)^2 = \frac{1}{4}\sum_i \phi_i^2 = \frac{1}{4}(m^2+\phi_4^2),\ a = 1..4\,. \qquad \text{(C1)}$$

From (4.8) we can write down the free energy of one unit cell

$$f(T,\vec{H}) = -\frac{1}{2}\sum_{ab} J_0^{ab}\,\vec{B}^a\cdot\vec{B}^b + \vec{H}\cdot\sum_a \vec{B}^a - T\sum_a S(B^a) \qquad \text{(C2)}$$

$$= -2H\Phi_4 - \frac{n}{2}T_c m^2 + \frac{1}{2}(3nT_c - 48j_3)\Phi_4^2 - 4T\,S\left(\frac{1}{4}\sqrt{m^2+\Phi_4^2}\right), \qquad \text{(C3)}$$

with equilibrium conditions

$$\left(-nT_c - \frac{T}{\sqrt{m^2+\Phi_4^2}}\,S'\right) m = 0, \qquad \text{(C4)}$$

$$\left(3nT_c - 48j_3 - \frac{T}{\sqrt{m^2+\Phi_4^2}}\,S'\right)\Phi_4 = 2H, \qquad \text{(C5)}$$

where

$$S' = \frac{\partial\ S}{\partial\sqrt{m^2+\Phi_4^2}} \qquad \text{(C6)}$$

Finally when $m \neq 0$, conditions (C4) and (C5) give

$$\Phi_4 = \frac{H}{2(nT_c - 12j_3)}. \qquad \text{(C7)}$$

References:

Ak 77 J. Akimitzu, K. Siratori, G Shirane, M. Iizumi and T. Watanabe, J. Phys. Soc. Jap. 44, 172 (1977)

Al 82 A. Albinati and B. T. M. Willis, J. Appl. Cryst. 15, 361 (1982).

Al 89 N. Ali, P. Hill, S. Labroo and J. E. Greedan, J. Solid State Chem. 83, 178 (1989).

Am 88 D. J. Amit, "Field Theory, The Renormalization Group, and Critical Phenomena", World Scientific (1984).

An 56 P. W. Anderson, Phys. Rev. 102, 1008 (1956).

An 83 P. W. Anderson, Proc. Natl. Acad. Sci. 80, 3386 (1983).

Ba 75 G. E. Bacon, "*Neutron Diffraction*", Oxford University Press (1975).

Ba 87 R. Ballou, J. Deportes, R. Lemaire, Y. Nakamura and B. Ouladdiaf, J. Mag. Mag. Mat. 70, 129 (1987)

Ba 88 R. Ballou, J. Deportes, R. Lemaire and B. Ouladdiaf, J. Appl. Phys. 63, 3487 (1988),

Ba 89 $Nd_2Mo_2O_7$ SANS data was collect by F. Barakat and J. Avelar, 1989.

Be 61 E. F. Bertaut, J. Phys. Chem. Solids 21, 256 (1961).

Be 67 E. F. Bertaut and P. Burlet, Sol. State Comm. 5, 279 (1967).

Bi 79 K. Binder, "Monte Carlo Methods in Statistical Physics", Springer (1979).

Bi 81 K. Binder, Z. Phys. B43, 119 (1981).

Bi 83 K. Binder, "Applications of the Monte Carlo Method", Springer (1983).

Bi 86 K. Binder and A. P. Young, Rev. Mod. Phys. 58, 801 (1986).

Bl 68 H. W. J. Blote, R. F. Wielinga and W. J. Huiskamp, Physica 43, 549 (1968).

Br 90 C. Broholm, G. Aeppli, G. P. Espinosa and A. S. Cooper. J. Appl. Phys. 67, 5799 (A) (1990).

Ch 87 D. Chandler, "Introduction to Modern Statistical Mechanics", Oxford University Press (1987).

Co 89 M. F. Collins, "*Magnetic Critical Scattering*", Oxford University Press (1989).

Da 64 A. Danielian, Phys. Rev. 133, A1344 (1964).

De 86 R. DePape and G. Ferey, Mat. Res. Bull. 21, 971 (1986).

El 89 V. Elser, Phys. Rev. Lett. 62, 2405 (1989).

Fe 86 G. Ferey, R. De Pape, M. Leblanc and J. Pannetier, Revue de Chemie Minerale 23, 474 (1986).

Fi 71 M. E. Fisher: In "*Critical Phenomena*", ed. by M. S. Green, Academic Press, New York (1971)

Fi 72 M. E. Fisher and M. N. Barber, Phys. Rev. Lett. 28, 1516 (1972).

Fi 74 M. E. Fisher, Rev. Mod. Phys. 46, 597 (1974).

Fe 88 A. M. Ferrenberg and R. H. Swendsen, Phys Rev. Lett. 61, 2635 (1988).

Fe 89a A. M. Ferrenberg and R. H. Swendsen, Phys Rev. Lett. 63, 1195 (1988).

Fe 89b A. M. Ferrenberg and R. H. Swendsen, Computers in Physics Sep/Oct, 101 (1989).

Ga 88 B. D. Gaulin, M. Hagen and H. R. Child, J. Phys. (Paris) 49, C8-327 (1988).

Ga 90 Triple axis measurements for $Tb_2Mo_2O_7$ were carried out by B. D. Gaulin and Z. Tun, on the N5 spectrometer of the NRU reactor at the Chalk River Nuclear Laboratories (1990).

Gr 86 J. E. Greedan, M. Sato, X. Yan and F. S. Razavi, Solid State Comm. 540/541, 117 (1986).

Gr 88 J. E. Greedan and J. N. Reimers, unpublished work. Weak reflections in time flight neutron diffraction data obtained from the GPPD at Argonne National Labs, were only consistent with a large (roughly orthorhombic) unit cell with dimensions a=7.2, b=12.47, c=17.42 Å in the space group P2. This is a super cell with double the volume of the one reported by Scott in the space group $P3_121$.

Gr 89 D. S. Greywall and P. A. Busch, Phys. Rev. Lett. 62, 1868 (1989).

Gr 90 J. E. Greedan, "*Magnetic Pyrochlore Oxides*" in Landolt-Bornstein New Series, Vol. III/27 "*Magnetic Properties of Non-Metals*".

Ha 56 J. M. Hastings and L. M. Corliss, Phys. Rev. 102, 1460 (1956)

Ha 84 A. B. Harris, O. G. Mouritson and A. J. Berlinsky, Can. J. Phys. 62, 915 (1984).

Ha 90 A. B. Harris, A. J. Berlinsky and C. Bruder, unpublished.

He 87 C. L. Henley, J. Appl. Phys. 61, 3962 (1987).

Ho 82 J. J. Hopfield, Proc. Natl. Acad. Sci. 79, 2554 (1982).

Ka 66 L. P. Kadanoff, Physics 2, 263 (1966).

Ka 67 L. P. Kadanoff, W. Gotze, D. Hamblen, R. Hecht, E. A. Lewis, V. V. Palciauskas, M. Rayl and J. Swift., Rev. Mod. Phys. 39, 395 (1967).

Ka 87 H. Kadowaki, K. Ubukoski, K. Hirakawa, J. L. Martinez and G. Shirane, J. Phys. Soc. Jpn. 56, 1294 (1987).

Ka 88 H. Kawamura, J. Appl. Phys. 63, 3086 (1988) and references therein.

Ka 89 H. Kawamura, J. Phys. Soc. Jap. 58, 584 (1989).

Ki 83 S. Kirkpatrick, C. D. Gelatt, Jr., and M. P. Vacchi, Science 220, 671 (1983).

Kr 34 H. A. Kramers, Physica 1, 182 (1934).

Kr 89 All susceptibility and heat capacity data for $Y_2Mn_2O_7$ were measured by R. K. Kremer and E. Gmelin at the Max Plank Institute fur Festkorperforshung in Germany, 1989.

La 76a D. P. Landau, Phys. Rev. B14, 255 (1976).

La 76b D. P. Landau, Phys. Rev. B13, 2997 (1976).

La 87 P. Lacorre, J. Phys. C20, L775 (1987).

La 90 B. E. Larson and C. L. Henely, to appear Phys. Rev. B (1990).

Le 84 T. D. Lee, R. G. Caflisch, J. D. Joannopoulos and F. Y. Wu, Phys. Rev. B29, 2680 (1984).

Li 74 W. A. Little Math Biosc. 19, 101 (1974).

Li 86 R. Liebmann, "*Statistical Mechanics of Periodic Frustrated Ising Systems*", Springer (1986), A discussion of antiferromagnetic ordering of Ising spins on the 3-D pyrochlore lattice can be found on pg. 117. For a picture of the Kagomé lattice see pg. 27 fig. c.

Lo 71 F. K. Lotgering, J. Phys (Paris) Colloq. 32, C1-34 (1971)

Lo 84 S. W. Lovesey, "*Theory of Neutron Scattering From Condensed Matter*", Oxford University Press (1984).

Ma 89 T. E. Mason, M. F. Collins and B. D. Gaulin, Phys. Rev. B39, 586 (1989).

Me 53 N. Metropolis, A. Rosenbluth, M. Rosenbluth, A. Teller and E. Teller, J. Chem. Phys. 21, 1087 (1953).

Mo 84 O. G. Mouritson, "Computer Studies of Phase Transitions and Critical Phenomena".

Pa 86 J. Pannetier, Data collected on the D1B powder instrument at the ILL in Grenoble France, unpublished work

Pe 89a Wide angle neutron scattering data were measured by S. L. Penny and J. E. Greedan, 1989.

Pe 90b Susceptibility data for $Tb_2Mo_2O_7$ were measured by S. L. Penny and G. Hewitson (1989).

Pl 75 R. Plumier, M. Leconte, A. Miedan-gros and M. Sougi, Phys. Lett. 55A, 239 (1975)

Po 82 C. Poole, H. A. Farach, Z. Phys. B47, 55 (1982)

Ra 88 E. Rastelli and A. Tassi, J. Phys. C19, L423 (1986) and J. Phys. C21, L35 (1988).

Ra 90 A. P. Ramirez, G. P. Espinosa and A. S. Cooper, Phys. Rev. Lett. 64, 2070 (1990).

Ra 90 A. P. Ramirez, G. P. Espinosa and A. S. Cooper, in press.

Re 88 J. N. Reimers, J. E. Greedan and M. Sato, J. Solid State Chem. 72, 390 (1988).

Ri 67 H. M. Rietveld, Acta Cryst. 22, 151 (1967).

Ri 69 H. M. Reitveld, J. Appl. Cryst. 2, 65 (1969).

Ru 63 G. S. Rushbrooke, J. Chem. Phys. 39, 842 (1963)

Sa 86 M. Sato, X. Yan and J. E. Greedan, Z. Anorg. Allg. Chem. 540/541, 177 (1986).

Sc 87 H. G. Scott, J. Solid State Chem. 66, 171 (1987).

Sq 78 G. L. Squires, "*Introduction to the Theory of Neutron Scattering*", Cambridge University Press (1978).

St 77 C. Stassis, H. E. Deckman, B. N. Harmon, J. P. Desclaux and A. J. Freeman, Phys. Rev. B15, 369 (1977).

Su 83 M. A. Subramanian, G. Aravamudan and G. V. Subba Rao, Prog. Solid State Chem. 15, 55 (1983).

Su 84 M. A. Subramanian, A. Clearfield, A. M. Umarji, G. K. Shenoy and G. V. Subra Rao, J. Solid State Chem. 52, 124 (1984).

Su 88 M. A. Subramanian, C. C. Torardi, D. C. Johnson. J. Pannetier and A. W. Sleight, J. Solid State Chem. 72, 24 (1988).

Vi 78 J. Villain, Z. Physik B33, 31 (1978).

Vo 87 V. G. Vologin, Sov. Phys. Solid State 29, 1339 (1987).

Wi 61 M. Wilkinson, E. Wollan, H. Child and J. Cable, Sol. State Comm. 5, 279 (1967).

Wi 65 B. Widdom, J. Chem. Phys. 43, 3892; J. Chem. Phys. 43, 3898 (1965).

Ya 52 C. N. Yang, Phys. Rev. 85, 808 (1952).

Zi 88 G. O. Zimmerman, A. K. Ibrahim and F. Y. Wu, Phys. Rev. B37, 2059 (1988).

$O = \phi(w+\ell)$